NOISE PROPERTIES OF InGaAs/InAlAs MULTIQUANTUM-WELL HETEROSTRUCTURE P-I-N PHOTODIODES

By

YOUNG-JUNE YU

A DISSERTATION PRESENTED TO THE GRADUATE SCHOOL
OF THE UNIVERSITY OF FLORIDA IN
PARTIAL FULFILLMENT OF THE REQUIREMENTS FOR THE
DEGREE OF DOCTOR OF PHILOSOPHY

UNIVERSITY OF FLORIDA

1989

ACKNOWLEDGEMENTS

The author wishes to express his sincere gratitude to Dr. Gijs Bosman for his most valuable guidance and many helpful discussions and also to Professor A. van der Ziel, Professor C.M. Van Vliet and Professor Peter Landsberg for their support and helpful suggestions.

The author wishes to thank the other committee members, Dr. Ramaswamy, Dr. Li and Dr. Tim Anderson, and Dr. Bhattacharya from the University of Michigan, Ann Arbor, for supplying the MQW-APD devices. The author also wishes to thank his fellow students in the Noise Research Laboratory, Chris Whiteside, Arthur van Rheenen, Mike Trippe, Min-Yih Luo, Sheng-Lyang Jang, Horng-Jye Luo, and his fellow Korean students, Hanggeun Jeong, Myung Seok Jo, Jean Young Choi, Young Seok Kim, Sang Sun Lee, Ju Sung Park, Duk Soo Jun, Sung Jae Lee, Young Soon Kim and Gap Kyu Lim for their help and many interesting discussions.

Special thanks go to his mother Kim Bok-Joo and his brothers and sisters, who have supported and encouraged him over the years.

TABLE OF CONTENTS

Page

ACKNOWLEDGEMENTS ii

ABSTRACT vi

CHAPTER

I INTRODUCTION 1

II REVIEW OF CONVENTIONAL AVALANCHE PHOTODIODE OPERATION 6

- 2.1.. Impact Ionization 6
  - 2.1.1. Definition of the Impact Ionization Coefficient 6
  - 2.1.2. Impact Ionization Mechanism 8
  - 2.1.3. Impact Ionization Threshold Energy....... 13
    - 2.1.3.1. Conditions for Threshold 14
    - 2.1.3.2. Calculation of Ionization Threshold Energy............................ 16
- 2.2. Noise Theory 28
  - 2.2.1. Binomial Process 28
  - 2.2.2. Poisson Process 28
  - 2.2.3. Variance Theorem 29
  - 2.2.4. Excess Noise Factor 31
  - 2.2.5. Generating Functions and Compounding Theorem 34
  - 2.2.6. General Theory of Avalanche Noise by Van Vliet and Rucker 36
  - 2.2.7. Discrete Noise Characteristics of the Avalanche Photodiode 46
  - 2.2.8. Excess Noise Factors for the Staircase Avalanche Photodiode 49

- 2.3. Device Operation 58
  - 2.3.1. Design Considerations 58
    - 2.3.1.1. Gain (Multiplication) 58
    - 2.3.1.2. Noise Equivalent Power and Detectivity 60
    - 2.3.1.3. Bandwidth 61
    - 2.3.1.4. Quantum Efficiency 64
    - 2.3.1.5. Dark Current 68
    - 2.3.1.6. Avalanche Photodiode Structure..... 72

2.3.2. Parameter Measurements 75

III TWO SIMPLE PROOFS OF CAPASSO'S EXCESS NOISE FACTOR F_N OF AN IDEAL N-STAGE STAIRCASE MULTIPLIER 84

IV NONPARABOLICITY AS A TOOL IN BANDGAP ENGINEERING .. 88

4.1. Introduction 88
4.2. Derivation of a Formula for the Impact-ionization Threshold Energy with Nonparabolic Conduction Band and One or Two Parabolic Valence Band 89
4.3. Further Discussions Concerning the Nonparabolicity 93

V THE THEORY OF TRAPPING AND DETRAPPING OF ELECTRONS IN MULTIQUANTUM-WELL (MQW) HETEROSTRUCTURES 98

5.1. Introduction 98
5.2. Trapping and Detrapping in Multiquantum-wells 101
5.3. Trapping in Heterojunction Interface States... 120

5.4. Computer Calculations of the Trapping Noise... 125

VI EXPERIMENTS ON MULTIQUANTUM-WELL (MQW) HETEROSTRUCTURE P-I-N PHOTODIODES 133

6.1. Introduction 133
6.2. Device Description 134
6.3. D.C. Measurements and Results................ 137
6.4. Noise Measurement Set-up 147
6.4.1. High-Frequency (150 MHz - 1 GHz) Noise Measurement Set-up 152
6.4.2. Medium-High-Frequency (10 MHz - 300 MHz) Noise Measurement Set-up 159
6.4.3. High-Frequency Noise Measurement Procedure 162
6.4.4. Low-Frequency Noise Measurement Set-up and Procedure 164
6.5. Results and Discussion of the Noise Measurements 169

VII SUMMARY, CONCLUSIONS AND RECOMMENDATIONS FOR FUTURE RESEARCH 184

7.1. Summary and Conclusions 184
7.2. Recommendations for Future Research 187

APPENDICES

A APPLICATION OF THE COMPOUNDING THEOREM TO A BERNOUILLI TRIAL.................................. 190

B EVALUATION OF SUB-INTEGRALS 192

C EVALUATION OF DOUBLE INTEGRALS.................... 196

REFERENCES 198

BIOGRAPHICAL SKETCH 203

Abstract of Dissertation Presented to the Graduate School
of the University of Florida in Partial Fulfillment of the
Requirements for the Degree of Doctor of Philosophy

NOISE PROPERTIES OF InGaAs/InAlAs MULTIQUANTUM-WELL HETEROSTRUCTURE P-I-N PHOTODIODES

By

Young-June Yu

May 1989

Chairperson: G. Bosman
Major Department: Electrical Engineering

The charge transport process in InGaAs/InAlAs multiquantum-well (MQW) heterostructure p-i-n photodiodes is studied experimentally and theoretically. Current-voltage (I-V), capacitance-voltage (C-V), S-parameter, and noise measurements are performed at room temperature over a wide range of reverse bias. The devices under study consist of alternating, undoped, lattice matched InGaAs and InAlAs layers sandwiched between a heavily doped n and p layer of InGaAs. To determine the dependence of charge transport phenomena on quantum-well width, a set of three different quantum-well layers of, respectively, 30, 90, and 500 Angstrom wide were used.

Upon illumination by a light-emitting-diode (1350 nm), measurements of the noise spectra were performed at frequencies ranging from 100 Hz to 1 GHz. In the frequency range of 200 MHz and 1 GHz, the 90-90 and 500-500 Angstrom

devices which have nontransparent barriers between neighboring quantum-wells, show distinctive sub-shot noise level at low bias. This sub-shot noise phenomenon is interpreted in terms of the trapping and detrapping of electrons in undepleted quantum-wells. The magnitude of the noise is proportional to 1/N, where N is the number of undepleted quantum-wells. The dependence of noise levels on bias indicates that quantum-wells located in the i-region are successively and gradually depleted with increasing reverse bias. C-V measurements support this finding.

To explain the sub-shot noise levels, a MQW trapping noise model was developed employing the Transfer Impedance method.

The excess noise observed at frequencies below 200 MHz is caused by the trapping and detrapping of electrons in heterojunction interface states.

Current-voltage measurements performed under illumination indicated that the quantum efficiency of the photodiode is bias dependent. We established that the photocurrent is controlled by field assisted injection of optically generated electrons from the low bandgap absorption region into the intrinsic region.

Finally, nonparabolicity of the conduction band was studied and a new formula for the ionization threshold energy was derived and compared with experimental values.

CHAPTER I
INTRODUCTION

In recent years there have been a number of remarkable advances in the fabrication of crystalline semiconductor heterostructures made possible by molecular beam epitaxy (MBE) and metal-organic chemical deposition (MOCVD). These epitaxial growth techniques allow for the precise control of both the thickness of heterostructure layers and the composition of compound materials and make bandgap engineering possible. A new generation of devices with artificial band profiles and structures is emerging from this approach.

Among novel structures, multiquantum-well (MQW) heterojunctions and superlattices are of great interest because they are the simplest examples of man-made structures which allow for the modification of electronic and optical properties. Applications as well as fundamental studies on these structures are being worked on by researchers in many different areas.

In the area of fiber-optic communications, considerable efforts have been devoted to the development of low-noise, high-gain avalanche photodiodes (APDs). As suggested by McIntyre, excess noise in APDs is small when the electron-to-hole impact ionization coefficient ratio,

α/β, is very large or very small. However, most III-V semiconductors of interest have nearly equal electron and hole ionization coefficients. Therefore, there is a strong desire to artificially enhance this ratio.

Chin et al. [1] first proposed a method for artificially enhancing the impact ionization coefficient ratio by employing a multilayered GaAs/AlGaAs structure. Capasso et al. [2] and Juang et al. [3] reported the experimental results of an enhanced α/β ratio in GaAs/AlGaAs multiquantum-well structures.

For fiber-optic communications, wavelengths of 1.3 μm or 1.55 μm should be used to minimize the attenuation of light transmission and dispersion in optical-fibers. Among the materials sensitive to these wavelength, the $In_{0.53}Ga_{0.47}As$ ternary compound in conjunction with $In_{0.52}Al_{0.48}As$ is most widely used to make heterojunctions. Capasso et al. [4] experimentally investigated $In_{0.53}Ga_{0.47}As/In_{0.52}Al_{0.48}As$ multiquantum-well structures and reported the enhanced α/β ratio at low temperature.

One of our initial research objectives was to measure the α/β ratios from noise measurements in several MQW structures with different dimensions. However, it turns out that in this material and in MQW structures, Zener tunneling current easily dominates with the result that we could never obtain a high enough field to have band-to-band impact ionization. Allam et al. [5] also reported that strong resonant Zener tunnelling occurs in these structures at room temperature. Without finding a new way to reduce the Zener tunnelling current an InGaAs/InAlAs MQW structure is not suited for APD applications. This disappointing situation was not recognized until the experiments were actually performed. Therefore, a more general treatment in terms of charge transport is needed to investigate this novel MQW structure before considering its applications.

The charge transport in our structures takes place in the direction perpendicular to the heterojunction interfaces. In semiconductor transport problems the following four situations may arise. Note that a combination of more than one situation may exist.

1) The carrier density increases due to multiplication.
2) The carrier density decreases due to recombination.
3) The carrier flow is slowed down due to trapping or scattering.
4) The carrier flow speeds up due to higher mobility and less scattering.

In our structure the first situation is excluded as explained above. The second case does not apply to the depleted section of quantum-well layers. The third case is most probable to occur in the MQW structures we investigated. Finally, the fourth situation usually applies to the situation where carrier transport is in a direction parallel to the heterostructure interfaces, as it occurs for example in modulation doped FETs.

The main objective of this dissertation is to study the charge transport noise in MQW heterostructure p-i-n diodes. The noise measurement tool was extensively employed to investigate the microscopic charge transport mechanisms of the p-i-n photodiodes. To measure the high frequency noise, a new measuring set-up was built. The noise spectrum was measured over a wide frequency range from 100 Hz to 1 GHz. In addition to noise measurements, conventional, basic measurements such as current-voltage (I-V), capacitance-voltage (C-V) measurements and impedance (S-parameter) measurements were performed to characterize the devices under study. As an unexpected finding, we observed distinctive sub-shot noise levels at low bias which to the author's knowledge have never been observed before. In Chapter VI, this sub-shot noise phenomenon is identified and interpreted in terms of trapping and detrapping in the quantum-wells. To explain the results of our noise measurements we developed a simplified trapping and detrapping model and a qualitative theory.

The organization of this thesis is as follows. Chapter II presents a review of conventional avalanche photodiodes. The details of the impact-ionization mechanism and device noise are presented. In addition, various design considerations of an APD are discussed as they relate to low-noise performance.

In Chapter III, the expression for the excess noise factor of an ideal n-stage staircase multiplier is presented with some proofs.

Chapter IV discusses nonparabolicity as a tool in band-gap engineering. A new formula for the threshold energy of electron-electron-hole impact ionization for the case of a parabolic valence band and a simple Kane type, nonparabolic conduction band is presented.

In Chapter V, the theory for carrier trapping and detrapping in multiquantum-wells and at heterojunction interfaces is developed. As a result, an expression for the sub-shot noise factor is found.

Chapter VI, the highlight of this dissertation, describes the multiquantum-well device structures and various measurement schemes used in this study. Particularly, the noise measurements are discussed in detail. Experimental results are presented with qualitative discussions.

Finally, conclusions are presented, followed by a summary of this work and some recommendations for future research.

CHAPTER II
REVIEW OF CONVENTIONAL AVALANCHE PHOTODIODE OPERATION

2.1. Impact Ionization

2.1.1. Definition of the Impact Ionization Coefficient

When the electric field is constant in the avalanche region and a spatial steady state is achieved, the impact ionization coefficient is defined as the probability per unit length along the direction of the field that a carrier impact ionizes. Equivalently, this definition reduces to the reciprocal of the average distance <x> along the direction of the field between two consecutive ionizing collisions.

The ionization coefficients are calculated as follows [6]

$$\alpha = \frac{1}{|v_n|\tau_n}, \qquad \beta = \frac{1}{|v_p|\tau_p} \qquad (2.1)$$

where v_n and v_p are the electron and hole drift velocities, respectively, and τ_n and τ_p are the times for an electron and hole to create a pair. Hence, the ionization rates are identified with the mean free paths between ionizing collisions. The above definition is not valid for situations of non-constant electric field or for an ionization coefficient which depends on position. Thornber [7] has introduced the following more general definition in terms of the number of electron-hole pairs created per unit time per unit volume normalized to the incident carrier density;

$$\alpha = \frac{e\mathcal{E}}{E_{th}} P(E_{th}) \tag{2.2}$$

where $\mathcal{E}$ denotes the electric field, E_{th} denotes the threshold energy, and $P(E_{th})$ represents a probability function which depends on threshold energy and electric field. Since P is a strongly increasing function of the electric field, as we will show in Eq. (2.9), P approaches unity at high fields. Then the average distance between consecutive ionizing collisions becomes

$$\alpha^{-1} \sim \langle x \rangle = \frac{E_{th}}{e\mathcal{E}} \quad \text{(high field)} \tag{2.3}$$

This distance is the minimum distance required for a carrier to create an electron-hole pair.

At low electric fields, where $P(E_{th})$ is less than unity, this distance must be much larger than the minimum distance and is expressed as

$$\langle x \rangle \gg \frac{E_{th}}{e\mathcal{E}} \quad \text{(low field)} \tag{2.4}$$

2.1.2. Impact Ionization Mechanism

Impact ionization is an essential mechanism in the operation of avalanche photodiodes (APD) and impact-avalanche transit time (IMPATT) diodes. At present this mechanism is not completely understood and several competing theories are available [8,9,10].

Wolff was the first to calculate the ionization rate in semiconductors. He applied a method borrowed from the gas discharge theory to solve the Boltzmann transport equation. He assumed that electrons experience only two types of collisions: collisions with optical phonons and collisions with valence electrons; the latter is producing impact ionization.

At high electric fields, he assumed that the energy gained between impact ionizations is much larger than the energy lost per phonon collision, i.e.,

$$e\mathbf{E}\lambda \gg E_p \tag{2.5}$$

where E_p is the energy lost per phonon collision and λ is the mean free path between impact ionizations. In this situation an electron can undergo many phonon collisions while gaining energy from the electric field. Since the electron changes its direction at each collision, many phonon collisions serve to keep the velocity distribution nearly isotropic. Hence, using only the first two terms of a Legendre polynomial expansion, Wolff approximated the velocity distribution function by [8]

$$F(v,\theta) = f_o(v) + f_1(v)\cos\theta \qquad (2.6)$$

where $f_o(v)$ represents the spherically symmetric part of the distribution and $f_1(v)$ is the asymmetric part arising from the perturbations caused by the applied electric field. Since θ is the angle between the velocity of the carrier and the electric field, the $\cos\theta$ term represents the net contribution to the distribution function in the direction parallel to the electric field.

Using this approximate distribution function and a Maxwellian approximation, Wolff solved the Boltzmann transport equation to calculate the ionization rate with the result

$$\alpha(\mathcal{E}) \sim \exp\left(-\frac{A}{\mathcal{E}^2}\right) \qquad (2.7)$$

where A is a constant.

On the other hand we may look at the situation

$$e\mathcal{E}\lambda \leq E_p \qquad (2.8)$$

i.e., the energy gained between impact ionization is less than the energy lost per phonon collision. In this situation carriers will not be able to gain the high energies required for impact ionization unless they escape phonon collisions. These carriers are the "lucky" or ballistic carriers first considered by Shockley [9]. The probability that a lucky electron, starting at zero energy, ballistically gains the threshold energy for ionization is equal to the probability that it travels for the ionization distance, $E_{th}/e\mathcal{E}$, without undergoing a phonon collision; i.e.,

$$P(E_{th}) = \exp(-\frac{E_{th}}{e\mathcal{E}\lambda}), \tag{2.9}$$

from which Shockley derived

$$\alpha = \frac{e\mathcal{E}}{E_{th}} \exp(-\frac{E_{th}}{e\mathcal{E}\lambda}) \tag{2.10}$$

Next, Baraff [10] argued that the distribution function of the electron energy was neither a spike in the direction of the field (Shockley's ballistic theory) nor nearly isotropic (Wolff). He said that these two aspects were complementary and assumed a velocity distribution of the form

$$f(v,\cos\theta) = A(v) + B(v)\delta(1 - \cos\theta) \tag{2.11}$$

which is a mixture of a spherical part and a "spike" in the direction of the electric field.

By using this distribution function, Baraff solved the Boltzmann equation and showed that his result contained Shockley's result as a low-field limit and Wolff's result as a high-field limit.

His theory is fairly successful in describing the ionization rates in Si and Ge, but does not explain very well the ionization rates in materials where strong band structure effects exists, as in III-V compounds. Also, his theory somewhat obscures the detailed physical mechanism by which carriers reach the ionization energy.

Shichijo and Hess [11] performed a Monte Carlo simulation of the impact ionization phenomenon in GaAs and provided a very clear physical picture of the impact ionization process. They explained it as follows.

Most of the time, an electron stays around the average energy of 0.7 ~ 1.2 eV under the heating influence of an electric field of the order of 5×10^5 V/cm and the cooling influence of phonon collisions. Occasionally, however, one of these electrons will escape phonon collisions and move up to higher energies. When an electron reaches 2.0 eV, as in the case of GaAs, it causes an impact ionization. We can think of this electron as one of the lucky electrons in Shockley's theory [9], and of the electrons around the average energy as the diffusing electrons in Wolff's theory [8].

It is also important to note the difference between this theory and Shockley's theory. Shockley's "lucky" electrons start from zero energy, escape the phonon scattering completely, and impact ionize. The ionizing electrons in the Hess theory start at an average energy and reach ionization threshold after a few scattering events.

Since this theory accounts for realistic scattering mechanisms and band structures, it can be applied to any semiconductor. Shichijo and Hess [11] also calculated the electron-ionization rate in GaAs versus crystal orientation and concluded that within the statistical uncertainty of their calculations (± 20 %), no orientation dependence of impact ionization for electric fields larger than 3.3×10^6 V/cm was found. They explained this as follows: At high electric fields and at steady state, electrons are scattered all over the Brillouin zone before reaching threshold, so any "memory" of the orientation of the electric field or the effect of the anisotropy of the conduction band are lost.

Recently, Ridley [12] has developed a simple analytical theory of impact ionization (the "lucky drift model"), giving results that are in excellent agreement with Baraff's theory [10]. The basis of his approach is the distribution between the rates of momentum relaxation τ_m and energy relaxation τ_E. If we have, as generally is the case, $\tau_m(\tau) << \tau_E(E)$, then it is possible for electrons to drift in an electric field with a drift velocity limited by momentum-relaxation collisions, without there being in the same period any significant energy relaxation. This is called lucky drift, and it is intermediate between Shockley's ballistic state and Wolff's equilibrium state, each of which is valid in a distinctive time domain and which can be characterized as follows [12]:

$0 < t < \tau_m(\tau)$; ballistic motion regime
$\tau_m(\tau) \leq t \leq \tau_E(E)$; lucky drift regime
$\tau_E(E) \leq t$; steady state regime

2.1.3. Impact Ionization Threshold Energy

Impact ionization can occur in a semiconductor when free carriers (electrons and holes) are accelerated by a high electric field until they gain sufficient energy to create an electron-hole pair by the generation of an electron from the valence band to the conduction band.

The minimum energy needed for impact ionization is the ionization threshold energy E_{th}. The value of the threshold energy depends on the band structure of the semiconductor. The conditions for an impact ionization process to occur at threshold were first established by Keldysh [13]. Anderson and Crowell [14] developed an algorithm to determine the threshold condition for a general type of band structure. Using the same methods, Pearsall [15] obtained the relation between the impact ionization threshold energy, the energy band gap, and the effective masses of the carriers (electrons and holes) for GaAs and GaSb.

In the following we will review the above-mentioned papers by Anderson and Crowell and by Pearsall et al. [14,15].

2.1.3.1. Conditions for Threshold.

Fig. 2.1 shows a general band structure of a direct bandgap semiconductor with an impact ionization process indicated. An initial electron in the conduction band makes a transition from state $i(E_i,k_i)$ to state $1(E_1,k_1)$, promoting an electron to state $2(E_2,k_2)$ and resulting in a hole in the valence band state $3(E_3,k_3)$. The two key requirements in order for impact ionization to occur are in terms of electronic quantities:

(1) conservation of energy, i.e.

$$E_i + E_v(k_3) = E_c(k_1) + E_c(k_2) \qquad (2.12)$$

(2) Conservation of momentum

$$\hbar k_i + \hbar k_3 = \hbar k_1 + \hbar k_2 \qquad (2.13)$$

As Anderson and Crowell [14] have shown, the threshold energy is determined by minimizing the energy of the initial particle with respect to small changes in the wave vectors of the particles (carriers) involved. Satisfying the restrictions of conservation of energy and

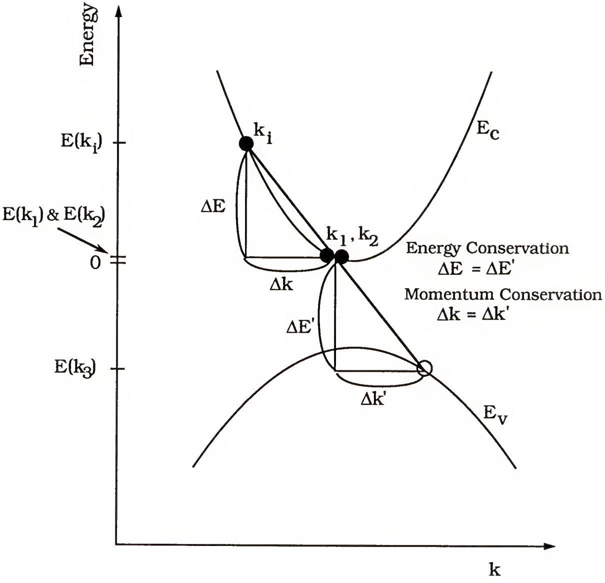

Figure 2.1 Simple three band E-k diagram showing the electron-initiated impact ionization.

conservation of momentum, we find for the threshold energy E_i

$$dE_i = 0 = dk_1 \cdot \nabla_k E(k_1) + dk_2 \cdot \nabla_k E(k_2) - dk_3 \cdot \nabla_k E(k_3) \quad (2.14)$$

and for a given k_i

$$dk_i = 0 = dk_1 + dk_2 - dk_3 \quad (2.15)$$

Substituting Eq. (2.15) into(2.14) and recognizing $\nabla_k E(k)/\hbar$ as a group velocity, we find

$$dk_2 \cdot (v_2 - v_1) + dk_3 \cdot (v_1 - v_3) = 0 \quad (2.16)$$

To satisfy Eq. (2.16) for arbitrary dk_2 and dk_3, one requires

$$v_1 = v_2 = v_3 \quad (2.17)$$

That is, a necessary condition for an impact-ionizing carrier to have minimum energy is that all final carriers have equal group velocities or lie on the same axis in E-k diagram [14]. Note that this axis should include the initial state.

2.1.3.2. Calculation of Ionization Threshold for Simple Models.

To get a functional expression showing how the threshold energies depend on the parameters of the band structure, we study the following simple models.

(a) Two Parabolic Bands

As Fig. 2.1 shows, we consider one conduction band with effective mass m_e and valence band with effective mass m_h; $m_e, m_h > 0$. Using the threshold condition Eq. (2.17), we obtain the following relationship between the wave vectors of the final particles using that the mass of an electron in the valence band is equal to $- m_h$

$$k_1 = k_2 = -k_3 \frac{m_e}{m_h} \tag{2.18}$$

Also, because of momentum conservation,

$$k_i = 2k_1 - k_3 = k_1 (2 + \frac{m_h}{m_e}) \tag{2.19}$$

If we choose the bottom of the conduction band as our reference, it should hold that

$$E_i = \frac{\hbar^2 k_i^2}{2m_e} = \frac{\hbar^2 k_1^2}{2m_e} (2 + \frac{m_h}{m_e})^2 = E_{th,e} \tag{2.20}$$

where $E_{th,e}$ denotes the electron-initiated threshold energy. Note that k_1 is unknown and needs to be eliminated.

Using energy conservation, E_i can be expressed in terms of the final particle energies in the following way:

$$\begin{aligned} E_i &= \frac{\hbar^2 k_1^2}{2m_e} + \frac{\hbar^2 k_2^2}{2m_e} + \frac{\hbar^2 k_3^2}{2m_h} + E_g \\ &= \frac{\hbar^2}{2m_e} (2k_1^2 + k_3^2 \frac{m_e}{m_h}) + E_g \end{aligned}$$

$$= \frac{\hbar^2 k_1^2}{2m_e}\left(2 + \frac{k_3^2}{k_1^2}\frac{m_e}{m_h}\right) + E_g \qquad \left(\text{Note: } \frac{k_3}{k_1} = -\frac{m_h}{m_e}\right)$$

$$= \frac{\hbar^2 k_1^2}{2m_e}\left(2 + \frac{m_h}{m_e}\right) + E_g = E_{th,e} \qquad (2.21)$$

Eliminating k_1 from Eqs. (2.20) and (2.21) leads to the following result for $E_{th,e}$:

$$E_{th,e} = E_g\left(1 + \frac{m_e}{m_e + m_h}\right) \qquad (2.22)$$

Similarly, one finds for the hole-ionization threshold

$$E_{th,h} = E_g\left(1 + \frac{m_h}{m_e + m_h}\right) \qquad (2.23)$$

From these results some interesting conclusions can be drawn. As expected, the threshold energy depends primarily on the bandgap and the effective masses. Since the effective mass is a function of the crystal orientation, one might expect that the threshold energy will also depend on crystal orientation. Shichijo and Hess [11] showed, however, that this effect is lost in the acceleration history of the initiating particle.

In addition, it is worth noting that when $m_e = m_h$,

$$E_{th,e} = E_{th,h} = \frac{3}{2} E_g \qquad (2.24)$$

which is the well known 3/2- bandgap rule [8].

(b) Three Simple Parabolic Bands

We consider a more sophisticated model by adding another valence band for light holes (shown in Fig. 2.2). We assume that an initiating hole (k_i) is located in the light-hole valence band. After impact ionization we have two holes (k_2, k_3) in the heavy-hole valence band and one electron in the conduction band (k_1).

In terms of electron parameters we have that before the impact ionization process k_2 and k_3 are occupied. After the ionization process k_1 and k_i become occupied. Hence

$$k_i + k_1 = k_2 + k_3 \qquad (2.25)$$

which can be rewritten as

$$k_i = 2k_{v,1}\left(\frac{m_{hh}}{m_{le}}\right) + k_{v,1}\left(\frac{m_e}{m_{lh}}\right) = k_{v,1}\left(\frac{2}{\gamma_1} + \frac{1}{\gamma_2}\right) \qquad (2.26)$$

where m_{lh} and m_{hh} denote the light-hole effective mass and the heavy-hole effective mass, respectively.

Before ionization the kinetic energy of the initiating hole is

$$E_i = \frac{\hbar^2 k_i^2}{2m_{lh}} = \frac{\hbar^2 k_{v1}^2}{2m_{lh}}\left(\frac{2}{\gamma_1} + \frac{1}{\gamma_2}\right)^2 = E_{th,h} \qquad (2.27)$$

where $E_{th,h}$ represents the hole-initiated threshold energy. After impact ionization we have two holes and an electron. From energy conservation $E_i + E_1 = E_2 + E_3$ and

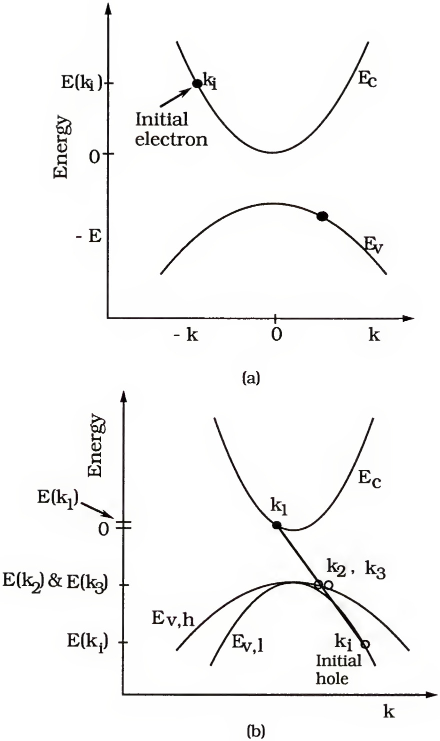

Figure 2.2 E-k diagram with impact ionization processes:
(a) primary particle before ionization
(b) resultant particles immediately after ionization.

with choosing the top of the heavy hole band as energy reference we find for the minimum of E_i

$$
\begin{aligned}
E_i &= -\frac{\hbar^2 k_1^2}{2m_e} + \frac{\hbar^2 k_2^2}{2m_e} - \frac{\hbar^2 k_3^2}{2m_h} + E_g \\
&= \frac{\hbar^2}{2m_{hh}} \left(2k_2^2 + k_1^2 \frac{m_{hh}}{m_e}\right) + E_g \\
&= \frac{\hbar^2 k_{vl}^2}{2m_{lh}} \left(2\frac{m_{lh}}{m_{hh}} \frac{k_{vh}^2}{k_{vl}^2} - \frac{m_{lh}}{m_e} \frac{k_1^2}{k_{vl}^2}\right) + E_g \\
&= \frac{\hbar^2 k_{vl}^2}{2m_{lh}} \left(2\gamma_1 \frac{1}{\gamma_1^2} + \gamma_2 \frac{1}{\gamma_2^2}\right) + E_g \\
&= \frac{\hbar^2 k_{vl}^2}{2m_{lh}} \left(\frac{2}{\gamma_1} + \frac{1}{\gamma_2}\right) + E_g = E_{th,h} \qquad (2.29)
\end{aligned}
$$

Eliminating k_{vl}^2 from Eqs.(2.27) and (2.28) leads to

$$E_{th,h} = E_g\left(1 + \frac{m_{lh}}{2m_{hh} + m_e - m_{lh}}\right) \qquad (2.30)$$

Since the electron-initiating ionization process is identical to the case of two parabolic bands, we have

$$E_{th,e} = E_g\left(1 + \frac{m_e}{m_e + m_{hh}}\right) \qquad (2.30)$$

(c) Three Simple Parabolic Bands with Spin-orbit Splitting of the Light-hole band

We can make the model more realistic by considering two valence bands, one for heavy holes with effective mass m_h and the other separated toward lower energy by an amount Δ due to the spin-orbit coupling with effective mass m_{lh} (Fig. 2.3).

From the momentum conservation principle we obtain the wave vector relationship where we mix electron and hole parameters as is usually done in the literature

$$k_i + k_1 = k_2 + k_3 \tag{2.25}$$

Each wave vector can be specified as follows:

k_i : wave vector of initiating hole in the light valence band

$k_2 = k_3 = k_{v,h}$ (in the heavy-hole valence band)

$k_1 = k_c$ (in the conduction band).

In addition one can derive from Eq. (2.17)

$$k_2 = \frac{1}{\gamma_1} k_{v,l}, \text{ where } \gamma_1 = \frac{m_{lh}}{m_{hh}} \tag{2.31}$$

$$k_1 = \frac{1}{\gamma_2} k_{v,l}, \text{ where } \gamma_2 = \frac{m_{lh}}{m_e} \tag{2.32}$$

Substitution of Eqs. (2.31) and (2.32) into (2.25) gives

$$k_i = k_{v,l}\left(\frac{2}{\gamma_1} + \frac{1}{\gamma_2}\right) \tag{2.33}$$

Before impact ionization occurs, the total energy of the initiating hole in the valence band can be expressed as

$$E_i = \Delta + \frac{\hbar^2 k_i^2}{2m_{lh}} = \Delta + \frac{\hbar^2 k_{vl}^2}{2m_{lh}}\left(\frac{2}{\gamma_1} + \frac{1}{\gamma_2}\right)^2 = E_{th,h} \tag{2.34}$$

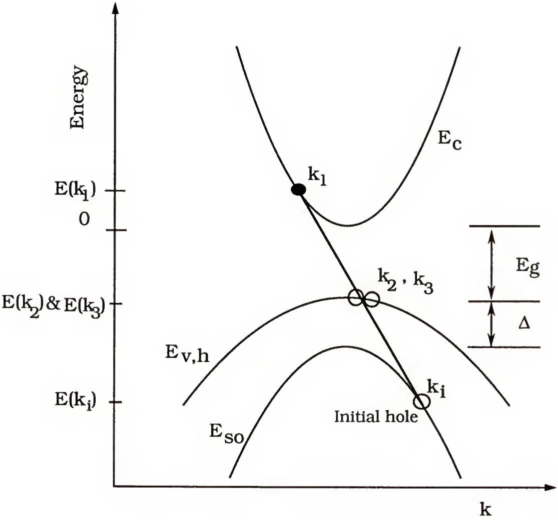

Figure 2.3 E-k diagram showing the impact ionization initiated by the hole in the spin-orbit band.

Solving for $k_{v,1}^2$ from Eq. (2.34) gives

$$k_{v,1}^2 = \frac{E_{th} - \Delta}{(2/\gamma_1 + 1/\gamma_2)^2} \frac{2m_{lh}}{\hbar^2} \qquad (2.35)$$

From the energy conservation principle, we find for the minimum of E_i

$$\begin{aligned} E_i &= E_g + (K\cdot E)_{2-h} + (K\cdot E)_{1-e} \\ &= E_g + \frac{\hbar^2 k_{vl}^2}{2m_{lh}}\left(2 \frac{m_{lh}}{m_{hh}} \frac{k_{vh}^2}{k_{vl}^2} - \frac{m_{lh}}{m_e} \frac{k_c^2}{k_{vl}^2}\right) \\ &= E_g + \frac{\hbar^2 k_{vl}^2}{2m_{lh}}\left(\frac{2}{\gamma_1} + \frac{1}{\gamma_2}\right) = E_{th,h} \qquad (2.36) \end{aligned}$$

In the third line we used Eqs. (2.31) and (2.32). When we substitute Eq. (2.35) into (2.36), we obtain for the spin orbit (s.o), hole-initiated threshold energy:

$$E_{th,h} = E_g\left(1 + \frac{m_{lh}(1 - \Delta/E_g)}{2m_{hh} + m_e - m_{hh}}\right) \qquad (2.37)$$

The electron-initiated threshold energy is unchanged and has the same form as in the previous case:

$$E_{th,h} = E_g\left(1 + \frac{m_e}{m_e + m_{hh}}\right) \qquad (2.38)$$

For a material in which $E_g = \Delta$, $E_{th,h}$ equals the bandgap, and $k_i = k_1 = k_2 = k_3 = 0$. In other words, the zero momentum transferred in this vertical transition reduces the threshold energy and increase β. This effect is referred to as resonant enhancement of the hole-ionization rate and was experimentally observed in $Al_xGa_{1-x}Sb$ alloys by Hildebrand et al. [16,17] near x = 0.065. His experimental values for β/α are plotted in Fig. 2.4. As Δ/E_g approaches unity, β becomes much larger than α. For $\Delta/E_g = 1.02$, $\beta/\alpha = 20$ at $\mathcal{E} = 3.3 \times 10^4$ V/cm^{-1}. This enhancement of β/α leads to a very low excess noise factor for long wavelength (1.55 μm) APD's.

Recently, Brennan et al. [18] found from Monte Carlo simulations that the minimum in the hole-ionization energy for $\Delta = E_g$ accounts only for a small part of the resonant enhancement of β. Another important requirement for the enhancement of β to occur is that the hole-ionization threshold energy ($E_{th,h}$) must be very high (1.4 eV) in both the light- and heavy-hole bands.

Brennan et al. [18] explained that β/α enhancement can only be accomplished if enough holes are scattered into the split-off band before they ionize from either the heavy- or the light-hole band. For that to occur, it is necessary for the holes to drift to a sufficiently high energy where the density of states of the split-off band is appreciable. Therefore, in order for the resonance to occur, $E_{th,h}$ must be high for both the heavy- and light-hole bands (~ 1.4 eV).

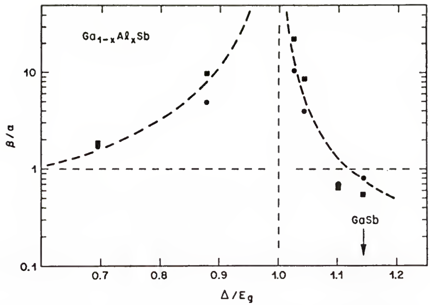

Figure 2.4 The ionization coefficient ratio β/α plotted versus Δ/E_g (Ref. 17)

(d) A Nonparabolic Conduction Band and One-parabolic Valence Band

The conduction band central valley in III-V materials can be quite well represented by

$$\frac{\hbar^2 k^2}{2m_e} = E(1 + \alpha' E) \qquad (2.39)$$

where α' is a measure for the deviation of the E(k) band from a parabolic shape. Ridley [19] showed that the threshold energy for electrons becomes in this case

$$E_{th,e} = E_g\left(\frac{1 + 2\mu}{1 + \mu}\right) \left[1 + \frac{\mu(1 + 2\mu)}{(1 + \mu)^2} \alpha' E_g\right] \qquad (2.40)$$

where μ is m_e/m_h, and m_e and m_h are the electron and hole effective masses respectively.

For example, for GaAs, $\mu = 0.149$ and $\alpha = 0.64\ \mathrm{eV}^{-1}$. Substitution of these values into Eq. (2.40) yields $E_{th,e} = 1.82$ eV. Landsberg and Yu [20] found a more accurate expression for the threshold energy of electron-electron-hole impact ionization, given by

$$E_{th,e} = E_g \cdot \frac{1 + \mu}{2\mu\alpha'} \left[1 + \sqrt{1 - \frac{4\mu(1+2\mu)}{(1+\mu)^2} \alpha' E_g}\ \right] \qquad (2.41)$$

When we substitute above values into Eq. (2.41), we obtain $E_{th,e} = 1.95$ eV, which is in better agreement with experimental findings. The derivation and a more detailed discussion of expression (2.41) will be presented in Chapter IV.

2.2 Noise Theory

2.2.1. The Binomial Process

Let an experiment be tried m times. Let p be the probability that the trial is successful and 1 - p the probability that it fails. Let there be n successes for the m trials, then

$$\bar{n} = mp \qquad (2.42)$$

$$\text{var } n = mp(1 - p)$$

and the probability distribution is given by

$$P_m(n) = \frac{m!}{n!(m - n)!} p^n (1 - p)^{m-n} \qquad (2.43)$$

This is called the binomial law.

For example, in terms of a photodiode, a "trial" is equal to the absorption of a photon by the p-n junction, "success" is when the generated electron-hole pair is collected.

2.2.2. Poisson Process

The photon detection by a photodiode or the emission of a photon in the visible wavelength spectrum can be described as a Poisson process [21]. If the arrival of photons at the detector can be described as a series of independent events occurring at random instants, then the binomial distribution reduces to the Poisson distribution as will be shown in the following.

If m goes to infinity and p goes to zero ($mp = \bar{n}$ is kept constant), then Eq. (2.43) can be approximated as

$$P_m(n) = \frac{m(m-1)\cdots(m-n+1)}{n!}\, p^n (1-p)^{m-n} \quad \text{(where we divided out the term } (m-n)!\text{)}$$

$$\simeq \frac{m^n\ p^n\ (1-p)^{m-n}}{n!}$$

$$= \frac{\bar{n}}{n!}(1-p)^{m-n}$$

Define $(1-p)^{m-n} = x$, then $(m-n)\ln(1-p) = \ln(x)$, or with $p \to 0$ $\ln(1-p) \sim -p$ and $x = e^{-mp}e^{+np} = e^{-n} \cdot 1$. Consequently, we derive at

$$P(n) = \frac{(\bar{n})^n}{n!}\exp(-\bar{n}) \tag{2.44}$$

$$\frac{m!}{n!(m-n)!}\, p^n (1-p)^{m-n} \approx e^{-mp}\frac{(mp)^n}{n!} \tag{2.44}$$

which is the Poisson distribution. The variance of a Poisson distribution is given by

$$\text{var } n = \bar{n} \tag{2.46}$$

2.2.3. Variance Theorem

We consider the electron multiplication process as it occurs in the avalanche region of an APD.

Let N be the number of electrons arriving at the device. Let X_i be the number of secondary electrons (offspring) produced the i^{th} primary electron. Let a second quantity n be defined by

$$n = \sum_{i=1}^{N} X_i \qquad (2.47)$$

Since all of the primary electrons have the same a priori probability for multiplication, it follows that

$$\overline{X_i} = M \; ; \quad \overline{X_i^2} = \overline{X^2} \qquad (2.48)$$

independent of i, where M is the gain. Let N and X_i both fluctuate; then

$$\bar{n} = \overline{NX} = \overline{N}M \qquad (2.49)$$

$$\text{var } n = M^2 \text{ var } N + \overline{N} \text{ var } X$$

which is called Burgess' variance theorem [21].

If we make use of the fact that var N = $\overline{N}$ (Poisson), then Eq. (2.48) reduces to

$$\text{var } n = \overline{NX^2} \qquad (2.50)$$

Assume that the currents flowing in the device show full-shot noise, then we have the following correspondences:

var n corresponds to $S_{I_d} = 2qI_d$: S_{Id} is the noise spectral density of diode current

var $\overline{N}$ corresponds to $S_{I_{pr}} = 2qI_{pr}$: $S_{I_{pr}}$ is the noise spectral density of primary current.

Then Eq. (2.48) can be rewritten as

$$S_{I_d} = M^2 S_{I_{pr}} + S_{I_{pr}} \text{ var } X \qquad (2.51a)$$

or

$$S_{I_d} = S_{I_{pr}} (M^2 + \text{var } X) \qquad (2.51b)$$

The first term of Eq. (2.51a) represents amplified primary noise, and the second term is identified as multiplication noise [21].

Tager [22] and McIntyre [23,24] showed that var X is given by

$$\mathrm{var}\ X = M^2(M-1):\ \text{Tager (equal ionization probabilities)} \tag{2.52}$$

$$\mathrm{var}\ X = M(M-1) + k(M-1)^2M:\ \text{McIntyre} \tag{2.53}$$

where $k = \beta/\alpha$

If we substitute Eq. (2.52) into (2-51), we get

$$S_{I_d} = S_{I_{pr}}\ [M^2 + M^2(M-1)] = S_{I_{pr}}M^3 \tag{2.54}$$

This is the result Tager obtained [22]. In the following sections Eqs. (2.52) and (2.53) will be discussed in more detail.

2.2.4. Excess Noise Factor, F

We rewrite Eq. (2.51) by using the definition of a variance and obtain

$$\begin{aligned} S_{I_d} &= S_{I_{pr}}\overline{X^2} \\ &= S_{I_{pr}}(\overline{X})^2F \\ &= S_{I_{pr}}M^2F \end{aligned} \tag{2.55}$$

where F is known as the excess noise factor. F is a measure for the amount by which the noise exceeds that of an ideal current multiplier. To clarify the meaning of F, we will consider the following example.

Let an input signal have the current value I_{ph}; then, after multiplication the output signal current becomes

$$I_{out} = I_{ph}M \qquad (2.56)$$

If we have an ideal, noise-free amplifier, the input current noise would be amplified by a factor M; hence

$$\sqrt{2qi_N\Delta f}_{output} = \sqrt{2qI_{ph}\Delta f}\cdot M \qquad (2.57)$$

Squaring both terms in Eq. (2.57) yields

$$S_{I_{ph}} = S_{I_{pr}}M^2 \qquad (2.58)$$

By comparing Eq. (2.58) with (2.55), we can deduce that for an ideal current multiplier the excess noise factor reduces to unity.

However, in reality nonideality exists for which the second term (multiplication noise) of Eq. (2.50) is responsible. Therefore, the noise level increases by $(MF)^{1/2}$.

The excess noise factor F is always greater than unity and is an increasing function of M. The value of F depends upon the detailed characteristics of the avalanche junction and upon the nature of the primary excitation: hole injection, electron injection or mixed injection.

Tager [22] showed that for equal ionization coefficients of electrons and holes the noise spectral density is given by

$$S_{I_d} = 2qI_{pr}M^3 \qquad (2.53)$$

where it is assumed that the incoming particles show full-shot noise. By equating Eqs. (2.53) and (2.55) we have F =M.

McIntyre extended the analysis to the case of unequal ionization coefficients [23]. He assumed that the relation between these two is $k = \beta/\alpha$ and is independent of the field strength. The noise spectral density is then given by

$$S_{I_d} = 2qI_{pr}M^3[1 - (1-k)(\frac{M-1}{M})^2] \qquad (2.60)$$

By equating Eqs. (2.60) and (2.55) we can obtain the expression for the excess noise factor

$$F = M[1 - (1-k)\frac{(M-1)^2}{M^2}] \qquad (2.61a)$$

whereas Tager's theory results in

$$F = M \qquad (2.61b)$$

For later use we rewrite the excess noise factor as follows:

$$F = \frac{\overline{X^2}}{M^2} \tag{2.62}$$

$$F = 1 + \frac{\text{var } X}{M^2} \tag{2.63}$$

Eq. (2.62) follows from Eq. (2.55), and Eq. (2.63) is obtained by equating Eq. (2.51) and Eq. (2.55).

2.2.5. Generating Functions and Compounding Theorem

1) Generating Functions

For random variables whose only possible values are non-negative integers, for example, 0 and 1 in the Bernouilli process and 0, 1, 2,· · · in the binomial counting process, a function related to the characteristic function is the generating function [25] of the Fowler-type of variable k defined by

$$\begin{aligned} g(s) &= \sum_{k=0}^{\infty} p_k s^k \\ &= E[s^k] \end{aligned} \tag{2.90}$$

here p_k = probability.

The generating function of a non-negative, integer valued, random variable k is formally related to the characteristic function ϕ of k through the change of variable $s = e^{it}$,

$$\begin{aligned} \phi(t) &= E[e^{it}] \\ &= E[(e^{it})^x] \\ &= g(e^{it}) \end{aligned} \tag{2.91}$$

Thus generating functions have the three basic properties of characteristic functions:

a) A generating function determines the distribution function uniquely.

b) The generating function of a sum of independent, non-negative, integer valued, random variables is the product of their generating functions.

c) The moments may be obtained through successive differentiation.

2) Compounding Theorem

Let N, X_1, X_2, · · · be independent non-negative integer valued random variables and suppose we wish to determine the generating function $g_R(s)$ of the sum $R = X_1 + X_2 + \cdot \cdot \cdot + X_N$.

Let $g_N(s)$ be the generating function of N and suppose that all X_i have the same distribution functions with the common generating function g(s).

Then,

$$\begin{aligned} g_R(s) &= E[s^R] \\ &= E[s^{x_1+x_2+\cdot \cdot \cdot+x_N}] \\ &= E\{E[s^{x_1+x_2+\cdot \cdot \cdot+x_N}|N|\} \\ &= \sum_{n=0}^{\infty} E[s^{x_1+x_2+\cdot \cdot \cdot+x_N}|N=n]P_r\{N=n\} \end{aligned}$$

$$= \sum_{n=0}^{\infty} E[s^{x_1+x_2+\cdot\cdot\cdot+x_N}]P_r\{N=n\}$$

(since N and X_i are independent)

$$= \sum_{n=0}^{\infty} g(s)^n P_r\{N=n\}$$

$$= E[g(s)^N] \qquad (2.92)$$

Therefore,

$$g_R(s) = g_N[g(s)] \qquad (2.93)$$

This is the compounding theorem. If we consider the avalanche multiplication process, then

X corresponds to the number of offsprings,

N corresponds to the number of incoming carriers,

and

R corresponds to the total number of carriers, M, collected after multiplication.

The compounding theorem is a very useful tool to analyze the branching process in APD's and is used as a central tool by C.M. Van Vliet et al. [26,27] to formulate the multiplication noise.

2.2.6. General Theory of Avalanche Noise by Van Vliet and Rucker

Contrary to the standard theories [22,23,24,28] which treat the impact ionization of carriers as a continuous spatial process, Van Vliet et al. [26,27] developed a new general theory employing the method of recurrent generating functions. This theory is quite general, since it covers the single-carrier process as well as the two-carrier process, from N = 1 to N = ∞, where N is the number of possible multiplications. Therefore, the results by Tager [22], McIntyre [26,27], Personick [28], and others are found to be special cases of this theory. One of the important features of Van Vliet's theory is that it properly describes the transition from continuum device physics to discrete device physics. The description of this transition is important in many modern devices. Since this theory is based on a finite number of discrete ionization processes, the result is also entirely discrete. Van Vliet predicted the presence of discrete steps in the noise for a finite number of possible multiplications in the avalanche region. J. Gong [29] verified this by measurements.

In this section we will outline the principles and the results. The theory starts from the following assumptions:

1) Ionization can take place after an energy gaining path l_1, with $l_1 = E_{th}/q|\mathcal{E}_i|$, where E_{th} is the ionization threshold energy and $\mathcal{E}_i$ is the average electric field in the interval l_1.

2) The number of possible ionizations per carrier transit is finite since we can divide the avalanche region w into N sections of length l_i, such that $w = \sum_{i=1}^{N} l_i$.

3) The a priori chance for electron-initiated ionization after an energy-gaining path l_1 is λ_i. In the same fashion we define a priori chance μ_i for holes.

4) After each collision all energy is lost and the momentum is randomized, so that each possible ionization during the successive paths $l_i \cdot \cdot \cdot l_N$ is governed by an independent Bernouilli trial. Note: This assumption needs to be modified a little bit according to the theories [11,12] discussed in the previous section (see impact ionization mechanism).

A. One-carrier Process Let N be the number of possible ionizations per primary carrier transit and consider only the electrons in this process as shown in Fig. 2.5. We consider the subtrees arising from the first, second, $\cdot \cdot \cdot$, Nth ionization event of the incoming carrier. These subtrees are denoted by Y_N, Y_{N-1}, $\cdot \cdot \cdot$, Y_1, respectively; thus

$$X \equiv X_N = 1 + Y_N + Y_{N-1} + \cdot \cdot \cdot + Y_1.$$

We now observe that the subtree Y_N is identical to the tree X, except that only a maximum of N - 1 ionizations can occur and that the subtree is "fed" by a Bernouilli trial (Fig. 2.6). If g_N and ϕ_N denote the generating functions of Y_N and X_N, respectively, then the compounding theorem gives [see Appendix A]

$$g_N(z) = \omega[\phi_{N-1}(z)] \tag{2.94}$$

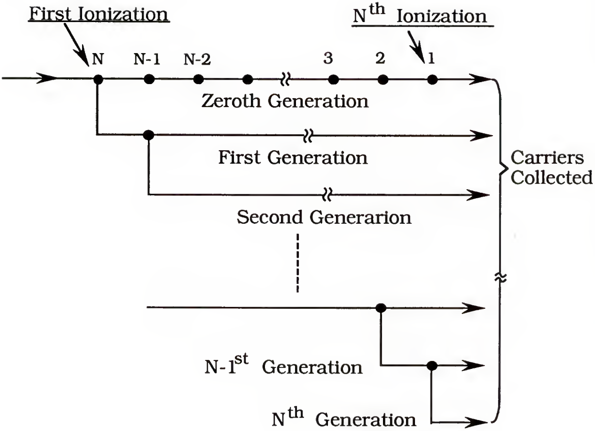

Figure 2.5 Impact ionization process involving N possible ionizations per transit of the primary carrier.

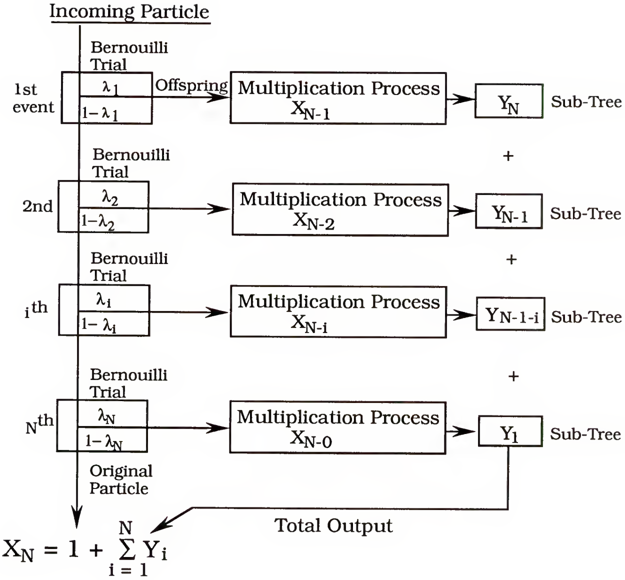

Figure 2.6 Diagram of the one-carrier multiplication process.

where ω is the generating function for a Bernouilli trial with a priori chance λ_i. Thus

$$g_N(z) = \lambda\phi_{N-1} - \lambda + 1 \tag{2.95}$$

In general, for branch i

$$g_{N-i+1}(z) = \omega_i[\phi_{N-i}(z)] = \lambda_i\phi_{N-i}(z) - \lambda_i + 1 \tag{2.96}$$

We also know from looking at Fig. 2.6,

$$X_N = 1 + \sum_{j=1}^{N} y_j$$

Then in terms of generating functions

$$\phi_N = z\sum_{j=1}^{N} g_j \tag{2.97}$$

where $g_o = z$. In a similar way

$$\phi_{N-1} = z\sum_{j=1}^{N-1} g_j \tag{2.98}$$

Dividing Eq. (2.97) by (2.98), we have

$$\frac{\phi_N}{\phi_{N-1}} = g_N \tag{2.99}$$

By using Eqs. (2.95) and (2.99) we obtain

$$\phi_N(z) = \phi_{N-1}(z)[\lambda\phi_{N-1}(z) - \lambda + 1] \tag{2.100}$$

which is solved with the boundary condition $\phi_o(z) = z$. The following result for the multiplication factor M is found by iterating Eq. (2.100),

$$M = \phi_N'(1) = (1 + \lambda)^N \tag{2.101}$$

For the noise we find

$$\text{var } X = \phi_N''(1) - [\phi_N'(1)]^2 + \phi_N'(1) = \frac{1 - \lambda}{1 + \lambda} M(M-1) \tag{2.102}$$

Substitution of Eq. (2.99) yields

$$\text{var } X_N = (2 - M^{1/N})M^{1-1/N}(M - 1) \tag{2.103}$$

For N = 1, this becomes

$$\text{var } X_1 = (2 - N)(M - 1) \tag{2.104}$$

For $N \rightarrow \infty$,

$$\text{var } X_\infty = M(M - 1) \tag{2.105}$$

which is the Tager's result. The multiplication factor can also be found for the asymptotic case $N \rightarrow \infty$. Since $\lambda = \alpha w/N$, where $w/N = 1$, Eq. (2.99) reduces to

$$M_\infty = \lim_{N \rightarrow \infty} (1 + \frac{\alpha w}{N})^N = e^{\alpha w} \tag{2.106}$$

B. Two-carrier Process. First we assume that a primary electron comes in at a position (k,l) where it can create a hole-electron pair. Here k is the number of possible subsequent ionizations by the electron which moves to the right and l is the number of possible ionizations by the hole which moves to the left, thus $k + l = N$, see Fig. 2.7. The total number of hole-electron pairs due to the pair coming in at (k,l), including this original pair, will be denoted as $X_{k,l}$ and given by

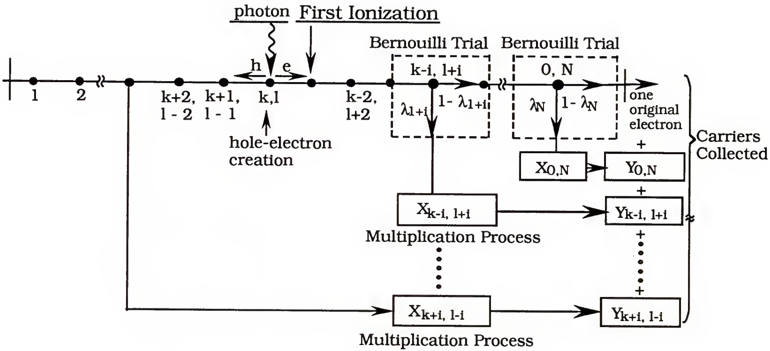

Figure 2.7 Diagram of the two-carrier multiplication process.

$$X_{k,l} = 1 + y_{k-1,l+1} + y_{k-2,l+2} + \cdot\cdot\cdot + y_{0,N} + y_{k+1,l-1} + y_{k+2,l-2} + \cdot\cdot\cdot + y_{N,0} \quad (2.107)$$

Let $\phi_{k,l}(z)$ be the generating function of X_k, then $\phi_{k,l}(z)$ can be expressed by the product of generating functions of subtrees as follows:

$$\phi_{k,l}(z) = zg_{k-1,l+1} \cdot g_{k-2,l+2} \cdot \cdot \cdot g_{k+1,l-1} \cdot g_{k+2,l-2} \cdot \cdot \cdot g_{N,0} \quad (2.108)$$

or

$$\phi_{k,l}(z) = z \prod_{j=1}^{k} g_{k-j,l+j} \cdot \prod_{j=1}^{l} g_{k+j,l-j} \quad (2.109)$$

By letting $k \rightarrow k + 1$, $l \rightarrow l - 1$,

$$\phi_{k+1,l-1}(z) = z \prod_{j=1}^{k} g_{k+1-j,l-1+j} \cdot \prod_{j=1}^{l} g_{k++1+j,l-1-j} \quad (2.110)$$

Dividing Eq. (2.109) by (2.110), we find the ratio

$$\frac{\phi_{k,l}}{\phi_{k-1,l+1}} = \frac{g_{k+1,l-1}}{g_{k,l}} \quad (2.111)$$

Now the generating function $g_{k-1,l+1}$ of $y_{k-1,l+1}$ is identical to that of $X_{k-1,l+1}$ except that the "feeding" is by a Bernouilli trial of a priori chance λ_{l+1}; thus according to the compounding theorem, it is given by $\lambda_{l+1}\phi_{k-1,l+1} - \lambda_{l+1} + 1$. likewise, the subtree $y_{k+1,l-1}$ is identical to that of $X_{k+1,l-1}$, except that the feeding is by a Bernouilli trial of a priori chance μ_{l-1}, resulting in a generating function $\mu_{l-1}\phi_{k+1,l-1} - \mu_{l-1} + 1$. Therefore, Eq. (2.111) reduces to the recurrent relation as

$$\phi_{k,l}(z)\,[\lambda_l\phi_{k,l}(z) - \lambda_l + 1] = \phi_{k+1,l-1}[\mu_{l-1}\phi_{k+1,l-1}(z) - \mu_{l-1} + 1] \tag{2.112}$$

When k = N, l = 0, we have the case of an electron-hole pair coming in at the left. However, the hole so introduced is immediately carried off at the negative electrode at the left. So this situation is equivalent to the case that only an electron comes in at the left and collected at the right after multiplications. Therefore, once we know the generating function $\phi_{N,0}$, we can find the mean (i.e., multiplication factor, M) and var X by calculating the first and second derivatives of $\phi_{N,0}(z)$ at z = 1, respectively. Thus

$$M = \langle X_{N,0}\rangle = \phi'_{N,0}(1) \tag{2.113}$$

$$\begin{aligned} \text{var } X_{N,0} &= \phi''_{N,0}(1) - [\phi'_{N,0}(1)]^2 + \phi'_N(1) \\ &= \phi''_{N,0}(1) - M^2 + M \end{aligned} \tag{2.114}$$

Eq. (2.112) is used to find the generating function $\phi_{N,0}$. But the algebra involved in Eqs. (2.113) and (2.114) is quite long and complex. Hence we will skip the derivation and show the important results below.

$$M = \frac{(1+\lambda)^N(1-k)}{(1+k\lambda)^{N+1} - k(1+\lambda)^{N+1}} \qquad \text{where } k = \frac{\mu}{\lambda} \qquad (2.115)$$

$$M_\infty = \frac{\alpha - \beta}{\alpha\left(\frac{1 + \beta w/N}{1 + \alpha w/N}\right)^N - \beta} \sim \frac{\alpha - \beta}{\alpha \exp(\beta-\alpha) - \beta} \qquad (2.116)$$

$$\text{var } X = \frac{M_N(M_N-1)(1-k)}{2 + \lambda + k\lambda}\left\{-\lambda + 2\,\frac{1-k\lambda^2}{1+k\lambda}\left[M_n k\,\frac{1+\lambda}{1-k} + \frac{1}{1+\lambda}\right]\right\} \qquad (2.117)$$

From Eq. (2.117) we can derive the following limiting cases:

(a) $N = 1$, $\text{var } X = \dfrac{\lambda(1-\lambda+3\mu+\lambda\mu)}{(1-\lambda\mu)^2}$ (Lukaszek) (2.118)

(b) $N = \infty$, $\text{var } X_\infty = M(M-1) + kM(M-1)^2$ (McIntyre)

(2.119)

(c) $\mu = 0$, $\text{var } X = \dfrac{1 - \lambda}{1 + \lambda} M(M-1)$ (one-carrier process)

(2.120)

2.2.7. Discrete Noise Characteristics of the Avalanche Photodiode

Many theories of avalanche noise (Tager [22] McIntyre [23] and Personick [28]) only deal with situations where the number of possible ionizations is very large. However, in many modern devices, where the depletion region is thin, the number of possible ionizations is finite and very small ($N = 1 \sim 5$).

As shown in the previous section, Van Vliet and Rucker developed a general theory which can be applied to such cases. To visualize the difference between two cases, we need to plot the curve for var X versus multiplication factor M.

Eq. (2.117) gives the expression for var X. To find var X as a function of M_N, we must eliminate λ with the help of Eq. (2.115). The results so obtained are shown in Fig. 2.8. It is clear that the noise is at all times below the McIntyre limit. It is also possible to construct an overall curve for var X in which N is the dependent variable.

The idea is as follows. For a given N, say $N = 1$, when the field increases $\lambda(1)$ increases, and so does var X_N. Since λ is bounded, $0 \leq \lambda < \lambda_{max} < 1$, var X cannot increase without switching to $N = 2$ if λ arrives at λ_{max}. Thus, the process switches over to $N = 2$, with $\lambda(2)$ being less than $\lambda_{1,max}$ in order to maintain the same gain; then $\lambda(2)$ increases up to $\lambda_{2,max}$, etc. Therefore, the plot of var X vs. M shows break points at such M values where λ is discontinuous, due to the regime switching from N to $N + 1$. Fig. 2.8 is obtained by piecewise fitting the results for $N = 1, 2, \cdots$ etc.

In 1980 J. Gong [29] measured the APD noise characteristics and experimentally verified the above theory. Instead of var X, he made a plot of var $X + M^2$ vs. M, which is identical to a plot of I_{eq} vs. I_d. To see this, we recall Eq. (2.63)

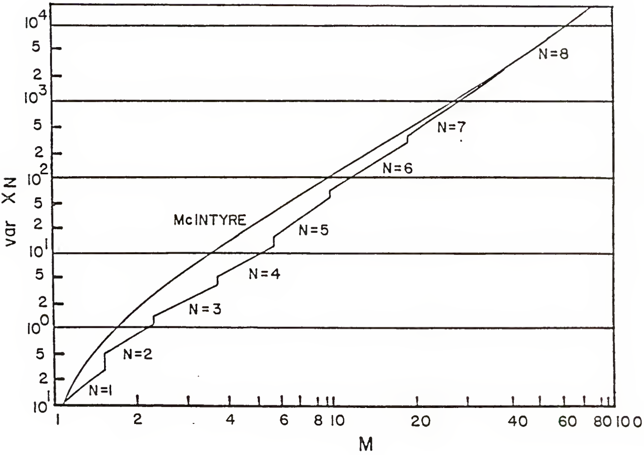

Figure 2.8 A plot of the var X versus multiplication factor M (Ref. 29).

$$F = 1 + \frac{\text{var } X}{M^2},$$

This equation can be rewritten as

$$FM^2 = \text{var } X + M^2 = \overline{X^2} \qquad (2.121)$$

If the primary current has shot noise, then

$$S_{I_d} = 2qI_{pr}\overline{X^2} = 2qI_{eq}$$

From this equation, we obtain the ratio

$$\frac{I_{eq}}{I_{pr}} = \text{var } X + M^2. \qquad (2.122)$$

Also

$$\frac{I_d}{I_{pr}} = M \qquad (2.123)$$

Dividing Eq. (2.112) by (2.113), we have

$$\frac{I_{eq}}{I_d} = \frac{\text{var } X + M^2}{M} \qquad (2.124)$$

Therefore, plotting var X + M^2 vs. M is a more convenient way to characterize the APD noise. One of Gong's plots is shown in Fig. 2.9 as an example.

2.2.8. Excess Noise Factors for the Staircase Avalanche Photodiode

The staircase APD (SAPD) was proposed by Capasso [30] and considered to be a solid-state analogy of photomultiplier tubes (PMT's). A detailed description of this device will be given in section III., 1-3. In this section, we are interested only in the derivation of the excess noise factor F of the SAPD.

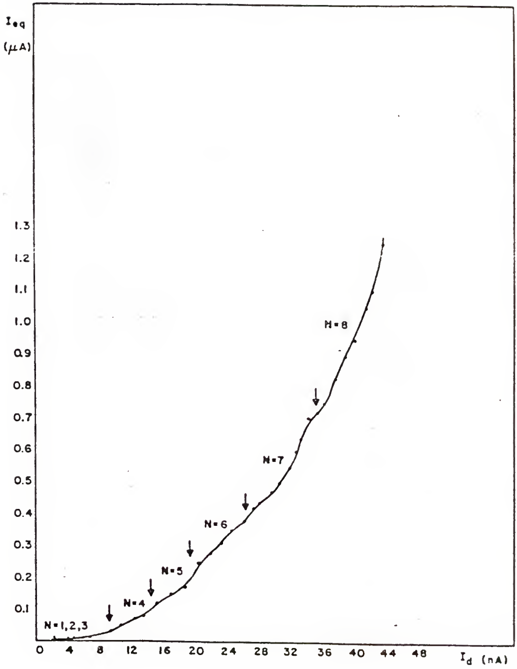

Figure 2.9 A plot of I_{eq} versus I_d (Ref. 29).

a) Derivation of F by Capasso. The band structure of a SAPD is shown in Fig. 2.10. Consider a photoelectron generated next to the p^+ contact. Under the combined action of the bias field $\mathcal{E}$ and the grading field $\Delta E_c/ql$, where ΔE_c is the conduction band step and l is the width of one step, the electron drifts toward the first conduction band step. The combined field $\mathcal{E} - \frac{\Delta \mathcal{E}_c}{ql}$ is small enough so that the electron does not impact ionize before it reaches the step. After the step, since $\Delta E_c \approx E_{th,e}$, the electron creates a hole-electron pair. This ballistic ionization process is repeated at each step.

Ideally, the avalanche gain per stage is 2. In practice, the gain is $2 - \partial$, where ∂ is the fraction of electrons which do not impact ionize. If N is the number of stages, the total gain is given by

$$<M> = (2 - \partial)^N. \qquad (2.125)$$

When we neglect the dark current, the noise spectral density is

$$S_{I_d} = 2qI_{pr}<M>^2 F(N,\partial), \qquad (2.126)$$

where F is the excess noise factor and is a function of N and ∂. If we write the shot noise generated by the n^{th} step as

$$S_{I,n} = 2q_{I_{n-1}} \mathrm{var}\ m, \qquad (2.127)$$

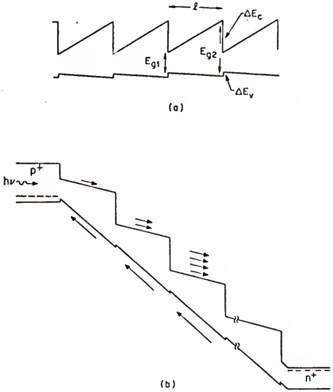

Figure 2.10 Band digram of the staircase avalanche photodiode (SAPD) (Ref. 6):
(a) SAPD is unbiased.
(b) SAPD is reverse biased.

where m is the gain of the n^{th} stage. Since we will deal with a binomial process (see section 2.2.1.),

$$<\partial^2> = \partial$$

$$<m^2> = <(2-\partial)^2> = <4 - 4\partial + \partial^2> = 4 - 3\partial \quad (2.128)$$

$$<m>^2 = (2-\partial)^2 = 4 - 4\partial + \partial^2 \quad (2.129)$$

Using Eqs. (2.128) and (2.129), eq (2.127) becomes

$$S_{I,n} = (\partial - \partial^2)\ (2qI_{n-1}) \quad (2.130)$$

where $I_{n-1} = I_o(2-\partial)^{n-1}$ is the average current into the n^{th} stage.

We assume that the noise contribution of the n^{th} stage $(1 \le n \le N)$ is multiplied noiselessly by the rest of the stages by a factor M^2, where M^2 is given by

$$M^2 = [(2-\partial)^{N-n}]^2 = (2-\partial)^{2(N-n)} \quad (2.131)$$

The total output noise per unit bandwidth is then

$$\begin{aligned} S_{I_d} &= 2qI_o(2 - \partial)^{2N} + S_{I,1}(2 - \partial)^{2(N-1)} \\ &\qquad + S_{I,2}(2 - \partial)^{2(N-2)} \\ &\qquad + \cdot \cdot \cdot \\ &\qquad + S_{I,N}(2 - \partial)^{0} \\ &= 2qI_o(2 - \partial)^{2N} + \sum_{n=1}^{N} 2qI_o(2-\partial)^{n-1}(\partial-\partial^2)\ (2-\partial)^{2(N-1)} \end{aligned}$$

$$= 2qI_o(2 - \partial)^{2N}[1 + \sum_{n=1}^{N} \frac{1}{(2-\partial)^n} \frac{\partial(1-\partial)}{(2-\partial)}] \quad (2.132)$$

By using the following summation formula for this geometrical series

$$S_N = \frac{a_1 - ra_N}{1 - r}, \quad r < 1 \quad (2.133)$$

Eq. (2.132) reduces to

$$S_{I_d} = 2qI_o(2 - \partial)^{2N}[1 + \frac{\partial\{1 - (2-\partial)^{-N}\}}{2 - \partial}]. \quad (2.134)$$

Therefore, the excess noise factor becomes

$$F(N,\partial) = 1 + \frac{\partial\{1 - (2-\partial)^{-N}\}}{2 - \partial} \quad (2.135)$$

This result is plotted in Fig. 2.11. If $\partial = 0$, i.e., all the electrons ionize at each step, F becomes unity. Therefore, this SAPD can in principle be a noise-free device.

b). Application of the Theory by Van Vliet et al. to SAPD's Van Vliet et al. [26,27] assumed that both electron- and hole-impact ionization occurs at discrete positions (see section II., 2-7). However, in SAPD's electrons impact-ionize at each step while holes impact-ionize at any position in the depletion region. Therefore,

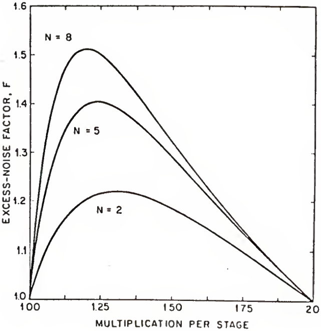

Figure 2.11 Excess-noise factor of the SAPD as a function of the multiplication per stage. N represents the number of stages. (Ref. 6).

we need to modify the assumption of impact ionization rates as follows.

λ: electron-impact ionization rate per stage

μ: hole-impact ionization rate per stage.

λ, μ are given by

$$\lambda = 1 - \partial \tag{2.136}$$

and

$$\mu = \exp[\int_0^L \beta dx] - 1 \tag{2.137a}$$

respectively, where L is the width of each step.

If β is very small, then

$$\mu = \overline{\beta} L \tag{2.137b}$$

where

$$\overline{\beta} = \frac{1}{L} \int_0^L \beta dx \tag{2.138}$$

The derivation of Eq. (2.137a) goes as follows. We assume that impact ionization caused by electrons between the steps is negligible. Then we can use the treatment of one-carrier process associated with holes. The hole current rate equation can be expressed by

$$dI_p(x) = \beta I_p dx. \tag{2.139}$$

We rewrite this as

$$\frac{dI_p}{I_p} = \beta dx \tag{2.140}$$

Th solution of this equation is simply given by

$$I_p(x) = I_p(0)\ \exp(\int_0^L \beta dx') \tag{2.141}$$

To find the multiplication factor for one-stage, we divide the output current at location L by the input current, and we have

$$M_p = \frac{I(L)}{I(0)} = \exp[\int_0^L \beta dx'] = e^{\bar{\beta}L} \tag{2.142}$$

where $\bar{\beta}$ is given by Eq. (2.138). Since an one-carrier process is involved, we obtain for the expression of the multiplication factor for one-stage in terms of the hole-impact ionization rate per stage using Eq. (2.101)

$$M_p = 1 + \mu \tag{2.143}$$

From Eqs. (2.142) and (2.143) we obtain the result as

$$\mu = \exp[\int_0^L \beta dx]\ -1 \tag{2.137a}$$

If we expand the exponential terms in series form,

$$M_p = e^{\bar{\beta}L} = 1 + \bar{\beta}L + \frac{(\bar{\beta}L)^2}{2!} + \cdot\ \cdot\ \cdot \tag{2.144}$$

For $\bar{\beta}L << 1$, we have

$$M_p = 1 + \bar{\beta}L. \tag{2.145}$$

From Eqs. (2.143) and (2.145) we also obtain the approximate result

$$\mu = \bar{\beta}L \tag{2.137b}$$

If we neglect hole-impact ionization, then this situation becomes a one-carrier process. Therefore, Eq. (2.101) gives the gain of SAPD as

$$M = (1 + \lambda)^N$$

Using Eq. (2.136), this reduces to

$$M = (2 - \partial)^N \tag{2.146}$$

which is the same result obtained in the previous section.

For the excess noise factor F we find, using Eqs. (2.101) and (2.102),

$$\begin{aligned} F &= 1 + \frac{\text{var } X}{M^2} \\ &= 1 + \frac{1 - \lambda}{1 + \lambda}\frac{M}{M^2}(M - 1) \end{aligned} \tag{2.147}$$

Substituting of Eq. (2.136) and Eq. (2.146) into (2.147) yields

$$F = 1 + \frac{\partial}{2 - \partial}\,[1 - (2 - \partial)^{-N}]$$

which is the same result derived by Capasso in the previous section. This derivation was published by Teich et al. [31].

2.3. DEVICE OPERATION

2.3.1. Design Considerations

2.3.1.1 Gain (Multiplication)

Assume that an electron current $i_e(0)$ is injected into a depletion layer of width w at the plane x = 0. We will assume that the field strength is high enough to produce an avalanche and that there is negligible thermal or photo-generation of carriers in this region. At any point x such that $0 < x < w$, the rate of generation of carriers is given by

$$\frac{di_e(x)}{dx} = \alpha i_e(x) + \beta i_h(x) \qquad (2.148)$$

Also at any point

$$i_e(x) + i_h(x) = I = \text{constant} \qquad (2.149)$$

Eqs. (2.148) and (2.149) give

$$\frac{di_e(x)}{dx} - (\alpha-\beta) i_e(x) = \beta I \qquad (2.150)$$

Eq. (2.150) is of a standard form which integrates to give

$$i_e(x) = \frac{i_e(0) + \int_0^x \beta I \exp[-\int_0^x (\alpha-\beta)\,dx']\,dx}{\exp[-\int_0^x (\alpha-\beta)\,dx']} \qquad (2.151)$$

Now we define the multiplication factor for the injected electrons as

$$M_n = \frac{I}{i_e(0)} = \frac{i_e(w)}{i_e(0)} = \frac{i_e(0) + \int_0^w \beta I \exp[-\int_0^x (\alpha-\beta)\,dx']\,dx}{\exp[-\int_0^w (\alpha-\beta)\,dx']}$$

(2.152)

By rearranging, we get

$$M_n = \frac{1}{1 - \int_0^w \alpha \exp[-\int_0^x (\alpha-\beta)\,dx']\,dx} \tag{2.153}$$

In a similar way, we determine the multiplication factor or gain for injected holes as

$$M_p = \frac{\exp[-\int_0^w (\alpha-\beta)\,dx]}{1 - \int_0^w \alpha \exp[-\int_0^x (\alpha-\beta)\,dx']\,dx} \tag{2.154}$$

Eqs. (2.153) and (2.154) will be used to determine the ionization coefficients α and β as explained in the following sections.

2.3.1.2. Noise Equivalent Power and Detectivity

Consider a detector receiving modulated radiation. Let a radiant power P produce a reading R of the instrument. Then we define the technical sensitivity by [21],

$$C = \frac{R}{P}$$

If a detector produces a voltage V, then

$$C = C_V = \frac{V}{P} \tag{2.155}$$

where the unit of C is volt/watt. If a detector produces current I, then

$$C = C_I = \frac{I}{P} \tag{2.156}$$

To define the noise equivalent power (NEP), we assume that the noise of the detector plus indicating instrument has a spectral intensity $S_R(f)$. Then, the NEP P_{eq} is defined by

$$P_{eq} = \frac{[S_R(f)]^{1/2}}{C} \tag{2.157}$$

where C is given by Eq. (2.155) or Eq. (2.156). The NEP P_{eq} is expressed in watt/$\sqrt{\text{Hz}}$, and is the power that gives the same reading as the noise per unit bandwidth.

Usually, P_{eq} is proportional to the square root of the detector area A. We can normalize the value of P_{eq} to a unit area by setting

$$P^*_{eq} = \frac{P_{eq}}{A^{1/2}} \tag{2.158}$$

where P^*_{eq} is expressed in watt/$(\text{Hz}^{1/2}\text{cm})$.

The best detector type is the one with the smallest P^*_{eq}. Since one wants to identify a good detector by a large number, we define the detectivity D^* by [21]

$$D^* = \frac{1}{P^*_{eq}} = \frac{A^{1/2}}{P_{eq}} \tag{2.159}$$

which is expressed by $(\text{Hz}^{1/2}\text{cm})$/watt.

2.3.1.3. Bandwidth

The response time of an APD is determined primarily by four effects [32]: a) the avalanche build-up time, b) the drift time of the carriers across the depletion width, c) the diffusion time of the generated minority carriers towards the active region, and d) the RC time constant of the device combined with external load resistance. In the following we will discuss these mechanisms in detail. The diffusion time can be minimized if a reach-through avalanche photodiode (RAPD) structure is employed [33] as shown in Fig. 2.12. In this case the response time of the internal APD device is limited by only three mechanisms:

a) the time for carriers to complete the process of multiplication, t_A;

b) the electron transit time across the drift region (W_d), $t_{d,e} = W_d/v_{se}$, where v_{se} represents the electron saturation velocity;

c) the transit time of the last holes across the avalanche region (W_A) and the drift region,

$$t_{dh} = \frac{W_A + W_d}{v_{sh}}$$

where v_{sh} denotes the hole saturation velocity.

The avalanche build-up time, t_A, is a function of the ratio of the ionization coefficients k and and given by [34]

$$t_A = Mk\,\frac{W_A}{v_{se}} \qquad 0 < k < 1 \qquad (2.160)$$

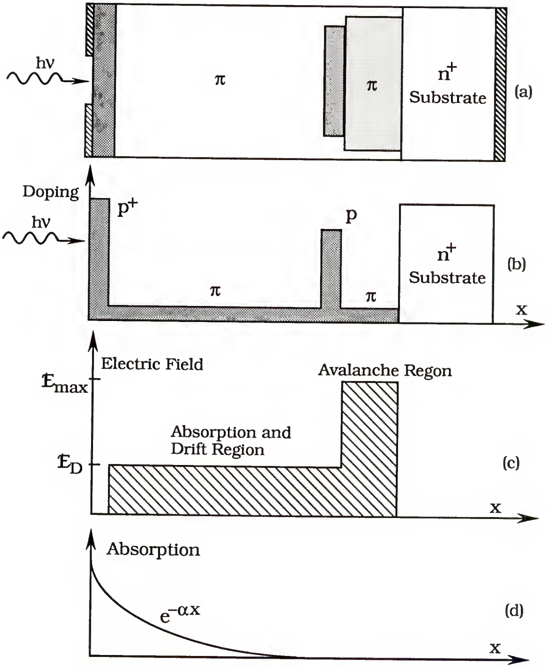

Figure 2.12 Reach-through avalanche photodiode
(a) Device configuration
(b) Doping profile
(c) Field distribution
(d) Absorption of incident light.

The overall response time becomes

$$\tau = \frac{W_d + MkW_A}{v_{se}} + \frac{W_d + W_A}{v_{sh}} \tag{2.161}$$

The bandwidth is characterized by the 3dB cutoff frequency and is approximately given by [34]

$$f_{(-3dB)} = \frac{0.44}{\tau} \tag{2.162}$$

where 0.44 is a numerical factor.

Equations (2.160) and (2.161) show that increasing the multiplication factor results in decreasing the bandwidth. That is, an APD exhibits a limited gain-bandwidth product.

The effect described by Eq. (2.161) gives another reason for seeking materials with k << 1 for devices in which the electrons initiate the avalanche.

2.3.1.4. Quantum Efficiency

The quantum efficiency of the p-i-n structure is defined by the number of electron-hole pairs generated per incident photon [35]:

$$\eta = \frac{I_{ph}/q}{P_{opt}/\hbar\nu} = (1 - r)\ (1 - \frac{e^{-\alpha w}}{1 + \alpha L_p}) \tag{2.163}$$

where

I_p = photogenerated current by the absorption of light.

P_{opt} = incident optical power

ν = light frequency

r = reflection coefficient

α = absorption coefficient

W = depletion-layer width

L_p = minority carrier (hole) diffusion length

Eq. (2.163) shows that one of the key factors that determines the quantum efficiency is the absorption coefficient. Fig. 2.13 shows the measured intrinsic absorption coefficients α for various photodetector materials [36]. Since α is a strong function of the wavelength, the useful wavelength range for detection is limited for a given semiconductor photodiode. The long wavelength cutoff λ_c is established by the energy gap of the semiconductor. For example,

$$\lambda_c = \frac{1.24}{E_g(= 0.67)} \sim 1.8\ \mu\text{m for Ge}$$

$$\lambda_c = \frac{1.24}{1.14} \sim 1.1\ \mu\text{m for Si}$$

$$\lambda_c = \frac{1.24}{1.43} \sim 0.9\ \mu\text{m for GaAs}$$

For wavelengths larger than λ_c, the values of α are too small to give appreciable absorption. The short wavelength cutoff of the photodiodes comes about because the values of α for short wavelengths are very large ($> 10^5 \text{cm}^{-1}$), and

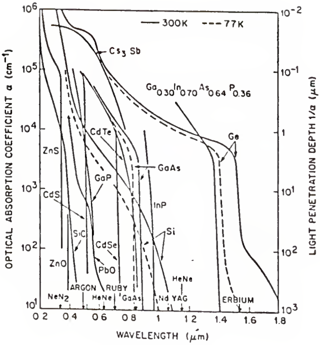

Figure 2.13 Optical absoption coefficients for various photodetector materials. (Ref. 36).

the radiation is absorbed very near the surface where the recombination is fast. Thus the photocarriers recombine before they are collected in the p-n junction.

Another result we can deduce from Eq. (2.163) is that to obtain a high quantum efficiency, the depletion layer must be wide enough to ensure that $\alpha w >> 1$. However, the transit time delay may be considerable. Practically, the depletion width is chosen equal to about $2/\alpha$. At this depth the incident optical power falls to a fraction $1/e^2$ of its value.

The second key factor in the expression for the quantum efficiency is the reflection coefficient r. In most of the materials suitable for photodiodes, the discontinuity in the refractive index going from air ($n = 1$) to the semiconductor ($n \sim 3.5$) leads to a reflection coefficient r of 0.3 at normal incidence. This reflection loss can be eliminated by depositing an appropriate transparent antireflection film coating on the photodiode surface [37]. Silicon nitride, with a refractive index in the range $n = 1.8 \sim 2.0$, can be used for this purpose. The film thickness must be equal to a quarter wavelength of the light in the dielectric.

For practical purposes, instead of the quantum efficiency, the reponsivity R is used and it is defined by

$$R = \frac{I_{ph}}{P_{opt}} = \frac{q\eta}{\hbar\nu} \qquad (2.164)$$

which is the ratio of photocurrent I_{ph} to incident optical power P_{opt}.

2.3.1.5. Dark Current

The reduction of the dark current is important since it limits the minimum detectable power. In an APD the dark current has, in general, three components: a) the generation and recombination current, b) the minority diffusion current, and c) the tunneling current in the avalanche region.

For low temperatures the dark current is governed by generation-recombination currents which are proportional to the depletion width, which in turn depends on the bias voltage. However, in the high temperature range, above room temperature, the dark current is dominated by diffusion currents.

In another classification the dark current can be divided into two components: a) dark current that is multiplied, I_{DM} by the avalanche effect; and b) dark current that is not multiplied, I_{DO}, and which flows through the periphery of the guard ring. In terms of shot noise we get [38]

$$i_n^2 = 2qB\{M^2(I_{ph} + I_{DM})F + I_{DO}\} \qquad (2.165)$$

where B is the bandwidth and I_{ph} is the photosignal current. If M is large, I_{DO} can be neglected and the dark current is governed by I_{DM} and a linear relationship is obtained between the dark current and the multiplication factor (Fig. 2.14). Thus, I_{DM} is determined by extrapolating the linear relationship to unity multiplication.

In the following we will discuss the three components of the dark current in more detail.

a) The Generation and Recombination Current, I_{g-r}

The value of I_{g-r} is proportional to the volume of the depletion region and inversely proportional to the effective carrier lifetime. I_{g-r} is given by [37]

$$I_{g-r} = \frac{qn_iAW}{\tau_e}\left[1 - \exp\left(+\frac{qV}{kT}\right)\right] \qquad (2.166)$$

where n_i is the intrinsic carrier concentration. The magnitude of this current is strongly affected via τ_e by crystal imperfections, impurities, etc., within the depleted region. High quality of defect-free material is required to reduce I_{g-r}[37].

b) The Diffusion Current

The diffusion current I_{dif} arises from thermally generated minority carriers diffusing into the depletion region from the surrounding undepleted p and n regions. The contributions of diffusion current depend on the

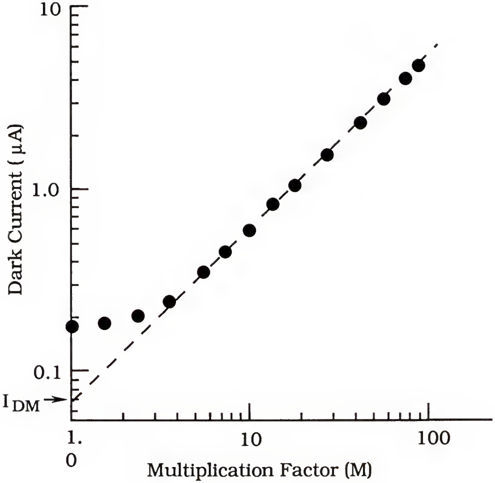

Figure 2.14 A plot of the total dark current versus multiplication factor. Note that separation of I_{DM} is obtained from the graphical method.

details of the photodiode geometry and can be calculated from [37].

$$I_s = qn_i^2 \left(\frac{D_n}{\tau_n}\right)^{1/2} \left(\frac{A_p}{N_A}\right) \quad : \quad \text{p region} \qquad (2.167)$$

$$I_s = qn_i^2 \left(\frac{D_p}{\tau_p}\right)^{1/2} \left(\frac{A_n}{N_D}\right) \quad : \quad \text{n region} \qquad (2.168)$$

where

D_n = n-type minority-carrier diffusion constant

D_p = p-type minority-carrier diffusion constant

τ_n = n-type minority-carrier lifetime

τ_p = p-type minority-carrier lifetime

A_p = area of depletion region bounding the p-region

A_n = area of depletion region bounding the n-region

N_A = acceptor concentration

N_D = donor concentration.

Because the diffusion current contribution to the dark current is proportional to n_i^2 and the I_{g-r} contribution is proportional to n_i, I_{dif} becomes dominant in materials with small bandgaps and at high temperatures.

c) The Tunneling Current At sufficient high fields, tunneling can take place as a band-to-band process or via traps or defect levels in the forbidden energy gap. The expression for band-to-band tunneling in a uniformly doped depletion region may be written as follows [37]

$$I_{tun} \approx \gamma \cdot A \cdot \exp\left[-\frac{\theta m_o^{1/2} E_g^{3/2}}{qhE_m}\right] \qquad (2.169)$$

where m_o is the free electron mass and E_m is the maximum junction field. The parameter $\theta = \alpha(\frac{m_e}{m_o})^{1/2}$, where m_e is the electron effective mass and $\alpha \sim 1$, and depends on the detailed shape of the tunneling barrier. The factor γ is different for tunneling via traps in the bandgap and for band-to-band tunneling. In the latter case,

$$\gamma = (\frac{2m_o}{E_g^{1/2}}) \frac{qE_mV}{4\pi^2h^2} \qquad (2.170)$$

From the exponential term in Eq. (2.169), it can be seen that the tunneling current increases with temperature because of the decrease of E_g with increasing temperature. The tunneling current near breakdown becomes a serious problem, especially for long wavelength APD (where Eg is small). To reduce the parasitic effect of the tunneling current near breakdown voltage, an InGaAs/InP heterojunction structure has been proposed [33,40] as we will explain in the next section.

2.3.1.6. Avalanche Photodiode Structure

In optical fiber communication, a detector is required to have (i) a low-noise performance, (ii) a low-operation voltage, (iii) a stable gain, and (iv) high-speed performance. The reach-through structure is designed to meet all these requirements [33].

The reach-through avalanche photodiode (RAPD) structure shown in Fig. 2.12 has the following advantages.

1) The absorption in the p^+ region is small and the slow diffusion of carriers to the high-field region is minimized.

2) The main absorption occurs in the high-field thick n-region where a high quantum efficiency and a small transit time can be achieved.

3) The p-n^+ junction is guarded by the surrounding n region so that uniform avalanche gain can be achieved in a uniform junction without edge breakdown.

4) The doping of the p-n^+ junction where avalanche multiplication occurs can be optimized to obtain the lowest possible noise and to obtain a slowly varying multiplication factor with bias voltage.

In III-V compound materials (direct bandgap semiconductors), a "soft" breakdown of the dark current due to tunneling is typical [41]. To solve this problem Nishida [42] made use of the heterostructure shown in Fig. 2.15. In this structure the GaInAs layer forms a narrow bandgap region designed to absorb the incident photons. The InP layer is a separate wide bandgap region, included to support avalanche multiplication. Any APD structure having these separate regions has become known as a separate absorption and multiplication APD (SAM-APD).

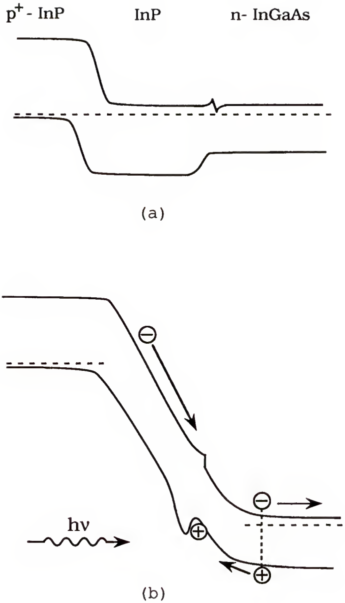

Figure 2.15 Energy band diagrams of an InGaAs-InP photodiode with separate absorption and multiplication regions (Ref. 32)
(a) zero bias
(b) reverse bias.

The narrow bandgap region must be sufficiently thick to absorb all the incident photons in order to yield a high quantum efficiency and must have a sufficiently low doping concentration for it to be fully depleted with a modest applied field. The thickness and doping level of the wide gap material are adjusted so that the electric field in the narrow bandgap material never exceeds the value which causes significant tunneling current.

The drawback of this structure is that this APD has a poor time response due to a pile-up of holes at the discontinuity in the valence band at the InGaAs/InP interface. Capasso [43] overcame this drawback by using superlattice layers at the interface grading out the discontinuity.

2.3.2. Parameter Measurements

The first measurements in which the ionization coefficients α and β were separately determined from photomultiplication measurements on a P^+N junction were reported by Wul and Shotov [44]. Their analysis assumed a constant value of the ratio $k = \beta/\alpha$.

Lee et al. [45] showed that if the measurements of the electron and hole multiplication, M_n and M_p, are made in the same junction, then determination of α and β is possible from the relationship

$$\int_0^W (\alpha-\beta)\,dx = \ln\left(\frac{M_n}{M_p}\right) \qquad (2.171)$$

To determine accurately M_n and M_p, several experimental conditions must be met [46]:

1) Pure electron and pure hole injection must be obtained in the same junction. This is best achieved by using photoexcitation.

2) The photocurrent without avalanche gain must be measured precisely.

3) The electric field variation in the junction should be sufficiently gradual so that α and β can be assumed to be only functions of electric field.

4) The electric field profile must be accurately known.

5) The avalanche gain must be uniform across the active area of the device.

There are several device structures that allow for the accurate determination of α and β. Here we introduce the p-i-n diode structure which is the simplest and satisfies all of the requirements just listed.

Fig. 2.16 shows the p-i-n diode configuration and its electric field distribution. Pure electron and hole injection can be obtained because the incoming light is completely absorbed in the p^+ or n^+ region. Since the electric field is constant in this structure ($E = V/W$,

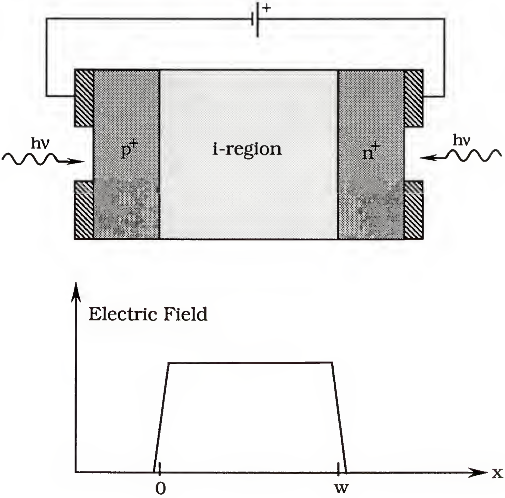

Figure 2.16 A p-i-n photodiode and its electric field profile.

where V is the total voltage across the intrinsic region), the ionization coefficients are constant and given by

$$\alpha = \frac{1}{W} \left[\frac{M_n - 1}{M_n - M_p} \right] \ln(\frac{M_n}{M_p}) \qquad (2.172)$$

$$\beta = \frac{1}{W} \left[\frac{M_p - 1}{M_p - M_n} \right] \ln(\frac{M_p}{M_n}) \qquad (2.173)$$

In the following we will derive equations (2.172) and (2.173).

From Eqs. (2.153) and (2.154) we find

$$\frac{M_n}{M_p} = \frac{\exp[\int_0^w (\alpha-\beta)dx]}{1 - \int_0^w \beta \exp[\int_x^w (\alpha-\beta)dx']dx} \times \{1 - \int_0^w \beta \exp[\int_x^w (\alpha-\beta)dx']dx\}$$

$$= \exp[\int_0^w (\alpha-\beta)dx]. \qquad (2.174)$$

Therefore,

$$\phi(w) = \int_0^w (\alpha-\beta)dx] = \ln(\frac{M_n}{M_p}) \qquad (2.175)$$

which is the same as Eq. (2.171). Eq. (2.174) can be rewritten as

$$\alpha - \beta = \frac{1}{W} \ln(\frac{M_n}{M_p}) \qquad (2.176)$$

From Eq. (2.154)

$$M_p - 1 = \frac{\exp[-\int_0^w (\alpha-\beta)dx] - 1 + \int_0^w \alpha \exp[-\int_0^x (\alpha-\beta)dx']dx}{1 - \int_0^w \alpha \exp[-\int_0^x (\alpha-\beta)dx']dx}. \tag{2.177}$$

By subtracting Eq. (2.153) from Eq. (2.154), we have

$$M_p - M_n = \frac{\exp[-\int_0^w (\alpha-\beta)dx] - 1}{1 - \int_0^w \alpha \exp[-\int_0^x (\alpha-\beta)dx']dx}. \tag{2.178}$$

The denominators of Eqs. (2.177) and (2.178) are the same. Thus

$$\begin{aligned}\frac{M_p - 1}{M_p - M_n} &= \frac{\exp[-\int_0^w (\alpha-\beta)dx] - 1 + \int_0^w \alpha \exp[-\int_0^x (\alpha-\beta)dx']dx}{\exp[-\int_0^w (\alpha-\beta)dx] - 1} \\ &= 1 + \frac{\int_0^w \alpha \exp[-\int_0^x (\alpha-\beta)dx]}{-\int_0^w (\alpha-\beta)\exp[-\int_0^x (\alpha-\beta)dx']dx} \\ &= 1 - \frac{\alpha}{(\alpha-\beta)} \\ &= -\frac{\beta}{\beta-\alpha}\,.\end{aligned} \tag{2.179}$$

By rearranging Eq. (2.179) in terms of β, we obtain

$$\beta = (\beta - \alpha)\frac{M_p - 1}{M_p - M_n} \; . \tag{2.180}$$

Substitution of Eq. (2.176) yields

$$\beta = \frac{1}{W} \left[\frac{M_p - 1}{M_p - M_n} \right] \ln\left(\frac{M_p}{M_n}\right). \tag{2.181}$$

In a similar way, we have the expression for α as

$$\alpha = \frac{1}{W} \left[\frac{M_n - 1}{M_n - M_p} \right] \ln\left(\frac{M_n}{M_p}\right) \qquad \text{Q.E.D.}$$

Fig. 2.17(a) shows two practical device structures that allow for very pure optical injection of electrons and holes. These have become the standard device configurations for ionization coefficient measurements [37].

In the first structure note that a window is etched in the substrate to within a few tens of micrometers from the junction in order to obtain pure electron injection using strongly absorbed light. However, in materials with a short minority-carrier diffusion length, many of the electrons optically excited in the region of the substrate just above the etched window recombine before being collected by the junction. The near-bandgap radiation generated by this recombination can be reabsorbed by the Franz-Keldysh effect in the space-charge region. This reabsorption produces a contamination of the electron-injected current, and if the width of the avalanche region is appreciable, pure electron injection is impossible. This effect was first observed by Bulman et al. [47].

Capasso [48] introduced a modification of the basic structure (Fig. 2.17(b)) to eliminate this source of contamination. A thin (< 1 μm) buffer layer (p^+-InGaAsP), composition lattice matched to the substrate, is inserted between the n-layer and the substrate.

The window is etched with a selective etchant that stops at the buffer layer. This thin layer with a smaller bandgap completely absorbs the incident light; yet the thickness is substantially smaller than the minority carrier diffusion length, so that the amount of recombination is negligible.

Fig. 2.18 shows an experimental set-up for the measurements of the ionization rates [37]. The photocurrent is measured via phase-sensitive detection. An optical fiber is used to couple the light source to the photodiode. This minimizes any contamination of the electron photocurrent from stray light incident on the edge of the mesa.

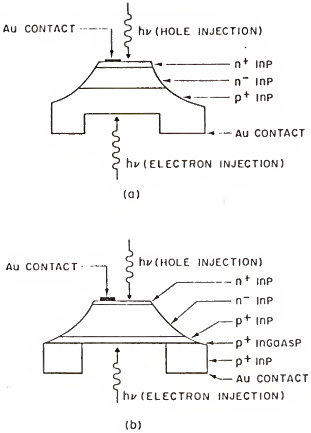

Figure 2.17 Configuration of practical device structures (Ref. 6)
(a) a simple structure used for the parameter measurements.
(b) an improved structure for pure electron or hole inection.

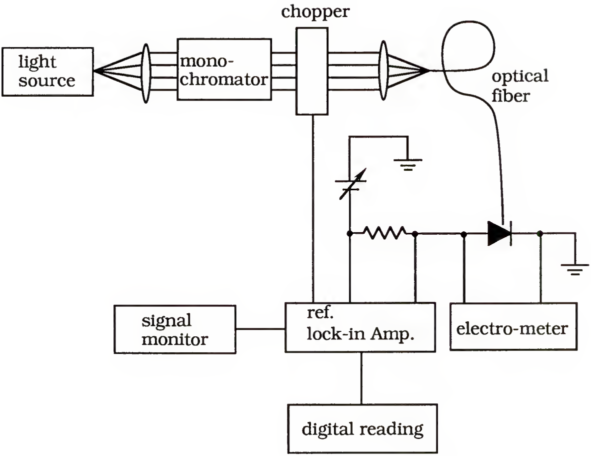

Figure 2.18 Typical experimental set-up used in photomultiplication measurements (Ref. 6).

CHAPTER III

TWO SIMPLE PROOFS OF CAPASSO'S EXECESS NOISE FACTOT F_N OF AN IDEAL N-STAGE STAIRCASE MULTIPLIER

We begin with a simple proof of Capasso's excess noise factor [49] of an ideal N-stage staircase multiplier by applying the variance theorem [50] to an ideal one-stage-staircase multiplier. The applicability of the variance theorem to a branching process is not immediately obvious since correlations between the various generations occur. Yet the overall result indicates the validity of the variance theorem as was shown explicitly by Van Vliet [51]. "Ideal" means that only the electrons contribute to the device operation. The noise process of such a one-stage amplifier can be described in the following way. We write

$$m_1 = \sum_{k=1}^{n_1} X_k \tag{3.1}$$

where m_1 and n_1 are the fluctuating output and input particle numbers, respectively, and X_k is a stochastic event, in this case the impact ionization process at the staircase interface. Then, $X_k = 1$ (no impact ionization) with probability $(1 - \lambda)$ and $X_k = 2$ with probability λ. Consequently

$$\overline{X}_k = \overline{X} = \overline{M}_1 = 1 + \lambda \tag{3.2a}$$

and

$$\mathrm{var}\ X_k = \mathrm{var}\ X = (1 - \lambda)\cdot\lambda \tag{3.2b}$$

In Eq. (3.2a), $\overline{M}_1$ is the average gain of a single ideal stage. By applying the variance theorem to (3.1), we obtain

$$\mathrm{var}\ m_1 = \overline{X}^2\ \mathrm{var}\ n_1 + \overline{n}_1\ \mathrm{var}\ X \tag{3.3a}$$

Since we assume a Poissonian distribution for n_1, Eq.(3.3a) reduces to

$$\mathrm{var}\ m_1 = \overline{n}_1\{\overline{X}^2 + \mathrm{va}\ X\} \tag{3.3b}$$

The excess noise factor F_1 of a one-stage multiplier is defined by

$$F_1 = \frac{\text{noise in output particle number}}{\text{amplified input noise if } X_k \text{ did not fluctuate}}$$

$$= \frac{\mathrm{var}\ m_1}{\overline{X}\ \mathrm{var}\ n_1} \tag{3.4a}$$

Upon substituting Eqs. (3.2a) and (3.3b) into Eq. (3.4a), we find for F_1

$$F_1 = \frac{\overline{X}^2 + \mathrm{var}\ X}{\overline{X}^2} = 1 + \frac{\mathrm{var}\ X}{\overline{X}^2} = 1 + \frac{\lambda(1-\lambda)}{(1+\lambda)^2} \tag{3.4b}$$

If $\mathfrak{M}_n$ is the noise measure of the multiplier [52], defined as

$$\mathfrak{M}_n = \frac{F_1 - 1}{1 - 1/\bar{M}_1} = \frac{(1 - \lambda)}{(1 + \lambda)} \tag{3.5}$$

then the excess noise factor F_∞ of an infinite number of identical stages in cascade is ($\mathfrak{M}_n$ + 1). If the infinite number of stages is divided into groups of N subsequent stages, each with an excess noise factor F_N and a gain $\bar{M}_N = (1 + \lambda)^N$, then Eq. (3.5) may also be written as

$$\mathfrak{M}_n = \frac{(1 - \lambda)}{(1 + \lambda)} = \frac{F_N - 1}{1 - 1/\bar{M}_N} \tag{3.6}$$

Consequently

$$F_N = 1 + \left(\frac{1 - \lambda}{1 + \lambda}\right) [1 - (1 + \lambda)^{-N}] \tag{3.7}$$

which is Capasso's result [49].

The second, even simpler proof uses Friiss's formula [53] for the excess noise factor F_n of N identical single stages, each of excess noise factor F_1 and gain $\bar{M}_1$. According to Friiss

$$\begin{aligned} F_N &= 1 + (F_1 - 1) + \frac{F_1 - 1}{\bar{M}_N} + \cdots + \frac{F_1 - 1}{(\bar{M}_N)^{N-1}} \\ &= 1 + \frac{F_1 - 1}{1 - (\bar{M}_N)^{-1}} [1 - (\bar{M}_N)^{-N}] \end{aligned} \tag{3.8}$$

Substituting for F_1 and $\bar{M}_1$ yields again Eq.(3.7).

The introduction of the noise measure $\mathfrak{M}_n$ or the application of Friiss's formula Eq. (3.8) puts the calculations of individual situations on a general schematic basis that is easy to apply to this and to other systems; for example, Eq. (3.8) applies also to secondary emission multipliers and it connects signal amplifier theory with particle multiplier theory.

Eq. (3.7) agrees with the results presented in Van Vliet's single-carrier multiplication paper [51]. However, in this paper no use is made of the variance theorem, but rather the branching problem is solved by an iteration process that involves the consideration of correlation between the branches of offspring. Teich and Matsuo [54] have shown that Van Vliet's method and Capasso's method lead to the same results. When the holes also contribute, Van Vliet's two carrier multiplication process [27] must be applied.

CHAPTER IV
NONPARABOLICITY AS A TOOL IN BAND-GAP ENGINEERING

4.1. Introduction

The study of impact ionization thresholds in semiconductors was shown to be equivalent to the study of the "most probable' Auger transitions in the same system some time ago [55], and the latter study goes back even further [56]. Many papers on threshold calculations have been published since that time. With increasing interest in low-noise avalanche photodiodes and impact ionization across energy-band discontinuities in heterostructures using III-V semiconductor compounds and related materials, it is of interest to reexamine what is known about threshold calculations with special reference to band nonparabolicity. For processes involving up to three parabolic bands standard formulas are of course available [57]. We note early calculations of thresholds for nonparabolic bands both analytically [57] and numerically [58,59]. Graphical constructions have also been used [60-62]. For later work, recent reviews [62,6] may be consulted.

4.2. Derivation of a Formula for the Impact-IonizationThreshold Energy with Nonparabolic Conduction and One or Two Parabolic Valence Band

As we found in chapter II, momentum conservation principle yields

$$k_i = k_1(2 + \frac{m_h}{m_e}) \qquad (2.19)$$

where k_i and k_1 represent wave vectors of initiating particle and offspring particle 1, respectively. If we use the definition of $\mu \equiv \frac{m_h}{m_e}$, this equation reduces to

$$k_i = \frac{1 + 2\mu}{\mu} k_1 \qquad (4.1)$$

We assume that an initiating electron is located in the conduction band of the simple Kane type. Then

$$\frac{\hbar^2 k_i^2}{2m_e} = E(1 + \alpha' E) \qquad (4.2)$$

where m_e is the effective mass at the conduction-band minimum and α' is a nonparabolicity parameter for a simple Kane band. For the threshold condition Eq. (4.2) can be rewritten as

$$\frac{\hbar^2 k_i^2}{2m_e} = E_T(1 + \alpha' E_T) \qquad (4.3)$$

Since this is a simple quadratic equation, we solve for E_T and obtain

$$E_T = -\frac{1}{2\alpha} + \frac{1}{2\alpha}\sqrt{1 + 4\alpha' A} \qquad (4.4)$$

where

$$A \equiv \frac{\hbar^2 k_i^2}{2m_e} \qquad (4.5)$$

Alternatively, threshold energy can be obtained by energy conservation principle, which is

$$E_T = \frac{\hbar^2 k_1^2}{2m_e} + \frac{\hbar^2 k_2^2}{2m_e} - (-\frac{\hbar^2 k_3^2}{2m_h}) + E_G \qquad (4.6)$$

where we assumed that two conduction-band states (k_1 and k_2) and one valence-band state (k_3) are treated as parabolic. This is possible as they are states of low energy. It is this physical approximation which makes our problem tractable by analytical methods. This is not possible if one treats all three conduction-band states as nonparabolic [63].

Upon substituting Eq. (4.1) into (4.6), we obtain

$$\begin{aligned} E_T &= \frac{\hbar^2 k_i^2}{2m_e}\left[\frac{2\mu}{(1+2\mu)^2} + \frac{\mu}{(1+2\mu)^2}\right] + E_G \\ &= \frac{\hbar^2 k_i^2}{2m_e}\left[\frac{\mu}{1+2\mu}\right] + E_G \\ &= \frac{A\mu}{1+2\mu} + E_G \qquad (4.7) \end{aligned}$$

By equating Eq. (4.4) and (4.7) with some rearrangements, we have

$$A^2\left(\frac{2\alpha'\mu}{1+2\mu}\right)^2 + A\left[8\alpha'^2E_G\frac{\mu}{1+2\mu} - \frac{1+\mu}{1-2\mu}4\alpha'\right] + 4\alpha'^2E_G^2 + 4\alpha'E_G = 0 \quad (4.8)$$

If we use substitutions such as

$$\frac{\mu}{1+2\mu} \equiv \phi, \qquad \frac{1+\mu}{1-2\mu} \equiv \theta,$$

then, Eq. (4.8) reduces to

$$A^2(4\alpha'^2\phi^2) + A[8\alpha'^2E_G\phi - 4\alpha'\theta] + (4\alpha'^2E_G^2 + 4\alpha'E_G) = 0 \quad (4.9)$$

which is a quadratic equation form for A. If we solve this equation for A, we obtain

$$A = \frac{\theta}{\phi^2}\left[\frac{1}{2\alpha'} \pm \frac{1}{2\alpha'}\sqrt{1-4\alpha'E_G\frac{\mu(1+2\mu)}{(1+\mu)^2}}\ \right] - \frac{\alpha'E_G}{\phi} \quad (4.10)$$

Finally, we substitute Eq. (4.10) into (4.7). Then, we have

$$E_T = \frac{1+\mu}{2\mu\alpha'}\left[1 \pm \sqrt{1 - \frac{4\mu(1+\mu)}{(1+\mu)^2}\alpha'E_G}\ \right] \quad (4.11)$$

where it turns out that only the bottom sign in the bracket has physical meaning.

Ridley's formula (4.6) can be easily derived if we use the condition such that

$$\frac{\mu(1 + 2\mu)}{(1 + \mu)^2}\alpha' E_G \ll 1. \tag{4.12}$$

This condition yields an approximation of the square root term between the brackets of Eq. (4.11). That is,

$$\sqrt{1 - \frac{4\mu(1+\mu)}{(1+\mu)^2}\alpha' E_G} \approx 1 - 2\alpha' E_G \frac{\mu(1 + 2\mu)}{(1 + \mu)^2} \tag{4.13}$$

Using this first order approximation, Ridley's formula is obtained as

$$E_T = \frac{1+2\mu}{1+\mu}\left[1 + \frac{\mu 1+\mu}{(1+\mu)^2}\alpha' E_G\right] E_G \tag{4.14}$$

If one is concerned with GaAs and uses $\mu \sim 0.067/0.45 = 0.149$, $\alpha E_G \sim 1$, $E_G \sim 1.424$ eV, this formula gives $E_T \sim 1.84$ eV, which is a distinctive improvement on the value [56,57]

$$E_T = \frac{1 + 2\mu}{1 + \mu} E_G \sim 1.61 \text{ eV} \tag{4.15}$$

which one would find for parabolic bands, if one notes that the accepted value lies near 2 eV [6]. Using the values for GaAs, our new formula Eq. (4.11) yields the result $E_T = 1.95$ eV, in excellent agreement with the accepted value.

Note that Eqs. (4.11) and (4.14) share as common characteristic that they reduce to Eq. (4.15) in the limit $\alpha E_G \to 0$, as is of course required.

4.3. Further Discussions Concerning the Nonparabolicity

Formula (4.11) is compared with (4.14) in Fig. 4.1, showing that the new formula yields higher threshold energies. There is a cutoff when the square-root becomes imaginary and formula (4.11) suggests that impact ionization ceases. However, for these higher E_T values the approximation just discussed begins to fail as the two low-energy states 1 and 2 (Fig. 4.2(b)) move higher into the conduction band and begin to feel the nonparabolicity. Thus the cutoff value $\mu = \mu_c$ suggested by Eq. (4.5) which occurs when

$$\alpha' E_G = \frac{(1 + \mu)^2}{4\mu(1 + 2\mu)} \qquad (4.16)$$

or

$$\mu_c = \frac{\sqrt{(\alpha' E_G)^2 + \alpha' E_G} - (\alpha' E_G - \frac{1}{2})}{4\alpha' E_G} - \frac{1}{2} \quad (\alpha' E_G > \frac{1}{8}) \qquad (4.17)$$

can be misleading. To establish a more reliable expression, we look for the condition that the line on the E-k diagram representing the downward transition in the conduction band cannot intersect the valence band. This means that the valence-band asymptotes must be steeper that the conduction-band asymptotes (Fig. 4.2). The condition for this turns out to be simply

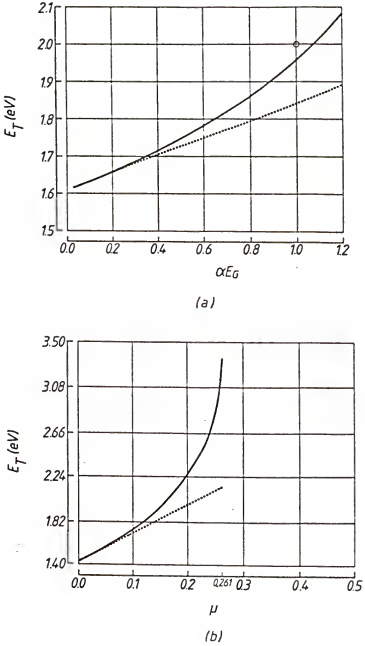

Figure 4.1 Threshold energy as a function of (a) αE_g (using $\mu = 0.149$) and (b) μ (using $\alpha E_g = 1.0$) for GaAs. The present result is represented by a solid line, dashed line represents Ridly's result, and the experimental value is shown as a circle.

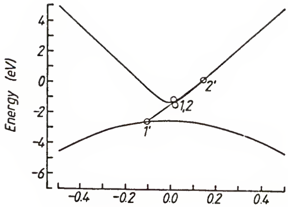

(a) $\mu = 0.2\,\mu_c$

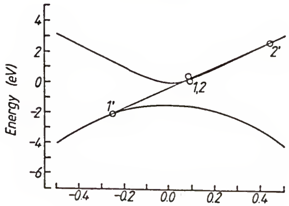

(b) $\mu = \mu_c$

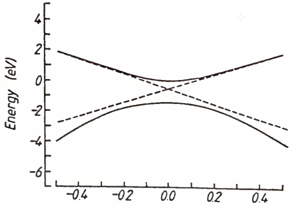

(c) $\mu = 1.2\,\mu^*$

Figure 4.2 Quadruplets of states at the trheshold of impact ionization at given aEg = 1. The effect of increasing m is shown. The horizontal axis gives ak/p where a =5.65Å. (a) $\upsilon = 0.2\ \mu_c$, (b) $\mu = \mu_c$, (c) $\mu = 1.2\ \mu^*$.

$$\mu < \mu^* \equiv [4(\alpha' E_G - \frac{1}{2})]^{-1} \qquad (4.18)$$

Thus for $\alpha' E_G \sim 1$, impact ionization is still possible in the range (see Fig. 4.3)

$$\mu_c < \mu < \mu^*, \quad \text{i.e., } 0.26 < \mu < 0.5$$

It ceases for $\mu > \mu^*$, provided the Kane band model still holds.

Thus the new formulas (4.11) and (4.18) show that one has a way of "switching off" this particular impact ionization process, given only a band of the form Eq. (4.2). In a band-gap engineering context if one needs strong impact ionization one is looking for small μ value- this is already suggested by the older formula (4.15). One can on the other hand decrease it, or indeed switch it off altogether, by looking for large enough values of μ. This latter feature is not even hinted at by the earlier formulae (4.14) or (4.15). In view of the occurrence of more complicated band structures (see for example Ref. 12), the problem of identifying other structures also displaying switch off is of interest and is under consideration.

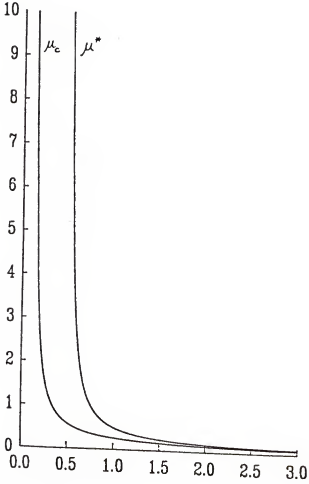

Figure 4.3 Electron/hole effective mass ratios μ_c and μ^* as a function of αE_g.

Chapter V
THE THEORY OF TRAPPING AND DETRAPPING OF ELECTRONS IN MULTIQUANTUM-WELL (MQW) HETEROSTRUCTURES

5.1. Introduction

It is well known that noise is associated with the randomness of the charge transport mechanism. If there is a fluctuation inside an electronic device, the electric signal at the external terminal will fluctuate as a result. One of the fluctuation mechanisms, the carrier generation and recombination (g-r) process, is quite a common source of carrier density fluctuations in semiconductor devices. This g-r process takes place via trap energy levels located in the forbidden band-gap.

The noise associated with the random filling and emptying of the traps is called trapping noise and has been studied for many decades. Gisolf [65] used a Fourier Transform method to find the power spectrum of a current pulse resulting from carrier detrapping and whose duration is determined by the time between the release of a carrier from a trap and the subsequent capture by a trap. He assumed each event to be independent and a fixed carrier lifetime. The latter assumption is not quite right because the carrier lifetime in reality is distributed. Therefore, Bernamont [66] and van der Ziel [67] took into account a probability function for the lifetime of free electrons, assumed it to be Poissonian, and came up with a Lorentzian type spectrum. These researchers considered only the lifetime of the free carriers. Machlup [68] however, took also into account the mean time carriers are bound in traps. Thus he compared the trapping and detrapping with a random telegraph signal which switches between two states randomly. If the mean free time is relatively small compared to the mean bound time, his result approaches Bernamont's result.

More general approaches have been developed later by Van Vliet et al. [69,70]. They were interested in how to incorporate all the information concerning the microscopic and macroscopic electron-trap behavior into the basic equations which govern device operation. This so-called collective approach consists basically of two parts. First, the internal sources of the fluctuations due to g-r processes and diffusion are accounted for. Secondly, the response function which relates the external terminal noise to the internal distributed sources should be calculated. These two parts are already linked together in the Fourier Transformed transport equations. An elegant formalism was presented by Van Vliet et. al and named the Transfer Impedance (T.I.) method. In general, an analytic solution of the differential transport equations is possible, though in many cases it becomes very complicated. We follow the collective T.I. approach to solve our problem.

G-r noise spectra obtained by solving the transport equations can be characterized by basically two parameters, namely by the low-frequency plateau values of the spectra and by the cutoff frequencies of the Lorentzians. Both of the parameters depend on the activation energy, density and capture coefficient of the traps.

From our noise measurements, we observed substantial sub-shot noise in the high-frequency regime of some devices, indicating that carrier flow in the MQW structures is severely modified by the trapping and detrapping in the quantum-wells.

To understand the sub-shot noise associated with the trapping, we look at the carrier flow in the presence of traps. Under reverse bias condition, carrier motion is limited by the transit time across the depletion region. If traps are present, carrier arrival is delayed because carriers spend some time in the traps until they are released to resume their flight. Since current is charge flow per unit time, trapping results in a current decrease by a factor equal to a time constant ratio, i.e. the ratio of lifetime over the transit time. Let us say the ratio is N. This phenomenon results in a decrease of the spectrum by a factor N^2. When we express the spectrum in terms of equivalent noise current, an 1/N-dependence results.

Can we explain the measured noise spectrum based on this theory? If we look at the noise spectrum between 100 Hz and 200 MHz, we observe 1/f noise like behavior with several small bumps. Since the trapping/detrapping process associated with the quantum-wells is quite fast due to the large capture cross-sections, cutoff-frequencies lie in the very high frequency domain. How do we relate to this low-frequency Lorentzian spectrum then? We assume that slow trapping/detrapping processes exist via the traps located in the heterostructure interfaces. To have a 1/f noise like spectrum extending up to 100 MHz, we assume with Tehrani [71] that the spectrum is composed of multiple Lorentzians with parameters that are separated more than one decade from each other.

Thus we have basically two kinds of traps, quantum-wells acting as giant traps and interface traps. The latter is the conventional trap which is caused by an imperfect lattice match or by an interface defect in the heterostructure junction.

5.2. Trapping and Detrapping in Multiquantum-wells

Fig. 5.1(a) shows the bandprofile of the MQW structures where carrier trapping and detrapping occurs. The thickness of the quantum-well and -barrier are l_2 and l_1, respectively. To describe the dynamics of the hole and

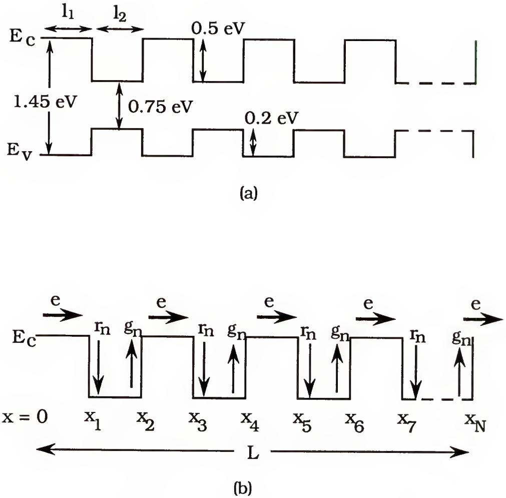

Figure 5.1 (a) A band diagram of the multiquantum-well heterostructure layers
(b) A simplified band diagram to model the trapping and detrapping in quantum wells.

electron transitions in this system, a four energy-level system is needed. Finding an analytic solution for this system however, results in many difficulties due to the ambipolar nature of the system when we take into account both holes and electrons. To circumvent this situation, an approximation is made, that is, when electron injection is dominant as is the case in the devices under investigation, we neglect the hole density. Consequently, a simplified system consisting of two energy levels, i.e., the extended state and the localized state of the conduction band shown in Fig. 5.1(b), can be used.

The basic equations which describe the carrier transitions and flow are the kinetic equations, Poisson's equation and the current equation. For a two energy level system, the kinetic equations read

$$\frac{dn}{dt} = g_n - r_n + \frac{1}{q}\frac{dJ_n}{dx} + \gamma \qquad (5.1)$$

$$\frac{d\hat{n}}{dt} = -g_n + r_n - \gamma \qquad (5.2)$$

In the above equations, n and $\hat{n}$ are the electron density in the extended conduction band and the electron density in the localized conduction band, respectively. The Langevin term, γ represents the fluctuations in the transition rates between the extended conduction band and the localized conduction band. The current equation for the electrons, neglecting diffusion, is

$$J_n = q\mu_n nE \tag{5.3}$$

If we include the displacement current, the total device current J becomes equal to

$$J = J_n + \varepsilon\frac{\partial E}{\partial t} \tag{5.4}$$

where we neglect the hole current as we mentioned earlier.

To simplify the problem, we assume a quantum-well to behave as a giant acceptor-type trap. Thus, the quantum-well is neutral when it is empty, whereas it is negatively charged when it is filled. In this system, the one-dimensional Poisson equation is expressed as

$$\frac{dE}{dx} = -\frac{q}{\varepsilon}(n + \hat{n}) \tag{5.5}$$

where E represents the electric field. The density $\hat{n}$ is equal to fN_A, and f is a trap filling factor. density of the acceptor-like traps. The concept of trap density in this context will be discussed in section 4 of this chapter.

For the generation and recombination terms we have

$$g_n = e_n\hat{n} = C_n n_1\hat{n} \tag{5.6}$$

$$r_n = C_n n(N_A - \hat{n}) \tag{5.7}$$

where C_n is a capture coefficient, n_1 is the Shockley parameter, equal to the density of electrons in the conduction band, when the Fermi level coincides with the trap level.

Since the total current is solenoidal Eq. (5.1) is redundant and can be dismissed.

By substituting equations (5.6) and (5.7) into Eq. (5.2) and linearization, we obtain the following A.C. equation for the trapped electron density in the quantum-wells

$$\begin{aligned}\frac{d\Delta\hat{n}}{dt} &= -\Delta(g_n - r_n) - \gamma \\ &= \Delta n(N_A - \hat{n}_o)C_n - \Delta\hat{n}(n_1 + n_o)C_n - \gamma \end{aligned} \tag{5.8}$$

Now we define several time constants

$$\tau_{1n}^{-1} = C_n(N_A - \hat{n}_o) \tag{5.9}$$

$$\tau_{2n}^{-1} = C_n(n_1 + n_o) \tag{5.10}$$

$$\tau_n^{-1} = \tau_{1n}^{-1} + \tau_{2n}^{-1} \tag{5.11}$$

With three definitions, wee rewrite equation (5.8)

$$\frac{d\Delta\hat{n}}{dt} = \frac{\Delta n}{\tau_{1n}} - \frac{\Delta\hat{n}}{\tau_{2n}} - \gamma \tag{5.12}$$

Summarizing, we have three equations describing our system. If we express these equations in a simplified form

$$C_1 = f(J,n,E) \tag{5.4a}$$

$$C_2 = f(n,\hat{n},E) \tag{5.5a}$$

$$C_3 = f(n,\hat{n},\gamma) \tag{5.12a}$$

where C_1, C_2, and C_3 are constants and f denotes a function. We have three equations with five variables. Our goal is to reduce these three equations to one equation which has only three variables, i.e. J, E, and γ. Assuming A.C. short conditions $(\int \tilde{E}dx = 0)$ or A.C. open circuited conditions (J = 0), where $\tilde{E}$ and $\tilde{J}$ denote the A.C. Fourier components of E(t) and J(t), respectively. In this way, we can obtain the current or voltage fluctuations in terms of γ. Now we return to the reduction task.

Fourier transform of Eq. (5.12) yields

$$(i\omega + \frac{1}{\tau_{2n}})\tilde{\hat{n}} = \frac{\tilde{n}}{\tau_{1n}} - \tilde{\gamma} \tag{5.13}$$

Upon substituting Eq. (5.12) into the Fourier transformed Poisson equation, we obtain the following first order differential equation for $\tilde{n}$.

$$\tilde{n} = -\frac{\varepsilon}{q}\,\frac{(1+i\omega\tau_{2n})}{(1+i\omega\tau_n)}\,(\frac{\tau_n}{\tau_{2n}})\,\frac{d\tilde{E}}{dx} + \frac{\tau_n}{(1+i\omega\tau_n)}\,\tilde{\gamma} \tag{5.14}$$

To determine the current fluctuation, we return to the A.C. current equation given by

$$\Delta J = q\mu n_o \Delta E + q\mu E_o \Delta n + \varepsilon \frac{\partial \Delta E}{\partial t} \tag{5.15}$$

A Fourier transform of this equation gives

$$\tilde{J} = (q\mu n_o + i\omega\varepsilon)\tilde{E} + q\mu E_o \tilde{n} \tag{5.16}$$

Using the definition of the dielectric relaxation time

$$\tau_\Omega^{-1} = \frac{q\mu n_o}{\varepsilon} \tag{5.17}$$

we rewrite Eq. (5.16)

$$\frac{\tilde{J}}{\varepsilon} = (i\omega + \frac{1}{\tau_\Omega})\tilde{E} + \frac{q}{\varepsilon} v_n \tag{5.18}$$

where μE_o is replaced by v_n which is the electron drift velocity. By substituting Eq. (5.14) into the above equation, we obtain the following differential equation for $\tilde{E}$.

$$\frac{d\tilde{E}}{dx} - \frac{\tau_{2n}(1+i\omega\tau_n)(1+i\omega\tau_\Omega)}{(1+i\omega\tau_{2n})\tau_n\tau_\Omega v_n}\tilde{E} = -\frac{(1+i\omega\tau_n)\tau_{2n}}{\varepsilon(1+i\omega\tau_{2n})\tau_n v_n}\tilde{J} + \frac{q\tau_{2n}}{\varepsilon(1+i\omega\tau_{2n})}\tilde{\gamma} \tag{5.19}$$

For simplicity, this equation can be written in the following form.

$$\frac{d\tilde{E}}{dx} - P\tilde{E} = Q \tag{5.19a}$$

where

$$P = \frac{\tau_{2n}(1+i\omega\tau_n)(1+i\omega\tau_\Omega)}{(1+i\omega\tau_{2n})\tau_n\tau_\Omega v_n} \tag{5.20}$$

$$Q = -\frac{(1+i\omega\tau_n)\tau_{2n}}{\varepsilon(1+i\omega\tau_{2n})\tau_n v_n}\tilde{J} + \frac{q\tau_{2n}}{\varepsilon(1+i\omega\tau_{2n})}\tilde{\gamma} \tag{5.21}$$

The solution of this differential equation which satisfies the boundary condition $\tilde{E} = 0$ at $x = 0$ is given by

$$\tilde{E}(x) = e^{-\int_0^x P(x'')dx''} \int_0^x Q(x')e^{\int_0^{x'} P(x'')dx''} dx' \tag{5.22}$$

Since the values of $P(x'')$ and $Q(x')$ vary periodically in the multiquantum-well structures, we can write the above integral as a sum of sub-integrals. In other words, we need to evaluate a set of discrete integrals, instead of one continuous integral. To determine the electric field at each interface, we apply the boundary conditions shown in Fig. 5.1(b).

$$\tilde{E}(0) = 0$$

$$\tilde{E}(x_1) = e^{-\int_0^{x_1} P dx''} \int_0^{x_1} Q(x') e^{\int_0^{x'} P dx''} dx'$$

$$= e^{-P_1 l_1} I_{01}$$

where I_{01} represents the integral. Similarly, at $x = x_2$,

$$\tilde{E}(x_2) = e^{-\int_0^{x_2} P dx''} \int_0^{x_2} Q(x') e^{\int_0^{x'} P dx''} dx'$$

$$= e^{-(P_1 l_1 + P_2 l_2)} \{ \int_0^{x1} Q_1 e^{\int_0^{x'} P dx''} dx' + \int_{x_1}^{x_2} Q_2 e^{\int_0^{x'} P dx''} dx' \}$$

$$= e^{-(P_1 l_1 + P_2 l_2)} \{ I_{01} + I_{12} \}$$

Note that the main integral is split into two sub-integrals, I_{01} and I_{12}, because the integration over x' extends over two sections. In a similar fashion, we find the electric field at each interface x_3, x_4, etc

$$\tilde{E}(x_3) = e^{-\int_0^{x_3} P dx''} \int_0^{x_3} Q(x') e^{\int_0^{x'} P dx''} dx'$$

$$= e^{-(2P_1 l_1 + P_2 l_2)} \{ I_{01} + I_{12} + I_{23} \}$$

$$\tilde{E}(x_4) = e^{-\int_0^{x_4} P dx''} \int_0^{x_4} Q(x') e^{\int_0^{x'} P dx''} dx'$$

$$= e^{-(2P_1 l_1 + 2P_2 l_2)} \{I_{01} + I_{12} + I_{23} + I_{34}\}$$

.

.

.

Sub-integrals I_{01}, I_{12}, I_{23}, etc are evaluated in the Appendix B. We rewrite the above given expressions for electric field by substituting the expressions of I_{01}, I_{12}, I_{23}, etc.

$$\tilde{E}(0) = 0$$

$$\tilde{E}(x_1) = \frac{Q1}{P1}[-e^{-P_1 l_1} + 1] + \frac{Q2}{P2}[\ 0\ ]$$

$$\tilde{E}(x_2) = \frac{Q1}{P1}[-e^{-(P_1 l_1 + P_2 l_2)} + e^{-P_2 l_2}] + \frac{Q2}{P2}[-e^{-(P_1 l_1 + P_2 l_2)} + 1]$$

$$\tilde{E}(x_3) = \frac{Q1}{P1}[-e^{-(2P_1 l_1 + P_2 l_2)} + e^{-(P_1 l_1 + P_2 l_2)}) - e^{-P_1 l_1} + 1]$$

$$+ \frac{Q2}{P2}[\ -e^{-(P_1 l_1 + P_2 l_2)} + e^{-P_1 l_1}]$$

$$\tilde{E}(x_4) = \frac{Q1}{P1}[-e^{-(2P_1 l_1 + 2P_2 l_2)} + e^{-(P_1 l_1 + 2P_2 l_2)} - e^{-(P_1 l_1 + P_2 l_2)} + e^{-P_2 l_2}]$$

$$+ \frac{Q2}{P2}[-e^{-(P_1 l_1 + 2P_2 l_2)} - e^{-(P_1 l_1 + P_2 l_2)} - e^{-P_2 l_2} + 1]$$

$$\begin{aligned}\tilde{E}(x_5) = \frac{Q_1}{P_1}[&-e^{-(3P_1l_1+2P_2l_2)}+e^{-(2P_1l_1+2P_2l_2)}-e^{-(2P_1l_1+P_2l_2)}\\ &+e^{-(P_1l_1+P_2l_2)}-e^{-P_1l_1}+1]\\ &+\frac{Q_2}{P_2}[-e^{-(2P_1l_1+2P_2l_2)}+e^{-(2P_1l_1+P_2l_2)}-e^{-(P_1l_1+P_2l_2)}+e^{-P_1l_1}]\end{aligned}$$

.

.

$$\begin{aligned}\tilde{E}(x_N) = \frac{Q_1}{P_1}[&-e^{-(\frac{N+1}{2}P_1l_1+\frac{N-1}{2}P_2l_2)}+e^{-(\frac{N-1}{2}P_1l_1+\frac{N-1}{2}P_2l_2)}\\ &-e^{-(\frac{N-1}{2}P_1l_1+\frac{N-2}{2}P_2l_2)}+e^{-(P_1l_1+P_2l_2)}-e^{-P_1l_1}+1]\\ &+\frac{Q_2}{P_2}[-e^{-(\frac{N-1}{2}P_1l_1+\frac{N-1}{2}P_2l_2)}+e^{-(\frac{N-1}{2}P_1l_1+\frac{N-2}{2}P_2l_2)}\\ &-e^{-(\frac{N-1}{2}P_1l_1+\frac{N-2}{2}P_2l_2)}-e^{-(P_1l_1+P_2l_2)}+e^{-P_1l_1}]\end{aligned}$$

if N is an odd number. If N is an even number, we obtain

$$\begin{aligned}\tilde{E}(x_N) = \frac{Q_1}{P_1}[&-e^{-(\frac{N+1}{2}P_1l_1+\frac{N-1}{2}P_2l_2)}+e^{-(\frac{N-1}{2}P_1l_1+\frac{N-1}{2}P_2l_2)}\\ &-e^{-(\frac{N-1}{2}P_1l_1+\frac{N-3}{2}P_2l_2)}-e^{-(P_1l_1+P_2l_2)}+e^{-P_2l_2}]\\ &+\frac{Q_2}{P_2}[-e^{-(\frac{N}{2}P_1l_1+\frac{N}{2}P_2l_2)}+e^{-(\frac{N-2}{2}P_1l_1+\frac{N}{2}P_2l_2)}\\ &-e^{-(\frac{N-2}{2}P_1l_1+\frac{N-2}{2}P_2l_2)}+e^{-(P_1l_1+P_2l_2)}-e^{-P_2l_2}+1].\end{aligned}$$

As shown in Fig. 5.1b, the last section of the multiquantum-well layers has a small band-gap. This implies that N is an odd number in our situation.

Note that the rightmost term in each bracket that has a coefficient Q_1/P_1 is equal to unity when N is an odd number. If N is an odd number, the rightmost term in each bracket which has a coefficient Q_2/P_2 is equal to unity. Hence summation of the electric field at each interface results in the following expression

$$\sum_{i=0}^{N} \tilde{E}(x_i) = \frac{Q1}{P1}[1+0+1+0+\cdot\cdot\cdot+0+1+\text{exponential terms}] + \frac{Q2}{P2}[0+1+0+1+\cdot\cdot\cdot+1+0+\text{exponential terms}] \tag{5.23}$$

where the contribution of the exponential terms is negligible with respect to unity because of the following reasons. Firstly, each exponential term has an alternating sign, thus reducing the contribution to the overall summation. Secondly, each exponential term becomes smaller as N increases. Therefore we can rewrite Eq. (5.23)

$$\sum_{i=0}^{N} \tilde{E}(x_i) = \frac{N}{2}\left(\frac{Q_1}{P_1} + \frac{Q_2}{P_2}\right) \tag{5.24}$$

The voltage across the depletion region is given by the line integral of the electric field, i.e.,

$$\tilde{V} = -\int_0^L \tilde{E}dx \qquad (5.25)$$

For the multiquantum-well structures, we get

$$\tilde{V} = -\{ \sum_{i=\text{odd num.}}^{N} \tilde{E}(x_i)\Delta x_i + \sum_{i=\text{even num.}}^{N} \tilde{E}(x_i)\Delta x_i \}$$

$$= \frac{Nl_1}{2}\frac{Q_1}{P_1} + \frac{Nl_2}{2}\frac{Q_2}{P_2} \qquad (5.26)$$

To evaluate Eq.(5.26) we use Eq.(5.20) for P_1, P_2 and modified Eq. (5.21) as follows

$$Q = -\frac{(1+i\omega\tau_n)\tau_{2n}}{\varepsilon(1+i\omega\tau_{2n})\tau_n v_n}\tilde{J} = Q'\tilde{J} \qquad (5.27)$$

where we put $\tilde{\gamma}$ equal to zero, since we are interested in finding the small-signal impedance. Using Eq.(5.26)-(5.27). The impedance is found from

$$Z = \frac{\tilde{V}}{\tilde{J}A} = \frac{Nl_1 Q_1'}{2\ P_1} + \frac{Nl_2}{2}\frac{Q_2'}{P_2} \qquad (5.28)$$

Let $L_1 = Nl_1/2$ and $L_2 = Nl_2/2$, then

$$Z = \frac{L_1 Q_1'}{P_1 A} + \frac{L_2 Q_2'}{P_2 A} \qquad (6.29)$$

Upon substituting Eqs. (5.20) and (5.27) into (5.29)

$$Z = \frac{L_1}{\varepsilon_1 A(i\omega + \frac{1}{\tau_{1\Omega}})} + \frac{L_2}{\varepsilon_2 A(i\omega + \frac{1}{\tau_{2\Omega}})}$$

$$= \frac{L_1}{\sigma_1 A(1+i\omega\tau_{1\Omega})} + \frac{L_2}{\sigma_2 A(1+i\omega\tau_{2\Omega})} \tag{5.30}$$

where we used the definition of the dielectric relaxation time i.e., $\tau_\Omega = \varepsilon/\sigma$. To illustrate the physical meaning of Eq. (5.30), we use the following definitions

$$R = \frac{L}{\sigma A} \quad \text{and} \quad C = \frac{\varepsilon A}{L}$$

Consequently, Eq. (5.30) yields

$$Z = \frac{R_1}{1+i\omega R_1 C_1} + \frac{R_2}{1+i\omega R_2 C_2} \tag{5.31}$$

As Eq. (5.31) indicates, the overall impedance of the multiquantum-well structures is equal to the series connection of two kinds of impedances, while the one with subscript 1 corresponds to the small band-gap section, while the other with subscript 2 is the impedance of the large band-gap section. Each impedance can be represented tas a resistor and a capacitor in parallel.

For later use, we define an impedance correction factor, f_z as follows

$$f_z \equiv 1 + \frac{L_1}{L_2} \frac{\varepsilon_2 \tau_{1\Omega}(1+i\omega\tau_{2\Omega})}{\varepsilon_1 \tau_{2\Omega}(1+i\omega\tau_{2\Omega})} \tag{5.32}$$

Then Eq. (5.30) can be rewritten as

$$Z = f_z \frac{\tau_{2\Omega} L_2}{\varepsilon_2 A(1+i\omega\tau_{2\Omega})} \tag{5.33}$$

In our case $L_1 = L_2 = L/2$. Then, Eq. (5.33) yields

$$Z = f_z \frac{\tau_{2\Omega} L}{2\varepsilon_2 A(1+i\omega\tau_{2\Omega})} \tag{5.34}$$

Eq. (5.34) will be used later to determine the current fluctuation noise.

The transport equation (5.19) that we have used so far can yield the noise also. Previously, we neglected the fluctuation terms to find the impedance. Now we put $\tilde{J} = 0$ in Eq. (5.21) to determine the terminal noise in terms of open-circuited voltage fluctuations. We rewrite Eq. (5.21) with $\tilde{J} = 0$

$$Q = \frac{q\tau_{2n}}{\varepsilon(1+i\omega\tau_{2n})}\tilde{\gamma} \tag{5.21a}$$

For the open-circuit voltage we find

$$\tilde{V}(L,\omega) = -\int_0^L \tilde{E}(x,\omega)\,dx \tag{5.35}$$

where the electric field expression contains the fluctuations implicitly. The spectral density of the open-circuit voltage fluctuation can be found from

$$\begin{aligned} S_V &= \frac{2}{T}\langle\tilde{V}(L,\omega)\tilde{V}^*(L,\omega)\rangle \\ &= \frac{2}{T}\langle\left[\int_0^L \tilde{E}(x,\omega)\,dx\right]\left[\int_0^L \tilde{E}^*(x,\omega)\,dx\right]\rangle \end{aligned} \tag{5.36}$$

where < > denotes average value and T is a given time interval. To evaluate Eq.(5.33), we split the integral into N sections as we did for the impedance. Eq.(5.36) can be rewritten as

$$
\begin{aligned}
S_V = \frac{2}{T} < & \left[\int_0^{x_1} \tilde{E}(x,\omega)dx + \int_{x_1}^{x_2} \tilde{E}(x,\omega)dx + \int_{x_2}^{x_3} \tilde{E}(x,\omega)dx + \cdots + \int_{x_{N-1}}^{x_N} \tilde{E}(x,\omega)dx \right] \\
& \left[\int_0^{x_1} \tilde{E}^*(x',\omega)dx' + \int_{x_1}^{x_2} \tilde{E}^*(x',\omega)dx' + \int_{x_2}^{x_3} \tilde{E}^*(x',\omega)dx' + \cdots + \int_{x_{N-1}}^{x_N} \tilde{E}^*(x',\omega)dx' \right] > \\
= \frac{2}{T} & \left[\int_0^{x_1}\int_0^{x_1} \overline{\tilde{E}(x,\omega)\tilde{E}^*(x',\omega)}\,dxdx' + \int_{x_1}^{x_2}\int_{x_1}^{x_2} \overline{\tilde{E}(x,\omega)\tilde{E}^*(x',\omega)}\,dxdx' \right. \\
& + \int_{x_2}^{x_3}\int_{x_2}^{x_3} \overline{\tilde{E}(x,\omega)\tilde{E}^*(x',\omega)}\,dxdx' + \cdot\ \cdot + \int_{x_{N-1}}^{x_N}\int_{x_{N-1}}^{x_N} \overline{\tilde{E}(x,\omega)\tilde{E}^*(x',\omega)}\,dxdx' \\
& \left. + \int_0^{x_1}\int_{x_1}^{x_2} \overline{\tilde{E}(x,\omega)\tilde{E}^*(x',\omega)}\,dxdx' + \int_0^{x_1}\int_{x_2}^{x_3} \overline{\tilde{E}(x,\omega)\tilde{E}^*(x',\omega)}\,dxdx' + \cdot\ \cdot\ \cdot \right]
\end{aligned}
\tag{5.37}
$$

The evaluation of the double integrals in the above equation is given in the Appendix C. Note that the open-circuit expression for the electric field $\tilde{E}(x,\omega)$ has fluctuation terms only. Hence the product of $\tilde{E}(x,\omega)$ with $\tilde{E}^*(x,\omega)$ yields the product of fluctuation terms i.e., $\tilde{\gamma}(x,\omega)\tilde{\gamma}^*(x',\omega)$. The average value of this product is proportional to a spectral density and is given by g-r noise theory. If we write this

$$S_\gamma(x,x',\omega) = \frac{2}{T}\,\overline{\tilde{\gamma}(x,\omega)\tilde{\gamma}^*(x',\omega)}$$
$$= K_\gamma \delta(x-x') \qquad (5.38)$$

Since S_γ contains delta function, the cross terms in the last line of Eq. (5.37) become zero. This means that g-r noise sources in each quantum-well are statistically independent of each other. Also note that the double integrals become single integrals because of the delta function in the integrand.

Using a result we obtained from Appendix C

$$\frac{2}{T}\int_{x_{n-1}}^{x_n}\int_{x_{n-1}}^{x_n}\overline{\tilde{E}(x,\omega)\tilde{E}^*(x',\omega)}\,dx\,dx' \sim 0;\ \text{If N is an odd number}$$

$$\sim K_{\gamma_n}\left(\frac{\overline{Q_2' Q_2'^*}}{P_2 P_2^*}\right) l_2;\ \text{If N is an even number}$$

We rewrite Eq. (5.37) and find

$$S_{V_n} = \frac{2}{T}\sum_{i=1}^{N}\int_{x_{i-1}}^{x_i}\int_{x_{i-1}}^{x_i}\overline{\tilde{E}(x,\omega)\tilde{E}^*(x',\omega)}\,dx\,dx'$$

$$= \frac{2}{T}\cdot\left(\frac{\overline{Q_2' Q_2'^*}}{P_2 P_2^*}\right) l_2 K_{\gamma_n}\ [0 + 1 + 0 + 1 + \cdot\cdot\cdot\ 0 + 1]$$

$$= \frac{Nl_2}{T}\left(\frac{\overline{Q_2' Q_2'^*}}{P_2 P_2^*}\right) K_{\gamma_n} \tag{5.39}$$

For the structures where $l_1 = l_2 = l$, Eq. (5.39) can be rewritten as

$$S_{V_n} = \frac{Nl}{T}\left(\frac{\overline{Q_2' Q_2'^*}}{P_2 P_2^*}\right) K_{\gamma_n} \tag{5.39a}$$

To evaluate Eq.(5.39a), we use Eq.(5.20), (5.21) and (5.38), and find

$$S_{V_n} = Nl \frac{q^2 v_n^2 \tau_n^2 \tau_\Omega^2}{\varepsilon^2 (1+\omega^2\tau_n^2)(1+\omega^2\tau_\Omega^2)} K_{\gamma_n} \tag{5.40}$$

Concerning the fluctuation terms in Eq.(5.46), we assume that the random emptying and filling of traps results in full shot noise, allowing us to write the noise spectrum as follows

$$K_{\gamma_n} = \frac{4n_o}{A\tau_{1n}} \tag{5.41}$$

Using this expression, Eq. (5.40) can be rewritten as

$$S_{V_n} = Nl \frac{q^2 v_n^2 \tau_{1n}^2 \tau_\Omega^2}{\varepsilon^2 (1+\omega^2\tau_\Omega^2)} \left(\frac{4n_o}{A\tau_n}\right)$$

$$= \frac{4Nl_2^2 q^2 n_o v_n \tau_\Omega^2}{A\varepsilon^2 (1+\omega^2\tau^2)} \left(\frac{\tau_{1n}}{\tau_f}\right) \tag{5.42}$$

where τ_{fn} is the flight time for the electrons between the adjacent quantum-wells. In Eq. (5.42), we used $v_n = l/\tau_{fn}$. The spectral density of the current fluctuations can be found with the help of Eq. (5.41)

$$S_{I_n} = \frac{S_{v_n}}{|Z|^2} = \frac{4Nl^2q^2n_ov_n\tau_\Omega^2}{A\varepsilon^2(1+\omega^2\tau^2)}\left(\frac{\tau_{1n}}{\tau_f}\right)\cdot\frac{4\varepsilon^2A^2(1+\omega^2\tau_\Omega^2)}{N^2l^2\tau_\Omega^2}\cdot\frac{1}{f_z^2}$$

$$= \frac{16qqn_ov_nA}{N}\left(\frac{\tau_{1n}}{\tau_f}\right)\cdot\frac{1}{f_z^2} \qquad (5.43)$$

Note that in Eq. (5.32) the impedance correction factor f_z is approximately 2 at low frequencies. Using the value of f_z and $I = qn_ov_nA$, Eq. (5.43) can be rewritten as

$$S_{I_n} = \frac{4qI}{N}\left(\frac{\tau_{1n}}{\tau_f}\right) \qquad (5.44)$$

From this result, we note that the current noise level critically depends on the number N of heterostructure layers and on the ratio (τ_{1n}/τ_f). The bias dependence of the noise level can be explained in terms of these two parameters. If the quantum-wells are depleted by applying the high bias voltage, then $\tau_{1n} = N\tau_f$ and full-shot noise is obtained. At low bias, however, the time constant ratio becomes one in the undepleted quantum-well layers and a strong suppression of the noise will occur due to a factor of 1/N, where N is the number of undepleted quantum-wells.

As we will see in chapter VI, as reverse bias increases, the quantum-well layers in the i-region are depleted gradually i.e., one quantum-well at a time. Thus, reduction in the number N of the undepleted quantum-wells results in the increase in the noise level.

5.3. Trapping in Heterojunction Interface States

As mentioned in the introduction, the development of the theory presented in this section was prompted by the frequency dependence of the noise spectrum in the mid-frequency range. We assume the levels of traps in the forbidden band-gap as shown in Fig. 5.2a. The difference with the conventional-type traps is that the traps in this case are located at discrete positions, i.e., only at the heterostructure interfaces.

Fig. 5.2a shows the band diagram for the interface trap model. In order to contribute to an electrical conduction, the electrons in each trap level should transit to the energy level of the extended conduction band (E_{ec}). This electron transition consists of a transition between a trap energy level (E_T) and the localized conduction band (E_{lc}), followed by a transition from the E_{lc} state to the E_{ec} state. The latter is the quantum-well detrapping and detrapping process discussed in the previous section. Since the quantum-well trapping and detrapping is a very fast process, the above two-step

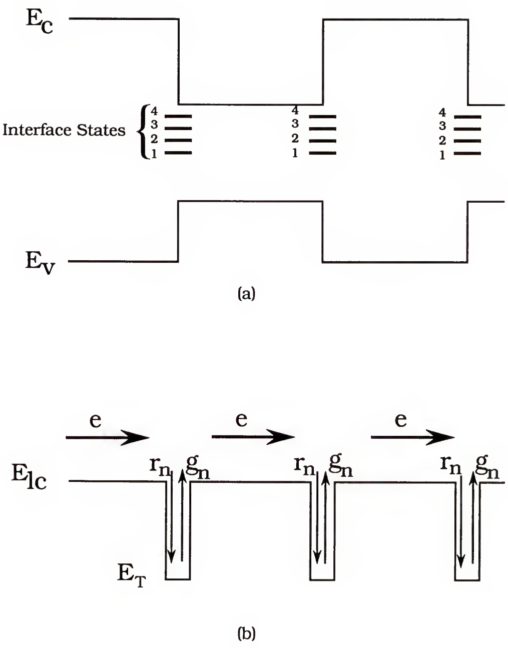

Fig 5.2 (a) Heterojunction interface traps
(b) simplified interface-trap model

process can be approximated by a one-step process, namely, the E_T-E_{1c} transition is assumed to be identical to the E_T-E_{ec} transition. This transition is shown in Fig. 5.2(b).

With the carrier transitions and flow as indicated in Fig. 5.1(b), the kinetic equations become

$$\frac{dn}{dt} = g_n - r_n + \frac{1}{q}\frac{dJ_n}{dx} + \gamma \tag{5.45}$$

$$\frac{d\hat{n}}{dt} = -g_n + r_n - \gamma \tag{5.46}$$

In the above equations, n and $\hat{n}$ are the free carrier density and the trapped carrier density, respectively. γ represents the fluctuations in the transition rates. If we neglect diffusion current and include the displacement current

$$J = qn\mu_n E + \varepsilon\frac{\partial E}{\partial t}. \tag{5.47}$$

Poisson's equation becomes

$$\frac{dE}{dx} = -\frac{q}{\varepsilon}(n + \hat{n} - N_d), \tag{5.48}$$

where N_d denotes the impurity density.

For the generation and recombination terms we have

$$g_n = e_n n = C_n n_1 \hat{n} \tag{5.49}$$

$$r_n = C_n n(N_d - \hat{n}) \tag{5.50}$$

where C_n is the capture coefficient, and n_1 is the density of electrons in the conduction band when the Fermi level coincides with the trapping level.

By substituting equations (5.49) - (5.50) into Eq. (5.46) and linearization, we have the following A.C. equation for the trapped electron density in the interface states

$$\begin{aligned}\frac{d\Delta\hat{n}}{dt} &= \Delta n(N_t - \hat{n})C_n - \Delta\hat{n}(n_1 + n_o)C_n - \gamma \\ &= \frac{\Delta n}{\tau_1} - \frac{\Delta\hat{n}}{\tau_2} - \gamma \qquad (5.51)\end{aligned}$$

with

$$\tau_1^{-1} = C_n(N_d - \hat{n}) \qquad (5.52)$$

$$\tau_2^{-1} = C_n(n_1 + n_o) \qquad (5.53)$$

Let

$$\tau^{-1} = \tau_1^{-1} + \tau_2^{-1} \qquad (5.54)$$

We apply Fourier analysis on the linearized A.C.equations of (5.47), (5.48) and (5.51). With some algebra, we obtain the following first order differential equation

$$\frac{d\tilde{E}}{dx} - \frac{\tau_2(1+i\omega\tau)(1+i\omega\tau_\Omega)}{(1+i\omega\tau_2)\tau\tau_\Omega v_n}\tilde{E} = -\frac{(1+i\omega\tau)\tau_2}{\varepsilon(1+i\omega\tau_2)\tau v_n}\tilde{J} + \frac{q\tau_2}{\varepsilon(1+i\omega\tau_2)}\tilde{\gamma} \qquad (5.55)$$

We rewrite Eq.(5,55) in the following form

$$\frac{d\tilde{E}}{dx} + P\tilde{E} = Q \qquad (5.55a)$$

where

$$P = \frac{\tau_2 (1+i\omega\tau)(1+i\omega\tau_\Omega)}{(1+i\omega\tau_2)\tau\tau_\Omega v_n} \qquad (5.56)$$

$$Q = -\frac{(1+i\omega\tau)\tau_2}{\varepsilon(1+i\omega\tau_2)\tau v_n}\tilde{J} + \frac{q\tau_2}{\varepsilon(1+i\omega\tau_2)}\tilde{\gamma} \qquad (5.57)$$

Solving Eq.(5.55), we obtain for the spectral density of the voltage fluctuations

$$S_V = \frac{Nl}{T}\left(\frac{\overline{Q_2' Q_2'^{*}}}{P_2 P_2^{*}}\right) K\gamma \qquad (5.58)$$

where subscript '2' denotes the value of the even-numbered section. Substitution of Eqs.(5.56) and (5.57) and (5.58) yields

$$S_V = \frac{4Nlq^2 n_o v_n^2 \tau^2 \tau_\Omega^2}{A\varepsilon^2 (1+\omega^2\tau_\Omega^2)(1+\omega^2\tau^2)\tau_1} \qquad (5.59)$$

The current spectral density is found with the help of the impedance

$$S_I = \frac{S_V}{|Z|^2} = \frac{4Nlq^2 n_o v_n^2 \tau^2 \tau_\Omega^2}{A\varepsilon^2 (1+\omega^2\tau_\Omega^2)(1+\omega^2\tau^2)\tau_1} \cdot \frac{\varepsilon^2 A^2 (1+\omega^2\tau_\Omega^2)}{N^2 l^2 \tau_\Omega^2}$$

$$= 4qI \frac{\tau^2}{t_L \tau_1} \frac{1}{(1+\omega^2\tau^2)} \; . \qquad (5.60)$$

Eq.(5.60) is a well known g-r noise spectrum result and shows the Lorentzian-type frequency response.

So far we have considered only a single trap level. For the multilevel trap system, we follow the same procedure as Tehrani [71] did. That is, we assume a linear superposition of multiple Lorentzian components, each with different trap parameters. Thus we get the following spectrum

$$S_I = 4qI \sum_i \frac{\tau_i}{t_L} \left(\frac{\tau_i}{\tau_{1i}}\right) \frac{1}{(1+\omega^2\tau_i^2)} \tag{5.61}$$

where

$$\tau_{1i}^{-1} = C_{ni}(N_{ti} - \hat{n}_i) \tag{5.62}$$

$$\tau_{2i}^{-1} = C_n(n_{1i} + n_o) \tag{5.63}$$

$$\tau_i^{-1} = \tau_{1i}^{-1} + \tau_{2i}^{-1} \tag{5.64}$$

5.4. Computer Calculations of the Trapping Noise

It is difficult to present a quantitative analysis of the trapping noise of the multiquantum-well structures because of the many unknown parameters. For this reason we can only hope to carry out qualitative calculations based on the limited information available from the experimental results.

We begin with a calculation of the capture cross section of the quantum-well traps. Unlike the capture cross section of an ordinary trap center (see Fig. 5.3) which has a typical value of 10^{-20} m^2, a heterostructure quantum-well has a very large cross section, i.e. ~ 10^{-8} m^2, because the capture cross section is associated with the total area of the heterostructure interface. If we use this cross section value, we obtain a very small, unrealistic value for our time constant. Therefore, we need to modify the definition of capture cross section in the context of quantum-well structures.

For free carriers to be captured by a trap, they need to lose energy through a scattering process. According to Whiteside [72], the scattering mean free path is of the order of 10 Å for energies of about 1.0 ev. Then we are allowed to assume that at every 10 Å, free carriers experience scattering, loose energy and can be captured by the traps. This idea introduces the following approximation. Instead of modifying the capture cross section, we use the standard value of $(10\ \text{Å})^2$ and we assume that the traps are spaced 10 Å apart forming a lattice as shown in Fig. 5.4. Then we can calculate an effective trap density

$$N_A = \frac{\text{number of traps}}{\text{unit volume}} = \frac{1}{(10\text{Å})^3} = 10^{27}\text{m}^{-3} \qquad (5.65)$$

This value leads to values of τ_{1n} and τ_{2n} of

$$\tau_{1n} = \frac{1}{C_n N_A} = (\delta_c v_{th} N_A)^{-1} \sim 3.8 \times 10^{13} \qquad (5.66)$$

As shown in Eq. (5.43) the evaluation of the noise spectra depends critically on the time constant τ_{1n}. Calculation

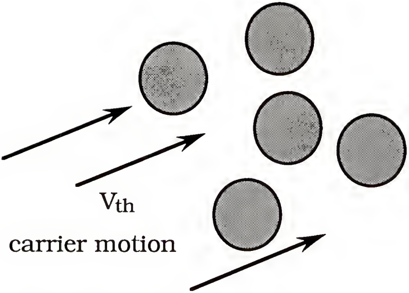

Figure 5.3 The apture cross section of ordinary trap centers.

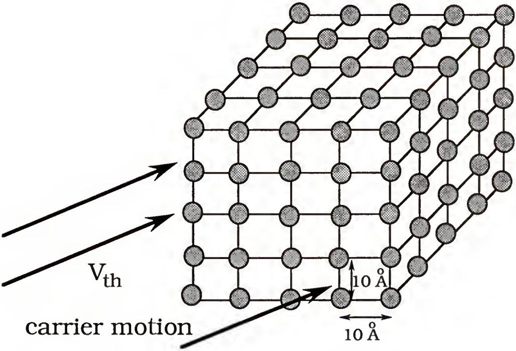

Figure 5.4 The effectice capture cross section of heterostructure quantum-wells.

of the current noise spectrum associated with quantum-well trapping can be performed by using Eq.(5.31), (5.43) and the parameters presented in Table 5.1.

Table 5.1
Parameters used for the calculation
of the quantum-well trapping noise

I, device current	1 μA
L,width of the MQW region	$2\cdot10^{-6}$ m
N, number of heterostructure layers	200 (for UM505)
A, cross section area of the device	$3.14\cdot10^{-8}$ m^2
v_n, electron velocity	$1\cdot10^{5}$ m/sec
C_{nw}, capture rate of the quantum-well traps	$2.6\cdot10^{-15}$ m/sec
N_t, density of quantum-well traps in E_c	$1\cdot10^{27}$ m^{-3}
t_L, transit time across the MQW region	$2\cdot10^{-11}$sec
τ_f, flight time between each quantum-well	$2\cdot10^{-13}$sec
τ_Ω, dielectric relaxation time	$2\cdot10^{-6}$sec
ε, relative dielectric constant	12
ε_o, free space dielectric constant	$8.85\cdot10^{-12}$ f/m

The result of this calculation indicates that the spectrum is flat up to tens of GHz. As expected in the introduction, the magnitude of the low-frequency spectrum plateau value is reduced by a factor of 1/N, where N is the number of the heterostructure layers in the multiquantum-well device. In other words, this distinctive sub-shot noise phenomenon is strong evidence for the occurrence of the trapping and detrapping in the quantum-wells.

Next we focus on Eq. (5.61). To explain the measured noise spectra which show approximately 1/f noise like behavior, a superposition of several Lorentzians with different time constants was considered by Tehrani [71]. As indicated by van Rheenen [73] superposition to 1/f is possible only when the time constants are a factor of ten or more apart. Then, we are allowed to treat a trap level in the forbidden gap separately and single trap level theory applies to the multi-level trap situation.

Eq.(5.61) shows that each Lorentzian is characterized by a plateau value and a time constant whose reciprocal value is the cutoff frequency. To have a 1/f noise like spectrum, we noted that plateau value of each Lorentzian should vary inverse proportionally to the frequency. Since the transit time t_L has a fixed value, having a statistical factor τ/τ_1 independent of the degree of trap occupancy is able to realize latter condition. The time constants τ and τ_1 are known to be a function of the following trap parameters: activation energy, carrier and trap densities, spin degeneracy, and capture cross section. To evaluate Eq.(5.62) and (5.63), we present the following expressions.

The average value of the trapped carrier density is given by

$$\hat{n}_o = \frac{N_t}{1+\frac{1}{g}\exp\left(\frac{E_T-E_F}{kt}\right)} \tag{5.67}$$

where g denotes spin degeneracy. The average free carrier density and the Shockely-Read parameter is expressed by

$$n_o = N_c \exp\left(\frac{E_F-E_c}{kt}\right) \tag{5.68}$$

$$n_1 = \frac{N_c}{g} \exp\left(\frac{E_T-E_c}{kt}\right) \tag{5.69}$$

respectively.

To explain the measured noise spectrum, we need to extract an approximate value for the statistical factor τ/τ_1 from Fig. 5.5. If we substitute the value of the spectral density at the corner frequency into Eq.(5.60), we obtain the following condition

$$\frac{\tau}{\tau_1} = 10^{-3} \sim 10^{-5} \tag{5.70}$$

Using Eq.(5.62) and (5.63), we find

$$\frac{\tau_2}{\tau_1} \simeq \frac{\tau}{\tau_1} = \frac{N_t-\hat{n}_o}{n_1+n_o} \tag{5.71}$$

If $\hat{n}_o$ is negligibly small compared to N_t and if n_o is smaller than n_1, the statistical factor is about constant.

Then, by comparing Eq.(5.68) and (5.69), we note that the Fermi energy level must be located below the trap energy level. Since our multiquantum-well structures are undoped, we assume that the Fermi energy level lies around mid-gap. Next we assume the presence of several discrete trap levels located between the Fermi level and the conduction band. We label the trap levels as shown in Table 5.2. Using these parameters, we obtained a 1/f noise like spectrum. If we combine this result and the result of the high-frequency spectrum, we are able to explain the entire spectrum ranging from 1 KHz up to 100 GHz (see Fig. 5.5).

Table 5.2

Trap parameters used for the calculation of the interface trapping noise

Trap #	N_t (m^{-3})	E_{act} (ev)	C_n (m^3/sec)	τ(sec)	f_c (Hz)
1	10^{14}	0.318	10^{-15}	10^{-3}	10^{3}
2	10^{15}	0.259	10^{-15}	10^{-4}	10^{4}
3	10^{16}	0.199	10^{-15}	10^{-5}	10^{5}
4	10^{17}	0.139	10^{-15}	10^{-6}	10^{6}
5	10^{18}	0.079	10^{-15}	10^{-7}	10^{7}
6	10^{19}	0.019	10^{-15}	10^{-8}	10^{8}

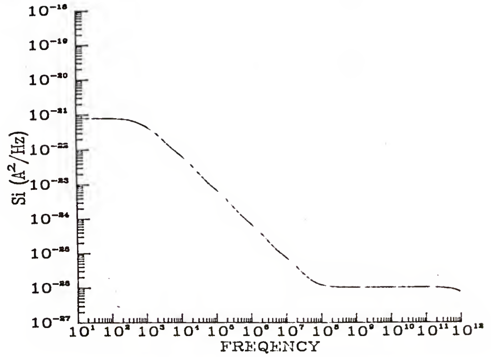

Figure 5.5 Noise spectrum obtained by the computer simulation

CHAPTER VI
EXPERIMENTS ON MULTIQUANTUM-WELL (MQW) HETEROSTRUCTURE P-I-N PHOTODIODES

6.1. Introduction

An experimental study on heterostructure p-i-n photodiodes is discussed in this chapter. The emphasis is placed on the noise measurements and their analysis. Together with noise measurements, conventional measurements such as I-V, C-V, impedance (S-parameters) should be performed, since these measurements provide information about the steady-state operating condition of the device. Researchers have been using noise measurement as a powerful tool in studying the microscopic behavior of an electronic device and its physics.

Our initial objective of this study was to measure the impact-ionization coefficient ratios on the heterostructure MQW-APDs using the noise measurement method. When it turned out that we could not obtain a high enough electric field to initiate the impact ionizations in the InGaAs based structures due to the high tunneling current at room temperature, we discovered that some multiquantum-well structures exhibited distinctive sub-shot noise and that this sub-shot noise is dependent on both the structure and the applied bias. So it was decided that sub-shot noise needed to be studied instead. Measurements on three different quantum-well structures were performed and their findings will be presented in this chapter.

In the first section, we will discuss the device structures. In subsequent sections, the experimental set-up, the experimental procedures and the results will be presented with a discussion.

6.2. Device Description

A heterostructure APD in its simplest form is a p^+-i-n^+ diode. Instead of an i-region, an undoped MQW layer is sandwiched between p^+ and n^+ layers. The configuration of the device used in the experiments is shown in Fig. 6.1. The multiquantum-well layer and absorption layers were grown on an n^+ InP substrate by molecular beam epitaxy (MBE) technique at the University of Michigan.

For device UM505, a 2 μm-thick n^+ $In_{0.53}Ga_{0.47}As$ layer for photo-absorption, a 1.8 μm-thick undoped $In_{0.53}Ga_{0.47}As/In_{0.52}Al_{0.48}As$ MQW region and another 2 μm-thick p^+-$In_{0.53}Ga_{0.47}As$ layer for top illumination were subsequently grown. Three different devices with different MQW periods and dimensions were used in the experiments. Detailed information of these devices is given in Table 6.1.

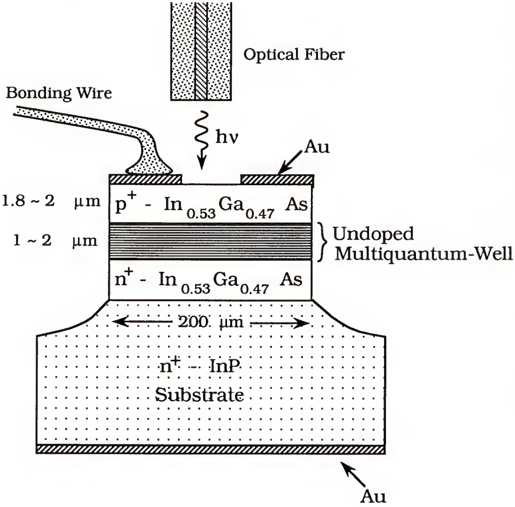

Figure 6.1 Configuration of a multiquantum-well heterostructure p-i-n photodiode

Table 6.1

Device No.	Composition	No. of MQW periods	Barrier Width	Well Width
UM504	$In_{0.53}Ga_{0.47}As/In_{0.52}Al_{0.48}As$	180	30 Å	30 Å
UM505	$In_{0.53}Ga_{0.47}As/In_{0.52}Al_{0.48}As$	100	90 Å	90 Å
UM516	$In_{0.53}Ga_{0.47}As/In_{0.52}Al_{0.48}As$	25	500 Å	500 Å

A window is provided in the metal film on the top p^+-InGaAs layer for illumination. This top illumination gives rise to a photo-generation of electrons and holes. The holes are collected by the top electrode and excess electrons will be injected into the multiquantum-well layers.

When this photodiode is operated at high reverse bias, most of the voltage drop is across the undoped MQW region, resulting in high electric fields, and thus providing the possibility for multiplication. The multiplication process can not take place in the n^+ and p^+ InGaAs layers because the voltage drop across the heavily doped layers is negligibly small. These layers, however, consist of low band-gap material (E_g =0.75 eV) which is suitable for photo-absorption of infrared (1.3 mm and 1.5 mm) wavelengths where material dispersion and optical attenuation are minimum in silica based optical fibers. The multiquantum-well layer consists of two different band-gap materials, i.e., $In_{0.53}Ga_{0.47}As$ (E_g = 0.75eV), and $In_{0.52}Al_{0.48}As$ (E_g = 1.47 eV). At the heterostructure interface the difference in band-gap results in band-edge discontinuities. Recent measurements have shown that 70% of the band-gap difference lies in the conduction band. Thus we assume a conduction-band discontinuity of 0.5eV and a valence-band discontinuity of 0.2eV [74] for our devices. Since carrier transport is perpendicular to the heterostructure interface, electrons and holes experience different potential discontinuities and consequently carriers will lose or acquire different amounts of kinetic energy at each interface.

6.3. D.C. Measurements and Results

Steady state characterizations such as I-V, C-V, and impedance measurements are necessary to understand the device operation and need to be done before the noise characterizations. Measurements were performed at room temperature on the three devices with different MQW structures.

We begin with device UM504 (30 Å - 30 Å). A semiconductor parameter analyzer (HP4145A) was used to measure the reverse dark current-voltage. The result is shown in Fig.6.2. At low bias the reverse dark current is dominated by generation-recombination process in the MQW

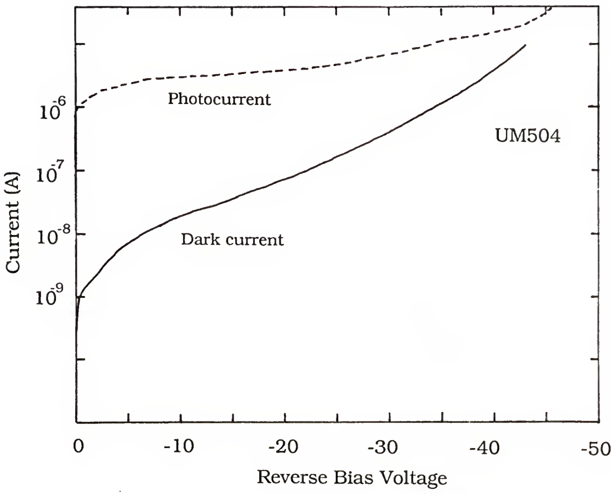

Figure 6.2 Current-voltage (I-V) characteristics.

structure rather than by diffusion in the InGaAs absorption regions, because of the low density of minority carriers in this highly doped material. The rapid increase in the dark current above 15 V is due to Zener tunneling in the low band-gap layers ($In_{0.53}Ga_{0.47}As$). Photocurrent was generated by illuminating the top layer (p^+-InGaAs) with a LED at $\lambda = 1.3$ µm. The reverse current-voltage characteristic was measured with continuous bias. Between 0 and 7 V the increase in the photocurrent is due to enhanced injection of excess electrons into the depletion region as bias increases. Above 7 V, the photocurrent remains constant for a while and increases again at higher bias due to the increasing dark current component. From this I-V characteristic, we see that this device performs similarly to an ordinary bulk device. We did not increase the bias high enough to observe the impact ionization because the tunneling current is already too high.

Fig. 6.3 shows the result of the C-V measurements. The rapid decrease in the junction capacitance between 0 and 0.5 V indicates that the undoped MQW layers are easily depleted by a small bias. Further decrease is due to the depletion at the edge of the InGaAs absorption layers. Above 12 V, the junction capacitance C_j reaches a constant value of 2.77 pF which is quite close to the geometrical value of 2.71 pF.

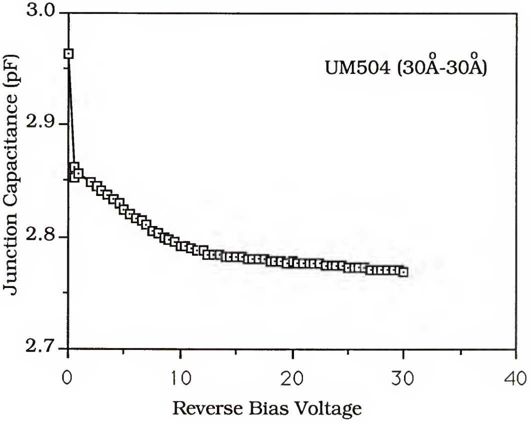

Figure 6.3 Capacitance-voltage (C-V) characteristic

The impedance was measured with an S-parameter analyzer (HP 8510A). The Smith chart plot of the result is shown in Fig. 6.4. To extract the series resistance value we used simulation software (Touchstone) and obtained the value of 30-Ω. This value together with the junction capacitance will be used in the noise data analysis.

Measurements of the I-V characteristics of device UM505 (90 Å - 90 Å) are shown in Fig. 6.5. As in device UM504, below 15 V, the dark current is dominated by generation-recombination processes and diffusion. With increasing bias, the depletion of more quantum-well layers results in a rapid increase in the field assisted thermal generation in the depleted layers. At extremely high bias, Zener tunneling current becomes dominant.

Note that the photocurrent is strongly dependent on reverse bias. Since the carrier generation by photo-absorption is independent of bias, this bias dependent quantum efficiency is attributed to the bias dependent collection process of the carriers. In an ordinary homostructure p-i-n photodiode with separated absorption layer, the carriers are, upon injection into the depletion region, accelerated by the electric field and cross the depletion region. Due to a lack of mobile carriers in this region recombination is unimportant. If there is a potential barrier between the absorption layer and depletion region, however, as in the heterostructure

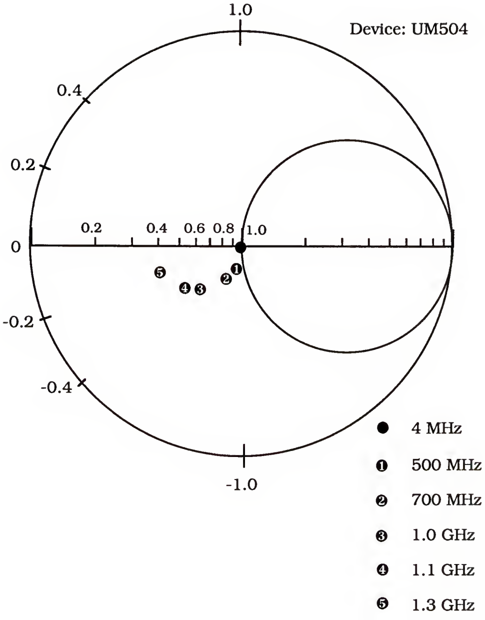

Figure 6.4 A plot of S-parameter (S_{11})

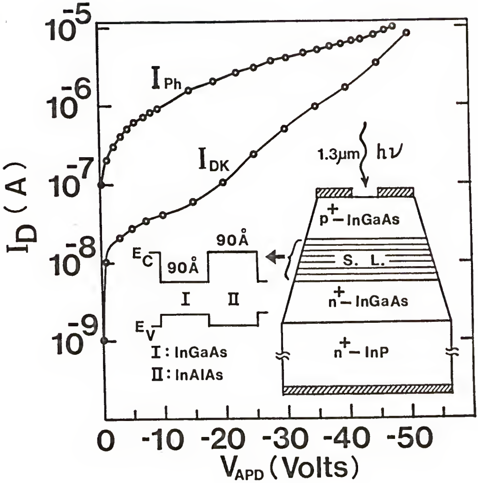

Figure 6.5 I-V characteristics of the device UM505.

photodiode shown in Fig. 6.6, photocurrent will be strongly dependent on the amount of carriers injected over the first few potential barriers. Effectively, these barriers reduce the carrier injection into the depletion region. In other words, an increase in the bias will lead to a reduction in the effective barrier height and consequently to an increase in the photocurrent. In our structure (UM505), the collection efficiency increases gradually as a function of bias. To understand this, we present in Fig. 6.7 the successive band profiles with increasing bias. As shown in this figure, an increase in the bias results in the depletion of more quantum-wells instead of lowering the potential barrier by tilting the band-profile. This weak dependence of the barrier height on the reverse bias accounts for the gradual increase in the quantum efficiency at low bias. In the previous device (UM504) which has a very thin potential barrier, we didn't observe this effect, because the carriers can easily tunnel through the barriers, whereas in an InP/InGaAs single heterojunction, nontransparent structure, Forrest et al. [75] observed that unity collection efficiency is obtained rather abruptly.

At higher bias, however, the potential barrier limiting the carrier injection is fully lowered and the photocurrent is limited by carrier transit across the undepleted quantum-well layers.

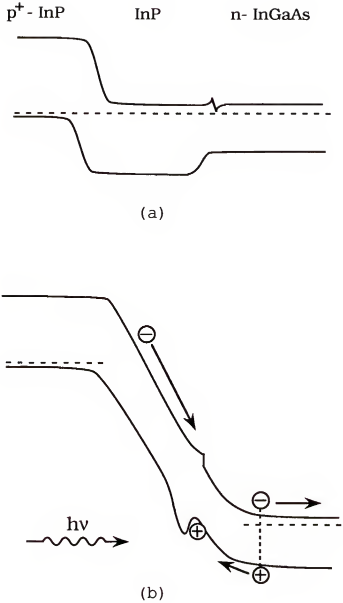

(a)

(b)

Figure 6.6 (a) Equilibrium and (b) reverse-bias energy band diagrams of an InGaAs-InP photodiode with separate absorption and multiplication regions.

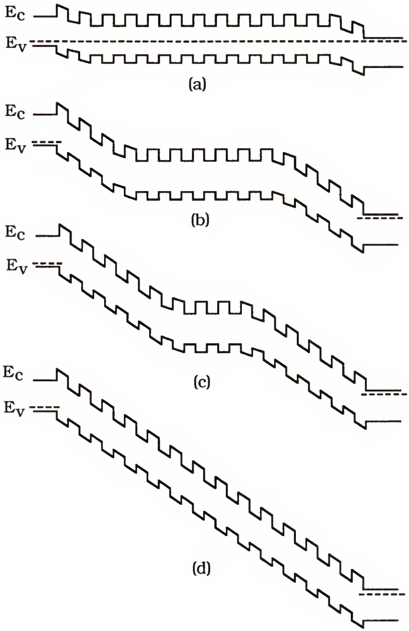

Figure 6.7 Successive depletion of quantum-well layers from (a) low to (d) high bias

C-V measurements are not available for device UM505 , but the calculated value of the geometrical capacitance yields 2.31pF. From this value and from the result of the S-parameter measurement shown in Fig. 6.8, we approximately obtained a series impedance value of 10-Ω.

Device UM516 was measured next. As shown in Fig. 6.9, the I-V characteristic demonstrates the gradual increase in the quantum efficiency as a function of reverse bias. The results of the C-V measurement, shown in Fig. 6.10, also indicate the gradual depletion of the multiquantum-well layers over a wide bias range, i.e. between 0 and 30 V. The reason for the sudden increase in the junction capacitance near zero bias is unknown. The measured junction capacitance C_j at high bias yields 1.35 pF which is close to the geometrical value of 1.17 pF. Fig. 6.11 shows the results of S-parameter measurements. From this data we obtained a series resistance value of 10-Ω.

6.4. Noise Measurement Set-up

One of the common difficulties in noise measurements is to amplify the small noise signal to a measurable level without adding noise contamination from the measuring equipment. This difficulty occurs because noise signals are usually small quantities and are sometimes buried in the background noise. We designed and built a new noise

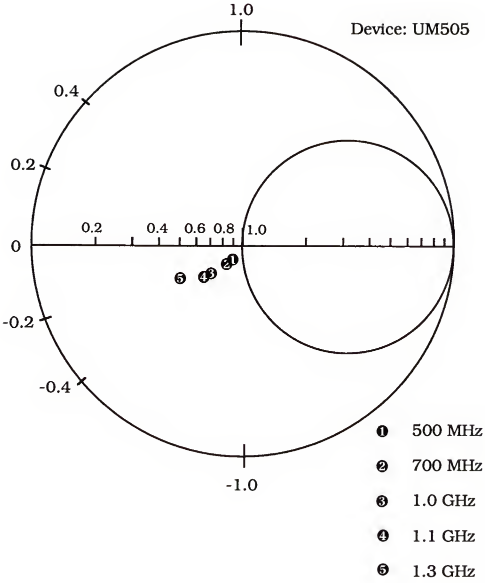

Figure 6.8 A plot of S-parameter (S_{11})

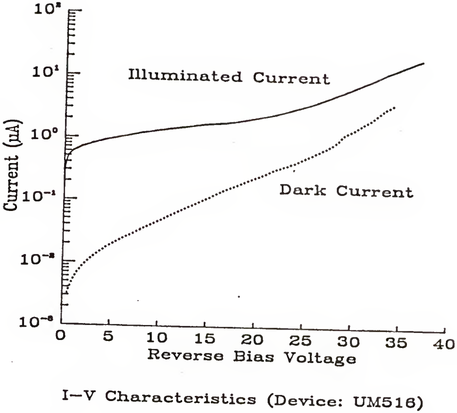

Figure 6.9 I-V characteristics of the device UM516.

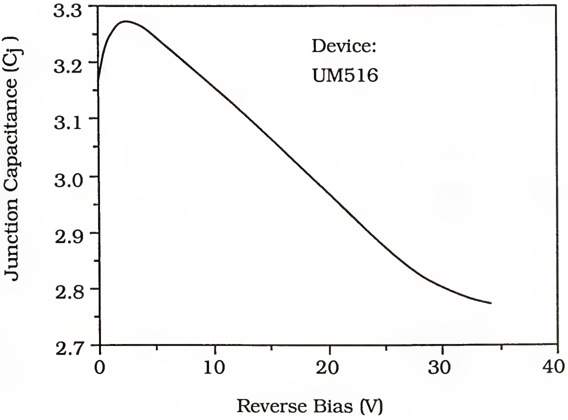

Figure 6.10 C-V characteristics of the device UM516

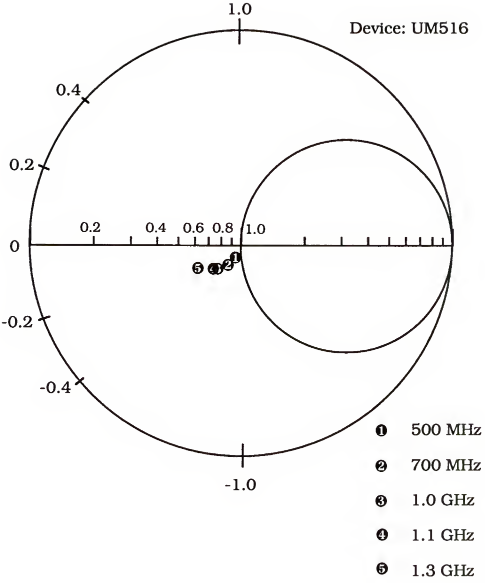

Figure 6.11 A plot of S-parameter (S_{11})

measuring system, improving the sensitivity over that of conventional systems.

To measure a wide frequency range of the noise spectrum, we need to employ several different measurement schemes. Basically we divided our frequency span from 100 Hz to 1 GHz into three frequency ranges because one receiver can't cover the entire frequency span. In addition it is desirable to use different measuring set-ups to have a maximum sensitivity for each frequency range. All measurement set-ups were tested for linearity and calibrated. For calibration, a commercial p-i-n photodiode was used with an identical device mount as that of the DUT. Since high frequency measurements are much more difficult than low frequency measurements and require state of the art techniques, we will give more attention to the high frequency experiment than to the low frequency set-ups.

6.4.1. High Frequency (150 MHz-1 GHz) Noise Measurement Set-up

The highlight of this measuring system is the combination of a modulation scheme first used by Dicke [76] and the circulator method developed by Gasquet et al. [77]. Known as the Dicke radiometer, the modulation scheme is used to separate out the weak signal buried in the background noise stemming from the thermal noise of the load resistor and the amplifier noise. The sensitivity is given by [78]

$$\frac{\Delta T}{T} = \frac{1}{\sqrt{B\tau}} \tag{6.1}$$

where B is the bandwidth of the receiver and τ is the time over which the signal is averaged. In our measurements B is 4MHz and τ has a value of 50 seconds. By substituting these values and using T = 300 K, we obtain $\Delta T = 0.02$K. This is the calculated sensitivity. In reality, available sensitivity is only 0.2 K, mainly because of the unbalanced temperature drift ratios between the calibration source resistance and the load resistance. In the high frequency experiment, impedance matching is important because a false signal results from an impedance mismatch during the Dicke switching. This impedance mismatching problem can be solved by using a circulator. Thus, regardless of the impedance changes in the device, the amplifier is always looking at a 50-Ω termination through the circulator. Several circulators are used to cover the wide frequency range (150 MHz - 1000 MHz). Detailed information about these circulator is given in Table 6.2.

Table 6.2
Circulators used in the high-frequency noise measuring set-up

Circulator Name	Frequency range	Loss (dB)
Innowave 1M16CV	147 - 174 MHz	0.5
Innowave 1M35CZ	300 - 400 MHz	0.4
P&H B1-U36310	500 - 1000 MHz	0.2

A block diagram of the entire system is shown in Fig. 6.12. An LED is used as a light source because of its full shot-noise performance. The wavelength of the LED is 1.3 μm. To avoid stray light which will cause parasitic absorption, light need to be focused on the top surface through the window. Optical fiber guiding turned out to be the best solution for confined illumination. The tip of an optical fiber was mounted on an XYZ micrometer positioner and could be easily positioned at the center of the window. A microscope with 100X multiplication is used to check the optical fiber alignment visually.

The biasing circuit is shown Fig. 6.13. When we increase the reverse bias, breakdown will occur abruptly. Once breakdown occurs, MQW structures are easily destroyed. For protection we built an accurate current limiter whose resolution is as accurate as 0.1μA. As a power source, a regulated power supply is used. The device

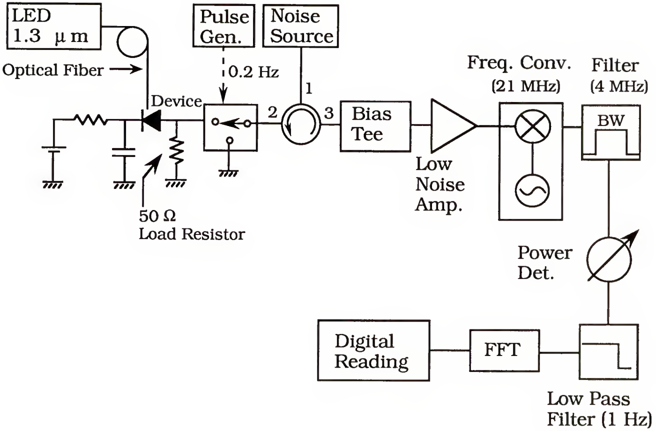

Figure 6.12 High-frequency noise measurement set-up.

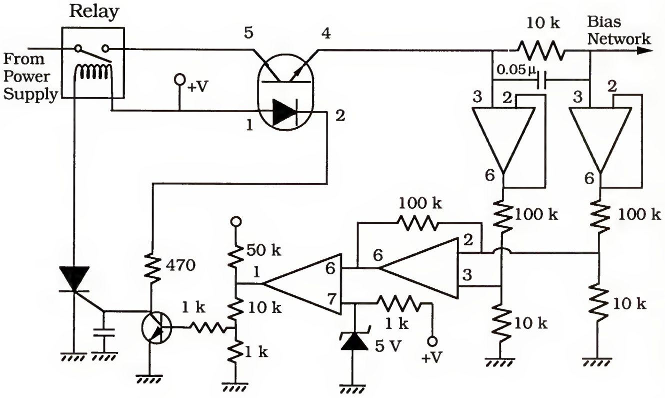

Figure 6.13 Current limiting circuit for the device protection.

under test (DUT) is mounted on a 50-Ω microstripline with a 50-Ω termination as shown in Fig. 6.14.

Immediately following the DUT is a coaxial relay switch which is operated by a pulse generator. The output of the relay switch is fed to circulator port 2 while a noise source (HP346B) is hooked up to circulator port 1. Since the HP346B is not a variable calibration noise source, an attenuator is used to adjust the calibration noise signal level. With an attenuator in series, calibration noise temperature T_{cal} is given by [79]

$$T_{cal} = LT_{NS} + (1-L)T_o \qquad (6.2)$$

where T_{NS} represents the noise source temperature, T_o is room temperature and L denotes the attenuator factor.

Following the circulator is the bias tee (HP11590A) which couples the noise signal to the low noise amplifier (LNA) and shorts the 50-Ω load resistor D.C. wise. The latter helps to avoid Joule heating of the load resistor.

Frequency selection is obtained with the noise figure meter (HP8970A), which is capable of receiving RF signals from 10 MHz to 1.5 GHz with a bandwidth of 4.0 MHz. Instead of using the power detector built in the noise figure meter, we employ a separate power detector (HP432B). In other words, the noise figure meter is used as a frequency converter in this set-up and we get the

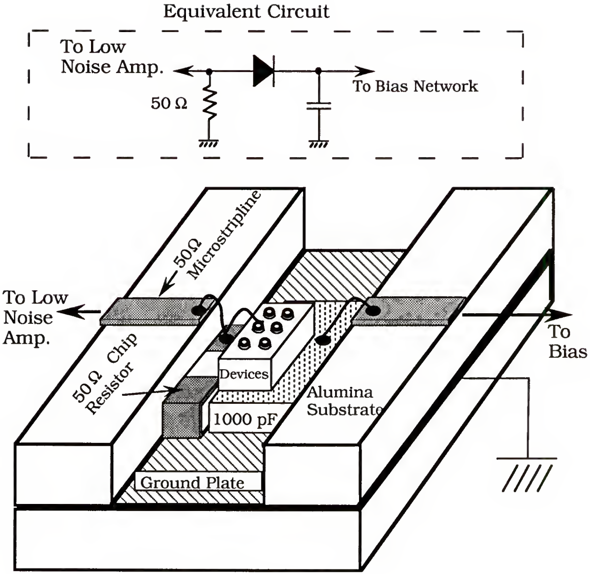

Figure 6.14 Configuration of a device mount

signal output from its intermediate frequency (21 MHz) output. To obtain an additional 20dB boost of this signal, a high frequency amplifier (HP8447F) is placed after the 21 MHz low-pass filter. Power detector (HP432B) produces a voltage signal at the monitor termination as well as an analog reading. The voltage output is fed to the FFT spectrum analyzer (HP3582A) through the low-pass filter with bandwidth of 1 Hz. Finally, the FFT analyzer displays the magnitude of the detected power signal as a function of frequency. When the coaxial relay switches slowly (0.2Hz) between port 1 and port 2, the difference between the noise generated in the DUT and the calibration noise source is displayed. The FFT spectrum analyzer averages the block function which is collected for 50 seconds (10 periods) and separates out the 0.2 Hz component by Fourier transformation.

6.4.2. Medium High Frequency (10 MHz - 300 MHz) Noise Measurement Set-up

In this frequency range, it is difficult to obtain the proper circulators to cover a wide frequency range. Without the circulator, impedance mismatches in the front-end cause a false signal during the Dicke switching. But it turned out that below 300 MHz the false signal due to the impedance mismatching is not serious. In that case, we are able to eliminate the offset caused by the impedance mismatches of the front-end system by following the procedures which we will discuss in the next section. However, impedance changes due to the bias dependent junction capacitance can not be compensated. Therefore this limitation allows us to measure the noise of the DUT at low bias only, because then we can neglect the change in the junction capacitance with bias.

Another difficulty arises when we operate the relay switch without using the circulator. For the short time interval when the mechanical switch moves from port 1 to port 2, the input of the amplifier floats. This results in a large spike in the output signal. To eliminate this troublesome spike, we designed a device whose block diagram is shown in Fig. 6.15. The pulse generator which operates the relay switch triggers the monostable multivibrator (SN74121) to generate the pulse. Controlling the potentiometer we adjust the pulse width to activate relay 2 for a time interval which should be slightly larger then the duration of the spike. When the relay is turned on, the input of the spectrum analyzer floats, but the output signal of the spectrum analyzer remains the same because of the large RC time constant due to the large value of the coupling capacitor and the high input impedance. Thus, the signal fed to the spectrum analyzer is skipped, eliminating the spike. Other portions of the set up are the same as in the previous section.

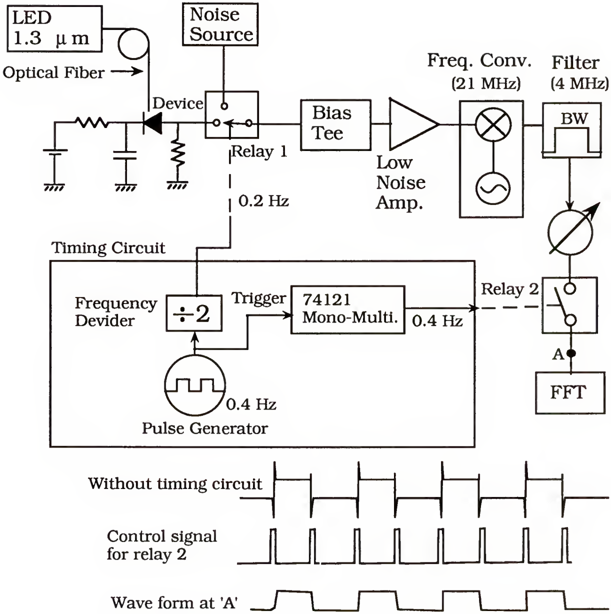

Figure 6.15 Measuring sep-up with the spike-eliminating timing circuit and related waveforms

6.4.3. High Frequency Noise Measurement Procedure

The experimental procedure consists of four measurements to determine the noise temperature of the DUT. The following symbols will be used in this section

T_o = Room temperature

T_{Do} = Temperature of the DUT in equilibrium

T_D = Temperature of the DUT

T_{ND} = Noise temperature of the DUT

T_a = Temperature of the amplifier

T_{cal} = Temperature of the calibration noise source

G^2BW = Gain bandwidth product

Γ = Voltage reflection coefficient

k = Boltzmann's constant

Measurements proceed as follows:

1) Short the input and turn off the calibration noise source. Then the noise source temperature equals room temperature. This procedure gives a meter reading equal to

$$M_1 = G^2 \cdot BW[kTa + kT_o] \qquad (6.3)$$

2) Keep the input shorted and turn on the noise source. Then the noise source radiates the calibration noise power kT_{cal} per unit bandwidth. The meter reading becomes

$$M_2 = G^2 \cdot BW[kT_a + kT_{cal}] \qquad (6.4)$$

3) Have the DUT connected to the input and turn off the noise source. This gives a meter reading of

$$M_3 = G^2 \cdot BW[kT_a + kT_{Do}(1-|\Gamma|^2) + kT_o|\Gamma|^2] \qquad (6.5)$$

4) Have the DUT connected and turn on the noise source. The meter reading becomes

$$M_4 = G^2 \cdot BW[kT_a + kT_{Do}(1-|\Gamma|^2) + kT_{cal}|\Gamma|^2] \qquad (6.6)$$

Manipulation of the above four equations yields the following expression for the DUT temperature.

$$T_{Do} = T_o[1 + T_{cal}\frac{M_3 - M_1}{(M_3 - M_1)+(M_2 - M_4)}] \qquad (6.7)$$

where $M_3 - M_1$ and $M_2 - M_4$ are obtained by operating the switch S_1 with the noise source turned off and turned on, respectively.

Ideally T_{Do} should be equal to T_o. But this is not what we experienced. There still might be impedance mismatches in the front-end and small temperature differences between the noise source and the load resistor in the device mount. These non-idealities result in an offset signal in the meter reading. We repeat the above four procedures with the DUT biased. Then we obtain

$$T_D = T_o[1 + T_{cal}\frac{M_3 - M_1}{(M_3 - M_1)+(M_2 - M_4)}] \qquad (6.8)$$

By subtracting Eq.(6.7) from Eq.(6.8) we obtain the noise temperature T_{ND} of the DUT.

Depending on the measuring frequency range we have to replace the circulator.

6.4.4. Low-frequency Noise Measurement Set-up and Procedure

As shown in Fig. 6.16, in this measurement set-up a standard measurement scheme is used. Sensitivity is not a critical limitation in this frequency range because of two reasons. One is that employing a large value (5 KΩ) load resistor improves the sensitivity hundred times over the high-frequency set-up value. The second reason is that preliminary experiments showed large excess noise levels.

Since the frequency range of the LNA and spectrum analyzer is not wide enough to cover the entire frequency range from 100 Hz - 1.5 MHz, required in this system, we divide this frequency range into two frequency spans ranging from 100 Hz - 25 KHz and from 10 KHz - 1.5 MHz. For each frequency span, the required equipment is listed in Table 6.3.

Table 6.3

	100 Hz - 25 KHz	10 KHz - 1.5 MHz
Analyzer	HP	Wave Analyzer
LNA	EG&G	ANZAC or CHW
Noise Source	Signal supplied by HP analyzer	Rhode & Schwarz

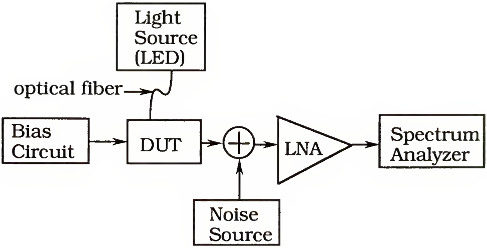

Figure 6.16 Low-frequency noise measuring set-up

Three measurements are required to determine the noise of the DUT. The procedure is as follows.

1) Short the input of the LNA. Then the meter reading corresponds to (see Fig. 6.17a)

$$M_1^2 = G^2 BW \cdot S_{Va} \qquad (6.9)$$

where S_{Va} represents the voltage spectral density of the LNA. Note that squared values of reading M_1 and gain G are used since noise is a quadratic quantity.

2) Connect the DUT to the LNA. The meter reading becomes (see Fig. 6.17b)

$$M_2^2 = G^2 BW \cdot [S_{Va} + (S_{iL} + S_{iD} + S_{ia})(R_i//R_L)^2 \qquad (6.10)$$

where S_{iL} = current spectral density of the load resistor
S_{iD} = current spectral density of the DUT
S_{ia} = current spectral density of the LNA
R_i = internal impedance of the LNA
R_L = load resistance

3) Add the calibration noise source with the DUT connected to the LNA. This gives a meter reading of

$$M_2^2 = G^2 BW \cdot [S_{Va} + (S_{iL} + S_{iD} + S_{ia} + S_{cal})(R_i//R_L)^2] \qquad (6.11)$$

Note that Fig. 6.17c shows the equivalent circuit concerning the above equation.

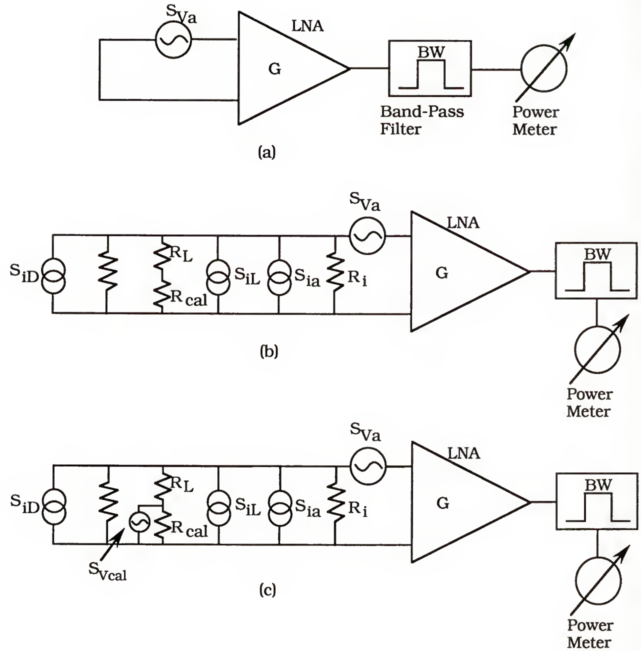

Figure 6.17 Noise equivalent circuit of the measuring set-up

Manipulating these four equations yields the unknown spectral density of the DUT

$$S_{iD} = \left(\frac{M_2^2 - M_1^2}{M_3^2 - M_2^2} \right) \frac{S_{Vcal}}{R_L^2} - \frac{4KT}{R_L} - S_{ia} \qquad (6.12)$$

There is an alternative scheme which simplifies the previous procedure. Instead of using a calibration noise source, the thermal noise of the load resistor can be used to calibrate the measurements. In the frequency span from 10 KHz - 1.5 MHz, this alternative scheme was used. Both of the schemes yielded the same results. Following is the modified procedure.

1) Short the input of the LNA
2) Connect the DUT with bias turned on
3) Keep the DUT connected and turn off the bias

These procedures yield the following three equations

$$M_1^2 = G^2 BW \cdot [S_{Va}] \qquad (6.13)$$

$$M_2^2 = G^2 BW \cdot [S_{Va} + S_{th,R_L} + S_{iD}(R_L//R_i)^2] \qquad (6.14)$$

$$M_3^2 = G^2 BW \cdot [S_{Va} + S_{th,R_L}] \qquad (6.15)$$

From these three equations, we obtain

$$S_{iD} = \frac{M_2^2 - M_3^2}{M_3^2 - M_1^2} \cdot \frac{4KT}{R_L} \qquad (6.16)$$

6.5. Results and Discussion of the Noise Measurements

The noise measurements on device UM505 were carried out first. The device was kept at room temperature. The results for the current noise spectra between 100 Hz and 1 GHz are presented in Fig. 6.18 We note that the DUT exhibits excess noise which decreases approximately as 1/f at low frequencies and reaches a plateau level for high frequencies. For an ordinary photodiode the plateau level is supposed to coincide with full-shot noise. However, this MQW-APD exhibits sub-shot noise at low bias. For example, for a bias current of 4 μA, the measured current noise is a factor of four lower than the full-shot noise level. As the bias increases, the noise increases and full-shot noise is obtained at a bias current of 9 μA. To investigate the bias dependence of the noise in more detail, several measurements were carried out at different frequencies. Their results are presented in Fig 6.19 to Fig. 6.22. In these measurements, the bias range is between 3 μA and 10 μA. The lower limit was determined by the maximum sensitivity of the measuring system and the upper limit is chosen to avoid excess tunneling current. To find the noise level at low bias below the measuring range, we used an extrapolation method and obtained 0.06 K for 1.0 μA, which is approximately 1/60 smaller than full-shot noise. This sub-shot noise phenomenon is a result of the trapping and detrapping in the undepleted

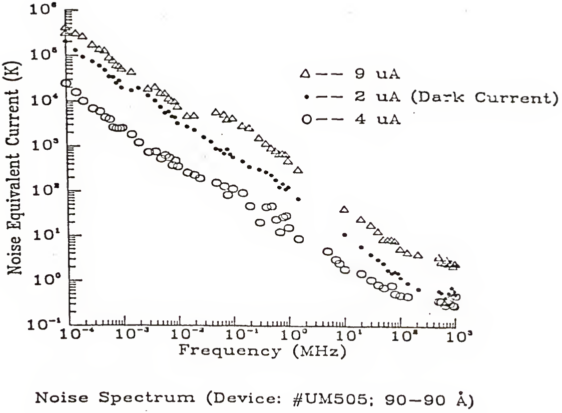

Figure 6.18 Noise spectra of the device UM505.

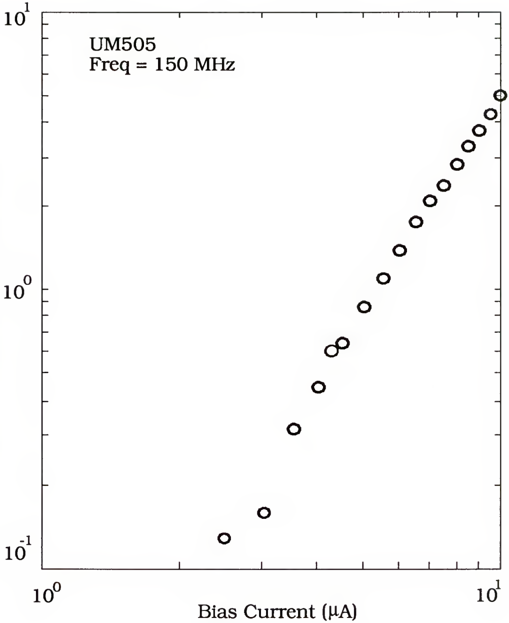

Figure 6.19 Noise temperature vs. bias current at an operating frequency of 150 MHz

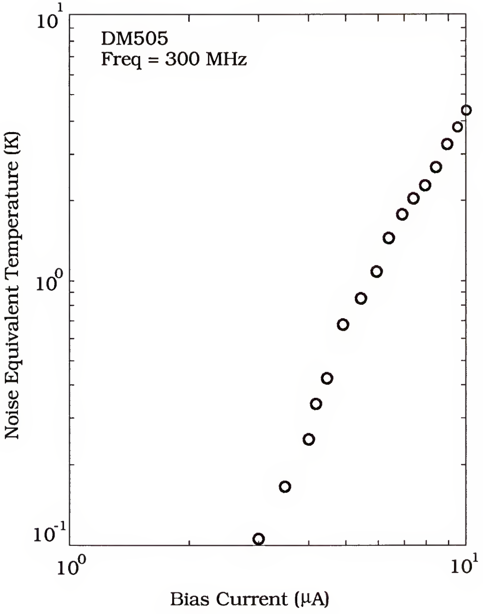

Figure 6.20 Noise temperature vs. bias current at an operating frequency of 300 MHz

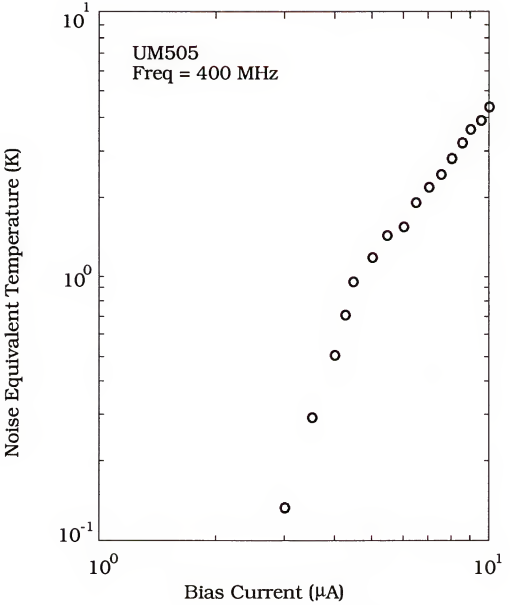

Figure 6.21 Noise temperature vs. bias current at an operating frequency of 400 MHz

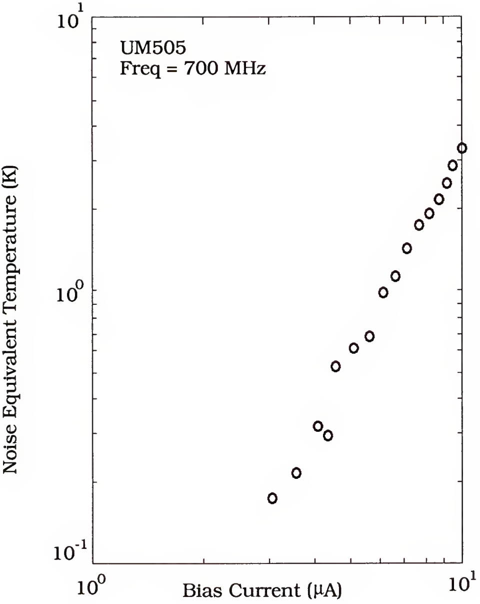

Figure 6.22 Noise temperature vs. bias current at an operating frequency of 700 MHz

multiquantum-wells as mentioned in chapter V. From the noise spectrum, we also note that the large excess noise levels showing up over a wide frequency range need to be explained. One possible explanation is that the large number of heterostructure interfaces results in a large number of interface states or deep level traps which will increase the generation-recombination process.

The noise spectrum of device UM516 was measured between 10 Hz and 25 KHz. Fig. 6.23 demonstrates the results and we see that this device also exhibits 1/f-noise like excess noise at low frequencies. Fig. 6.24 presents the high frequency noise spectra which were measured between 10 MHz and 1 GHz at room temperature. The noise levels off at roughly 150 MHz. Below this corner frequency, the frequency dependence is weak in contrast to what we observed in device UM505. Our explanation is as follows. Device UM516 has 25 periods of heterostructure layers compared to 100 layers for UM505. Having a smaller number of interfaces results in a smaller number of interface states or traps, thus resulting in a decrease in generation-recombination noise.

The current noise versus bias current was measured at several different frequencies. The bias range is between 4 μA and 20 μA. Above 7 μA, the noise of the DUT is increasing nearly linearly with the bias current, but is a factor of three less than the full-shot noise level. Even

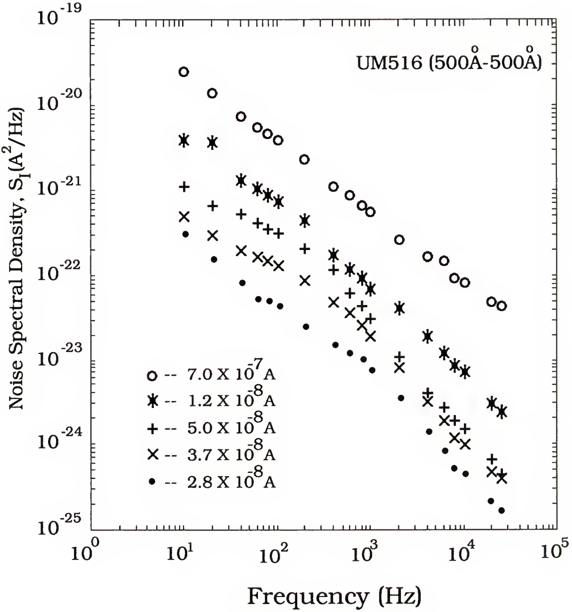

Figure 6.23 Low-frequency noise spectra of the device UM516

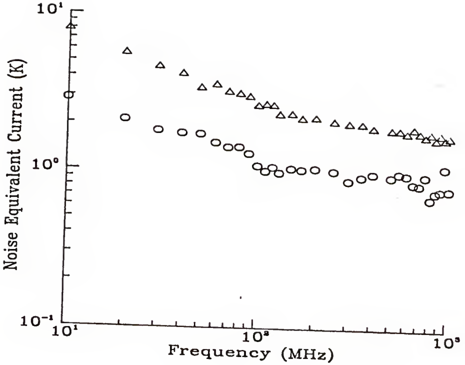

Figure 6.24 Noise spectra of the device UM 516.

at high bias, this device exhibits sub-shot noise. The C-V characteristic also indicates that punch through or full depletion is difficult to obtain in this structure. This suggests that there are at least three or four undepleted quantum-wells in the center of the depletion region. Compared to device UM505, this structure (UM516) has wider quantum-wells (500 Å) and a larger number of thermally generated carriers. When we increase the bias further to deplete the undepleted quantum-wells, large tunneling currents in the low band-gap may prevent complete depletion.

In Fig. 6.25 a break point occurs at bias current of 7 μA. Below this bias, it is difficult to estimate the factor of sub-shot noise due to the poor sensitivity of the set-up. To overcome this difficulty, we used a semiconductor laser as a light source to get more photo-current. The noise of the laser was characterized with a conventional p-i-n diode. Fig. 6.26 presents the bias dependent noise of the DUT illuminated by the laser. At 15 μA bias, which is the lower bias limit, the device noise is 1/23 smaller than full-shot noise. The reciprocal value of this fraction is close to the number of quantum-wells in this structure.

Device UM504 has very thin (30 Å), but a large number (180) of heterostructure layers. Therefore, low-frequency noise measurements exhibit large excess noise level as

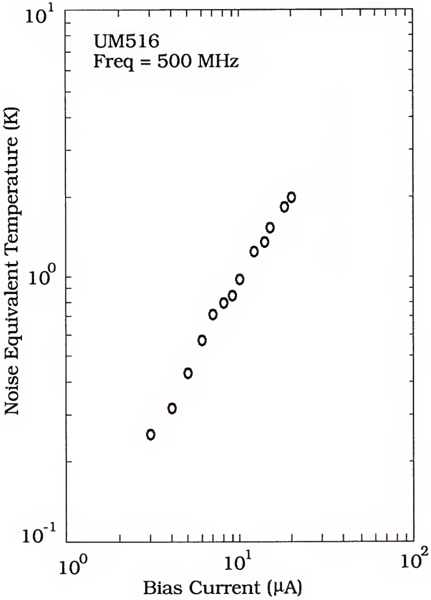

Figure 6.25 Noise temperature vs. bias current at an operating frequency of 500 MHz

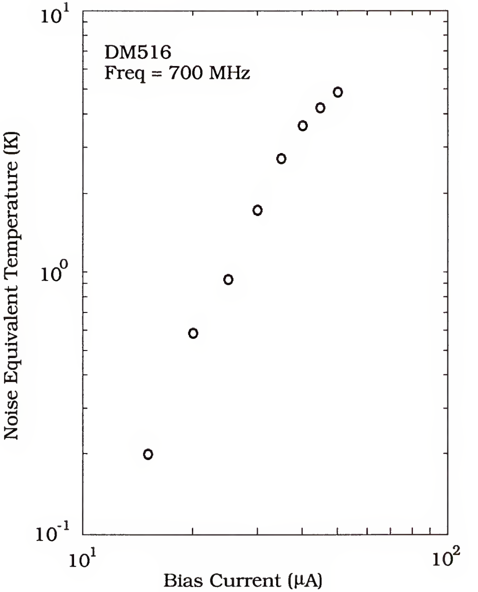

Figure 6.26 Noise temperature vs. bias current at an operating frequency of 700 MHz

shown in Fig. 6.27. The high frequency noise spectrum shown in Fig. 6.28 seems to indicate that the current noise of the DUT is strongly frequency dependent. But if we take the series resistance and junction capacitance into account and calculate the actual amount of noise generated in the DUT, the spectrum becomes flat and coincides with a full-shot noise level. This has to be expected because the structure with thin transparent layers is quite similar to a conventional bulk structure.

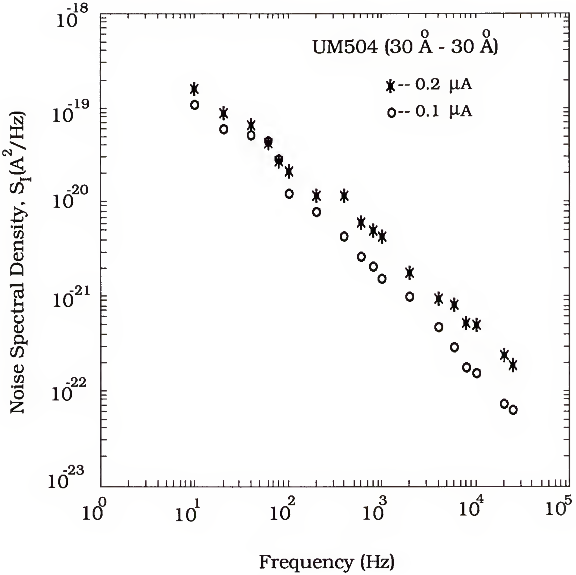

Figure 6.27 Noise Spectra of the device UM504

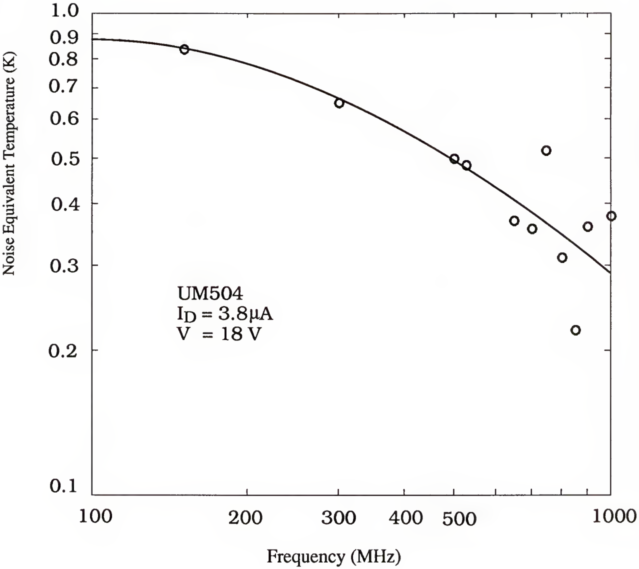

Figure 6.28 High-frequency Noise Spectra of the Device UM504

CHAPTER VII
SUMMARY, CONCLUSIONS AND RECOMMENDATIONS FOR FUTURE RESEARCH

7.1 Summary and Conclusions

We have described a theoretical and experimental study on the opto-electronic properties of MQW heterostructure p-i-n diodes grown by molecular beam epitaxy.

In the course of our experimental investigations, we have faced many unexpected difficulties. First of all, the large excess noise components at low frequencies resulted in a lower corner frequency of the high frequency noise plateau of 200 MHz, which is an extraordinarily high value compared to the value of several MHz in conventional p-i-n diodes. Hence, we had to build a new high-frequency noise measuring set-up employing Gasquet's circulator method and Dicke's radiometer technique.

Secondly, in our high frequency measurement, the noise signal was often masked by parasitic effects arising from junction capacitance, series resistance, and signal cables. Therefore, S-parameter measurements were performed to characterize the high-frequency small signal properties of the device and the device holder, so that we could correct the measured noise signal for parasitic effects.

Thirdly, distinctive sub-shot noise levels observed in the devices with 90-90 and 500-500 Angstrom layers were not understood at first. To confirm the credibility of the measuring system, the noise of a conventional p-i-n diode mounted in an identical device mount was measured. The results of this measurement assured us that our measuring system was working properly.

As suggested by Gisolf [65], Bernamont [66], and Machlup [67], a possible cause for distinctive sub-shot noise in semiconductor devices can be the coupling of carrier motion to the external circuit when the carriers are trapped and detrapped. We found a strong correlation between the number of undepleted quantum-wells and the sub-shot noise levels over a wide bias range. By incorporating the results of C-V, I-V and noise measurements as a function of bias, we conclude that the observed sub-shot noise levels are due to the trapping and detrapping in the undepleted multiquantum-wells. The following observations can be understood in this context.

In the case of the 30-30 Angstrom devices, which have transparent quantum-well layers, full-shot noise was observed in the frequency range between 200 MHz and 1 GHz, whereas in the case of the 90-90 and the 500-500 Angstrom devices, where the barriers are no longer transparent and the carriers are trapped and thermal assisted detrapped in the quantum-wells, distinctive sub-shot noise levels were observed. As reverse bias increases, the quantum-well layers located in the i-region are depleted gradually i.e., one quantum-well at a time, resulting in a gradual increase of the noise level. At the field strength where all quantum-wells are depleted, full-shot noise is observed.

The excess noise observed at frequencies below 200 MHz is of the generation-recombination type and is caused by electrons trapping and detrapping in heterostructure interface states.

To support the experimental study of carrier trapping and detrapping noise, a qualitative theory was developed based on a simplified MQW model. Only two energy levels were assumed in this model, namely the extended state level which corresponds to the conduction band-edge of the wide-gap InAlAs layers and the localized state level which corresponds to the conduction band-edge of the InGaAs layers. To obtain the current fluctuation expression, the transfer impedance method was used in solving the transport equations to which we added rate fluctuation noise terms.

From C-V measurements, successive depletion of quantum-wells over a wide bias range was observed in 90-90 and 500-500 Angstrom devices, whereas in 30-30 Angstrom case, immediate depletion near zero bias was observed. This C-V data in conjunction with bias dependent noise data strongly indicate that trapping and detrapping in the undepleted quantum-wells determine the overall current noise level.

The dark current-voltage characteristic is controlled by field assisted thermal emission of thermally generated carriers from the quantum-wells, whereas the photocurrent is controlled by field assisted injection of optically generated electrons from the low bandgap absorption region into the depletion region at low bias. At higher bias, the photocurrent is limited by carrier transit across the undepleted quantum-well layers. At extremely high bias, Zener tunneling current becomes dominant.

7.2. Recommendations for Future Research

Firstly, we recommend more detailed C-V measurements to investigate the charge distribution of the MQW structures. From these measurements accurate, bias dependent, band profiles can be obtained.

Secondly, we recommend that structures made of other compound materials and different compositions should be investigated to compare the characteristics of charge transport through the MQW layers.

Thirdly, bottom illumination is recommended to give pure hole injection instead of electron injection as was employed in our study. In this way, hole transport through the multiquantum-well hetero-junctions can be compared with electron transport in terms of detrapping activation energy, bias dependence of hole injection over a valence-band potential barrier, hole confinement in quantum-wells, etc.

Fourthly, we recommend employing a filter with a wider bandwidth in the high-frequency receiver to enhance the measuring sensitivity. Currently our receiver has a 4 MHz bandpass filter. For instance, with the use of 16 MHz bandpass filter, sensitivity will be enhanced two times, allowing us to get more data in the lower bias regime.

Fifthly, low temperature noise measurements are recommended to accurately determine the activation energy of the detrapping carriers in the quantum-well layers. Measurements of the low-frequency spectrum as a function of temperature will greatly benefit the analysis and the identification of an excess noise source. Also the dark current can be appreciably reduced by lowering the temperature. Then, it might be possible to increase the reverse bias to initiate band-to-band ionizations. One of the practical problems that needs to be addressed is how to put an optical alignment mechanism inside the cryostat chamber.

Sixthly, we recommend that for low-noise APD applications, the desired enhancement of ionization coefficient ratio α/β should be obtained by employing resonant impact-ionization schemes. Hence, HgCdTe or

GaAlSb bulk materials with split-off bands seem to be relevant. From our study on trapping and detrapping noise, it is found that homogeneous bulk structures are to be preferred since they have less excess noise at low-frequencies.

Finally, we recommend that Monte Carlo simulations should be performed to gain more understanding of the carrier transport mechanism in the direction perpendicular to the heterojunction interface.

APPENDIX A
APPLICATION OF THE COMPOUNDING THEOREM TO A BERNOUILLI TRIAL

Consider the following situation:

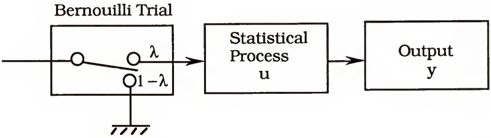

The generating function of the Fowler type of y and ϕ_y is by definition equal to

$$\phi_y(z) = \sum_y z^y W(y), \qquad (A.1)$$

where W(y) is the probability that the statistical variable y has a value y.

Hence in the above-pictured situation,

$$\phi_y(z) = \sum_y z^y W(y) = z^0 W(y{=}0) + z^1 W(y{=}1) + z^2 W(y{=}2) + \cdots \qquad (A.2)$$

The only way that y can be zero is by not feeding the statistical process a particle. The probability for this is $1 - \lambda$; consequently, $W(y{=}0) = 1 - \lambda$. From inspection of the above figure, we conclude that $W(y{=}1)$ has to be equal to $\lambda \cdot W(u{=}1)$, and that $W(y{=}2)$ equals $\lambda \cdot W(u{=}2)$, etc.

Substituting these results in equation (A.2) gives for $\phi_y(z)$:

$$\begin{aligned}\phi_y(z) &= 1\cdot(1-\lambda) + z^1\lambda W(u=1) + z^2\lambda W(u=2) + \cdots \\ &= 1 - \lambda + \lambda\phi_u(z) \qquad \text{(A.3)}\end{aligned}$$

If we define the function $\omega(z)$ by

$$\omega(z) = 1 - \lambda + \lambda z,$$

then, Eq. (A.3) reads

$$\phi_y(z) = \omega(\phi_u(z)). \qquad \text{(A.4)}$$

Equation (A.4) is a form of the compounding theorem we used in Chapter II, Eq. (2.94).

APPENDIX B
EVALUATION OF SUB-INTEGRALS

$$I_{01} \equiv \int_{0}^{x_1} Q(x')\, e^{\int_{0}^{x'} P dx''}\, dx'$$

$$= \frac{Q_1}{P_1}\,[e^{-P_1 l_1} - 1] \qquad (B.1)$$

$$I_{12} \equiv \int_{x_1}^{x_2} Q(x')\, e^{\int_{0}^{x'} P dx''}\, dx'$$

$$= Q_2 \int_{x_1}^{x_2} e^{\int_{0}^{x_1} P dx'' + \int_{x_1}^{x'} P dx''}\, dx'$$

$$= Q_2 \int_{x_1}^{x_2} e^{P_1 l_1} . e^{P_2 (x' - x_1)}\, dx'$$

$$= Q_2 \cdot e^{P_1 l_1} . e^{-P_2 x_1} \int_{x_1}^{x_2} e^{P_2 x'}\, dx'$$

$$= Q_2 \cdot e^{(P_1 - P_2) l_1} . \frac{1}{P_2} [e^{P_2 x_2} - e^{-P_2 x_1}]$$

$$= \frac{Q_2}{P_2} \cdot e^{(P_1 - P_2) l_1} [e^{P_2 (l_1 + l_2)} - e^{P_2 l_1}]$$

$$= \frac{Q_2}{P_2} [e^{P_1 l_1 + P_2 l_2} - e^{P_1 l_1}]$$

$$= \frac{Q_2}{P_2} \cdot e^{P_1 l_1} [e^{P_2 l_2} - 1] \qquad (B.2)$$

$$I_{23} \equiv \int_{x_2}^{x_3} Q(x') e^{\int_0^{x'} P dx''} dx'$$

$$= Q_1 \int_{x_2}^{x_3} e^{\int_0^{x_1} P dx'' + \int_{x_1}^{x_2} P dx'' + \int_{x_2}^{x'} P dx''} dx'$$

$$= Q_1 \int_{x_2}^{x_3} e^{P_1 l_1 + P_2 l_2} . e^{P_1 (x' - x_2)} dx'$$

(Note; $x_2 = l_1 + l_2$)

$$= Q_1 \int_{x_2}^{x_3} e^{(P_2 - P_1) l_2} . e^{P_1 x'} dx'$$

$$= \frac{Q_1}{P_1} \cdot e^{(P_2 - P_1) l_2} [e^{P_1 x_3} - e^{P_1 x_2}]$$

$$= \frac{Q_1}{P_1} \cdot e^{(P_2 - P_1) l_2} [e^{P_1 (2 l_1 + l_2)} - e^{P_1 (l_1 + l_2)}]$$

$$= \frac{Q_1}{P_1} \cdot [e^{2 P_1 l_1 + P_2 l_2} - e^{P_1 l_1 + P_2 l_2)}]$$

$$= \frac{Q_1}{P_1} \cdot e^{P_1 l_1 + P_2 l_2} [e^{P_1 l_1} - 1] \qquad (B.3)$$

$$I_{34} \equiv \int_{x_3}^{x_4} Q(x')\, e^{\int_0^{x'} Pdx''} dx'$$

$$= Q_2 \int_{x_3}^{x_4} e^{\int_0^{x_1} Pdx'' + \int_{x_1}^{x_2} Pdx'' + \int_{x_2}^{x_3} Pdx'' + \int_{x_3}^{x'} Pdx''} dx'$$

$$= Q_2 \int_{x_3}^{x_4} e^{2P_1l_1+P_2l_2} . e^{P_2(x'-x_3)} dx'$$

(Note; $x_3 = 2l_1+l_2$)

$$= Q_2 \int_{x_3}^{x_4} e^{2P_1l_1+P_2l_2-2P_2l_1-P_2l_2} . e^{P_2x'} dx'$$

$$= Q_2 e^{2(P_1l_1-P_2l_1)} \int_{x_3}^{x_4} . e^{P_2x'} dx'$$

$$= \frac{Q_2}{P_2} . e^{2l_1(P_1-P_2)} [e^{P_2x_4} - e^{P_2x_3}]$$

$$= \frac{Q_2}{P_2} e^{2l_1(P_1-P_2)} [e^{2P_2(l_1+l_2)} - e^{P_2(2l_1+l_2)}]$$

$$= \frac{Q_2}{P_2} . [e^{2(P_1l_1+P_2l_2)} - e^{2P_1l_1+P_2l_2}]$$

$$= \frac{Q_1}{P_1} . e^{2P_1l_1+P_2l_2} [e^{P_2l_2} - 1] \qquad (B.4)$$

$$I_{45} = \frac{Q_2}{P_2} . e^{2(P_1l_1+P_2l_2)} [e^{P_1l_1} - 1] \qquad (B.5)$$

$$I_{56} = \frac{Q_1}{P_1} \cdot e^{3P_1l_1+2P_2l_2}[e^{P_2l_2} - 1] \qquad (B.6)$$

$$I_{67} = \frac{Q_2}{P_2} \cdot e^{3(P_1l_1+P_2l_2)}[e^{P_1l_1} - 1] \qquad (B.7)$$

.

.

.

APPENDIX C
EVALUATION OF DOUBLE INTEGRALS

$$I_1 = \frac{2}{T}\int_0^{x_1}\int_0^{x_1}\overline{\tilde{E}(x,\omega)\tilde{E}^{*}(x',\omega)}\,dx\,dx'$$

$$= K\gamma_n \int_0^{x_1}\int_0^{x_1}\overline{\left(\frac{Q_2' Q_2'^{*}}{P_2 P_2^{*}}\right)}\left[1+e^{-(P_2+P_2^{*})l}-2\mathrm{Re}\left(e^{P_2 l}\right)\right]\delta(x-x')\,dx\,dx'$$

$$= K\gamma_n \int_0^{x_1}\overline{\left(\frac{Q_2' Q_2'^{*}}{P_2 P_2^{*}}\right)}\left[1+e^{-(P_2+P_2^{*})l}-2\mathrm{Re}\left(e^{P_2 l}\right)\right]dx$$

$$\sim K\gamma_n \int_0^{x_1}\overline{\left(\frac{Q_2' Q_2'^{*}}{P_2 P_2^{*}}\right)}\,dx$$

$$= K\gamma_n \overline{\left(\frac{Q_2' Q_2'^{*}}{P_2 P_2^{*}}\right)}\,l \tag{C.1}$$

$$I_2 = \frac{2}{T}\int_{x_1}^{x_2}\int_{x_1}^{x_2}\overline{\tilde{E}(x,\omega)\tilde{E}^{*}(x',\omega)}\,dx\,dx'$$

$$= K\gamma_n \int_{x_1}^{x_2}\int_{x_1}^{x_2}\overline{\left(\frac{Q_2' Q_2'^{*}}{P_2 P_2^{*}}\right)\left[e^{-P_1^{*}l}-e^{-(P_1+P_2)^{*}l}\right]\left[e^{-P_1 l}-e^{-(P_1+P_2)l}\right]}\,\delta(x-x')\,dx\,dx'$$

$$= K\gamma_n \overline{(\frac{Q_2'Q_2'^*}{P_2P_2^*})} \int_{x_1}^{x_2} [e^{-(P_1+P_1^*)l} + e^{-\{(P_1+P_1^*)+(P_2+P_2^*)\}l} - 2\mathrm{Re}(e^{-(2P_1+P_2)l})]dx$$

$$\sim 0 \tag{C.2}$$

$$I_3 = \frac{2}{T}\int_{x_2}^{x_3}\int_{x_2}^{x_3} \overline{\tilde{E}(x,\omega)\tilde{E}^*(x',\omega)}\,dxdx'$$

$$= K\gamma_n \int_{x_1}^{x_2}\int_{x_2}^{x_3} \overline{(\frac{Q_2'Q_2'^*}{P_2P_2^*})\,[1-e^{-P_2^*l}+e^{-(P_1+P_2)^*l}-e^{-(P_1+2P_2)^*l}]}$$

$$\cdot\overline{[1-e^{-P_2l}+e^{-(P_1+P_2)l}-e^{-(P_1+P_2)l}]}\,\delta(x-x')\,dxdx'$$

$$\sim K\gamma_n \int_0^{x_1} \overline{(\frac{Q_2'Q_2'^*}{P_2P_2^*})}\ [1+0+0+\cdot\ \cdot\ \cdot+0]dx$$

$$= K\gamma_n\ \overline{(\frac{Q_2'Q_2'^*}{P_2P_2^*})}l \tag{C.3}$$

.

.

.

REFERENCES

1. R. Chin, N. Holonyak, Jr., G. E. Stillman, J. T. Tang, and K. Hess, Electron. Lett., 16, 467 (1980).

2. F. Capasso, W. T. Tsang, A. L. Hutchinson, and G. F. Williams, Appl. Phys. Lett., 40 (1), 38 (1982).

3. F-Y. Juang, U. Das, Y. Nashimoto, and P. K. Bhattacharya, Appl. Phys. Lett., 47 (9), 972 (1985).

4. F. Capasso, J. Allam, A. Y. Cho, K. Mohammed, R. J. Malik, A. L. Hutchinson, and D. Sivco, Appl. Phys. Lett. 48 (19), p. 1294 (1986).

5. J. Allam, F. Beltram, F. Capasso, and A. Cho, Appl. Phys. Lett. 51 (8), p. 575 (1987).

6. F. Capasso, Semiconductors and Semimetals, vol. 22, part D, Chap. 1, Academic Press, Orlando (1985).

7. K. K. Thornber, J. Appl. Phys., 52, 279 (1981).

8. P. A. Wolff, Phys. Rev., 95, 1415 (1954).

9. W. Shockley, Solid State Electron., 2, 35 (1961).

10. G. A. Baraff, Phys. Rev., 128, 2507 (1962).

11. H. Shichijo and K. Hess, Phys. Rev. B, 23, 4197 (1981).

12. B. K. Ridley, J. Phys. C, 16, 3373, (1983).

13. L. V. Keldysh, Sov. Phys. JETP (English trans.), 10, 509 (1960).

14. C. L. Anderson and C.R. Crowell, Phys. Rev. B, 5, 2267 (1972).

15. T. P. Pearsall, R. E. Nahory, J. R. Chelikowski, Conf. Ser. - Inst. Phys., 33b, 331 (1977).

16. O. Hildebrand, W. Kuebart, and M. H. Pilkuhn, Appl. Phys. Lett., 37, 801 (1980)

17. O. Hildebrand, W. Kuebart, K. W. Benz, and M. H. Pilkuhn, IEEE J. Quantum Electron., QE-17, 284 (1981).

18. K. Brennan, K. Hess and W. C. Wang, J. Appl, Phys., 57, 1971 (1985).

19. B. K. Ridley, J. Appl. Phys., 48, 754 (1977).

20. P. T. Landsberg and Y-J. Yu, J. Appl. Phys. 63 (5), 1789 (1988).

21. A. van der Ziel, Noise in Measurements, Chap. 4, John Wiley & Sons, New York (1976).

22. A. S. Tager, Sov. Phys. - Solid State, 6, 1919 (1965).

23. R. J. McIntyre, IEEE Trans. Electron Devices, ED-13, 164 (1966).

24. R. J. McIntyre, IEEE Trans. Electron Devices, ED-19, 703 (1972).

25. S. Kain and H. M. Taylor, A First Course in Stochastic Processes, 2nd ed., Academic Press, New York (1963).

26. K. M. Van Vliet and L.M. Rucker, IEEE Trans. Electron Devices, ED-26, 746 (1979).

27. K. M. Van Vliet, A. Friedman, and L.M. Rucker, IEEE Trans. Electron Devices, vol ED-26, 752 (1979).

28. S. D. Personick, Bell Syst. Tech. J., 50, 167 (1971).

29. J. Gong, "Noise in avalanche photodiodes,"ME Thesis, University of Florida (1980).

30. F. Capasso, Laser Focus/Electro-optics (July 1984).

31. M. C. Teich, K. Matsuo, and B. E. Saleh, IEEE J. Quantum Electron., QE-22, 1184 (1986).

32. G. E. Stillman, V. M. Robbins, and N. Tabatabaie, IEEE Trans. Electron Devices, ED-31, 1643 (1984).

33. R. B. Emmons, J. Appl. Phys., 38, 3705 (1967).

34. W. W. Gartner, Phys. Rev., 116, 84 (1959).

35 S. Sze, Physics of Semiconductor Devices, Chap. 13, Wiley (Interscience), New York (1969).

36. H. Melchoir, Laser Handbook, vol. 1, North-Holland, Amsterdam (1972).

37. T. P. Pearsall and M. A. Pollak, Semiconductors and Semimetals, vol. 22, part D, Chap. 3, Academic Press, Orlando (1985).

38. T. Kaneda, Semiconductors and Semimetals, vol. 22, part D, Chap. 3, Academic Press, Orlando (1985).

39. H. Kressel, Semiconductor Devices for Optical Communication, Chap 2, Springer-Verlag, New York (1982).

40. F. Capasso, A. Y. Cho, and P. W. Foy, Electron Lett., 20, 635 (1984).

41. S. R. Forrest, M. DiDomenico, Jr., R. G. Smith, and H. J. Stocker, Appl. Phys. Lett., 36, 580 (1980).

42. K. Nishida, K. Ishii, K. Minemura, and K. Taguchi, Electron Lett., 13, 280 (1977).

43. F. Capasso, H. M. Cox, A. L. Hutchinson, N. A. Olsson, and S. G. Hummel, Appl. Phys. Lett. 55 (11), p. 1193 (1984).

44. B. M. Wul and A. P. Shotov, Solid State Phys. Electron Telecommun., 1, 491 (1960).

45. C. A. Lee, R. A. Logan, R. J. Batdorf, J. J. Kleimack, and W. Wiegmann, Phys. Rev., 134, A, 761 (1964).

46. G. E. Stillman and C. M. Wolfe, Semiconductors and Semimetals, vol. 12, Chap. 5, Academic Press, New York (1977).

47. G. E. Bulman, L. W. Cook, and G. E. Stillman, Appl. Phys. Lett., 40, 589 (1982).

48. F. Capasso, W. T. Tsang, A. L. Hutchinson, and G. F. Williams, Appl. Phys. Lett., 40 (1), 38 (1982).

49. F. Capasso, IEEE Trans. Electron Devices, vol. ED-30, 381 (1983).

50. R. E. Burgess, Faraday Soc. Disc., vol. 28, 151 (1959).

51. K. M. Van Vliet and L. M. Rucker, Physica, vol. 95A, 117 (1979).

52. H. A. Haus and R. B. Adler, Circuit Theory and Linear Noise Networks, New York, Wiley (1959).

53. H. T. Friiss, Proc. IRE, vol. 32, 419 (1944).

54. M. C. Teich, K. Matsuo, and B. E. Saleh, IEEE J. Quantum Electron., QE-22, 1184 (1986).

55. P. T. Landsberg, Solid State Commun. 10, 479 (1972).

56. A. R. Beattie and P. T. Landsberg, Proc. R. Soc. London Ser. A 249, 16 (1958).

57. P. T. Landsberg, Lectures in Theoretical Physics, Vol. 8A, Colorado Press, Boulder (1966).

58. A. R. Beattie, J. Phys. Chem. Solids 24, 1049 (1962).

59. J. R. Hauser, J. Appl. Phys. 37, 507 (1966).

60. W. Franz, Handbuch der Physik , Vol. 17, p. 190., Springer, Berlin (1956)

61. R. A. Ballinger, K. G. Major, and J. R. Mallinson, J. Phys. C 6, 2573 (1973).

62. D. J. Robbins, Phys. Status Solidi B 97, 9 and 387 (1980); 98, 11 (1980).

63. C. Shekhar and S. K. Sharma, Phys. Lett. A 51, 339 (1975).

64. H. Shichijo and K. Hess, Phys. Rev. B 23, 4179 (1982).

65. J. H. Gisolf, Physica 15, no 8-9, 825 (1949).

66. J. Bernmnt, Ann. Physique 7, 71 (1937).

67. A. van der Ziel, Physica 16, no. 4, 359 (1950).

68. S. Machlup, J. of Appl. Phys. 25 (3), 341 (1954).

69. K. M. Van Vliet, A. Friedmann, R. J. Zijlstra, A. Gisolf, and A. van der Ziel, J. of Appl. Phys. 46 (4), 1804 (1975).

70. K. M. Van Vliet, A. Friedmann, R. J. Zijlstra, A. Gisolf, and A. van der Ziel, J. of Appl. Phys. 46 (4), 1814 (1975).

71. S. Tehrani, "Properties of noise and charge transport in layered electronic materials," Ph.D. dissertation, University of Florida (1985).

72. C. F. Whiteside, "Hot-electron noise in Gallium Arsenide/Aluminum Gallium Arsenide heterojunction interfaces," Ph.D. dissertation, University of Florida (1987).

73. A. D. van Rheenen, G. Bosman, and C. M. Van Vliet, Solid-State Electronics 28 (5), p. 457 (1985).

74. R. people, K. W. Wecht, K, Alavi, and A. Y. Cho, Appl. Phys. Lett., 45, 118 (1983).

75. S. R. Forrest, O. K. Kim, and R. G. Smith, Solid State Electron. 26 (10), 951 (1983).

76. R. H. Dicke, Rev. Sci. Instrum. 17, 268 (1946).

77. D. Gasquet, J.C. Vassiere, and J.P. Nougier, Sixth International conference on Noise in Physical Systems (NBS Special Publication 614, 1981), p. 305.

78. G. Evans and C. W. McLeish, RF Radiometer Handbook, Artech house Inc., Dedham (1977).

79. A. van der Ziel, Noise in Solid State Devices and Circuits, John Wiley & Sons, New York (1986).

BIOGRAPHICAL SKETCH

Young-June Yu was born on January 21, 1956, in Jeonju city, Korea. He spent his childhood and boyhood in his hometown until he had to go to Seoul, capital city of Korea, for his college education. He attended the Sogang University from 1973 to 1977. In 1977 he received the Bachelor of Science degree in electronic engineering. From 1977 to 1982 he was employed by the Hong-Loong Machinery Corporation as a research engineer. In 1984 he received the Master of Science degree in electrical engineering from the University of Pittsburgh. Since 1985 he has been a graduate research assistant with the Noise Research Laboratory at the University of Florida.

His areas of interest include opto-electronic device physics, its characterizations, and noise measurements of semiconductor devices.

I certify that I have read this study and that in my opinion it conforms to acceptable standards of scholarly presentation and is fully adequate, in scope and quality, as a dissertation for the degree of Doctor of Philosophy.

GBosman

G. Bosman, Chairperson
Associate Professor of Electrical
Engineering

I certify that I have read this study and that in my opinion it conforms to acceptable standards of scholarly presentation and is fully adequate, in scope and quality, as a dissertation for the degree of Doctor of Philosophy.

CM Van Vliet

C. M. Van Vliet
Professor of Electrical Engineering

I certify that I have read this study and that in my opinion it conforms to acceptable standards of scholarly presentation and is fully adequate, in scope and quality, as a dissertation for the degree of Doctor of Philosophy.

R. Ramaswamy
Professor of Electrical Engineering

I certify that I have read this study and that in my opinion it conforms to acceptable standards of scholarly presentation and is fully adequate, in scope and quality, as a dissertation for the degree of Doctor of Philosophy.

S. S. Li
Professor of Electrical Engineering

I certify that I have read this study and that in my opinion it conforms to acceptable standards of scholarly presentation and is fully adequate, in scope and quality, as a dissertation for the degree of Doctor of Philosophy.

Timothy J. Anderson

T. Anderson
Professor of Chemical Engineering

This dissertation was submitted to the Graduate Faculty of the College of Engineering and to the Graduate School and was accepted as partial fulfillment of the requirements for the degree of Doctor of Philosophy.

May 1989

Hubert A. Bevis

Dean, College of Engineering

Dean, Graduate School